Universidade de Aveiro Departamento de Física
2013

Katrin Markull

Arrestment of the Estuarine Plume in Maputo Bay, Mozambique

Aprisionamento da Pluma Estuarina na Baía de Maputo, Moçambique

Universidade de Aveiro Departamento de Física
2013

Katrin Markull

Arrestment of the Estuarine plume in Maputo Bay, Mozambique

Aprisionamento da Pluma Estuarina na Baía de Maputo, Moçambique

Dissertação apresentada à Universidade de Aveiro para cumprimento dos requisitos necessários à obtenção do grau de Mestre em Ciências do Mar e das Zonas Costeiras, realizada sob a orientação científica do Prof. Doutor João Miguel Sequeira Silva Dias, Professor Auxiliar do Departamento de Física da Universidade de Aveiro e co-orientação do Doutor João Daniel Alonso Antão Lencart e Silva, Investigador Auxiliar no Centro de Estudos do Ambiente e do Mar (CESAM) da Universidade de Aveiro.

o júri

Presidente	Prof.ª Doutora Filomena Maria Cardoso Pedrosa Ferreira Martins Professora Associada do Departamento de Ambiente e Ordenamento da Universidade de Aveiro
Arguente	Doutor Nuno Alexandre Firmino Vaz Investigador auxiliar do CESAM e Departamento de Física da Universidade de Aveiro
Orientador	Prof. Doutor João Miguel Sequeira Silva Dias Professor auxiliar do Departamento de Física da Universidade de Aveiro

acknowledgements

This study was only possible thanks to the help, support and active collaboration of many people.

To Prof. Doutor João Miguel Dias for suggesting this interesting topic for my MSc thesis, for the scientific supervision and for always having been available for any doubts and questions I had.

To Doutor João Daniel Alonso Antão Lencart e Silva, for everything he taught me over the past months, never losing patience and a positive attitude, as well as for having allowed me to use his scientific data of Maputo Bay.

To the NMEC working group, for their availability, support and encouragement, especially during the last months.

To my great friends, for their presence even though some only from the distance.

To Sarah and Guilherme, for their friendship, understanding and support.

To my family, whose support I could always count on.

To Miguel for the unconditional support and understanding in these last months.

keywords

Estuarine dynamics; hydrodynamic modeling; Delft3D; salinity; flushing times; tide; stratification; river flow

abstract

Maputo Bay is a tidally-energetic embayment in Mozambique, influenced by strong rainfall and associated river runoff during the wet season. Previous investigations have suggested the arrestment of the freshwater plume related to high mixing during spring tide, eroding stratification and preventing an efficient exchange with the shelf due to the hampering of density currents. It was suggested that, with decreasing mixing towards neap tide, the bay would re-stratify, releasing the estuarine plume. The objective of this dissertation was to find out whether and under which conditions this arrestment of the estuarine plume occurs in Maputo Bay.

A 3-dimensional hydrodynamic model was applied to the bay, improving a previously published model through vertical and temporal refinement and recalibration. It is shown that now the model reproduces more accurately the semidiurnal and fortnightly stratification-mixing cycles occurring during the wet season. However, the model still predicts salinities lower than those found in observations. Uncertainties increase towards the mouth of the Maputo River, for which only modelled river flow data was available to force the bay dynamics, indicating this input as a possible source of the underestimation of salinity. The effect of varying river discharges, varying timings of discharge as well as varying discharge ratios on flushing times was investigated through a set of experiments of varying Maputo and Incomati river flows as well as timings of discharge during the spring-neap cycle.

The results suggest that when no discharge or a small discharge is introduced, flushing times are smallest during spring tide, when barotropic forcing is strong. Largest flushing times are found approximately 40 hours before neap tide, when tidal forcing is relatively weak. Flushing times for model runs with larger discharge were smaller due to the addition of flushing from river water. Here, flushing times were especially small during neap tide, when the decreased tidal mixing lead to stratification through which a classical estuarine circulation could develop, leading to an efficient bay-shelf exchange. Maximum flushing times for high-discharge runs during wet season were found for spring tide. Shelf-bay exchange was most efficient when the discharge of the Maputo River was larger than the discharge of the Incomati River, due to its location opposite the bay opening, thus influencing a larger area before leaving the bay. Timing of the discharge of the freshwater had only small effects, influencing the amount of mixing induced on the freshwater when first entering the bay.

It is concluded that the estuarine plume of Maputo Bay is in fact arrested during spring tide due to the large mixing inhibiting density currents and is released when mixing decreases, inducing stratification and baroclinic circulation. The potential energy stored in the bay is larger for a larger discharge of the Maputo River.

palavras-chave

Dinâmica estuarina; Delft3D, modelação hidrodinâmica; salinidade; tempos de renovação, maré; estratificação; escoamento fluvial

resumo

A Baía de Maputo, em Moçambique, é uma baía com marés energéticas, influenciada pelo escoamento dos rios associado a forte precipitação durante a estação húmida. Investigações anteriores têm sugerido que o aprisionamento da pluma de água doce está relacionado com a elevada mistura durante a maré viva, que por sua vez provoca a erosão da estratificação e impede a troca eficiente com a plataforma continental, dificultando o estabelecimento de correntes de densidade. Foi sugerido que com a diminuição da mistura durante a maré morta a baía seria re-estratificada, libertando a pluma estuarina. O objetivo desta dissertação foi averiguar se, e em que condições, este aprisionamento da pluma estuarina ocorre na baía de Maputo.

Foi aplicado um modelo hidrodinâmico 3-d para a baía, resultante do melhoramento de um modelo publicado anteriormente, através do refinamento vertical e temporal e recalibração. É demonstrado que agora o modelo reproduz com mais precisão os ciclos de estratificação/mistura semidiurnas e quinzenais que ocorrem durante a estação chuvosa. No entanto, o modelo ainda prevê salinidades inferiores as encontradas em observações. As incertezas aumentam próximo da foz do Rio Maputo, para o qual existem apenas dados de modelos de bacia para forçar o modelo, indicando esta entrada como uma possível causa da subestimação da salinidade. Foi definido um conjunto de experiências de diferentes descargas dos Rios Maputo e Incomati, sendo estes introduzidos no modelo em fárias fases do ciclo da maré. Foi investigado o efeito da variação da duração das descargas fluviais e da proporção do Maputo e do Incomati nos tempos de renovação da água na baía.

Os resultados sugerem que quando há uma pequena descarga dos rios, os tempos de renovação são menores durante a maré viva, quando o forçamento barotrópico é forte. Os maiores tempos de renovação encontram-se cerca de 40 horas antes da maré morta. Os tempos de renovação para as corridas com maior descarga são menores devido à adição de descargas de água do rio. Neste caso, os tempos de renovação foram especialmente pequenos durante a maré morta, quando a diminuição da mistura pela maré induz estratificação, criando condições para o desenvolvimento da circulação estuarina clássica, e escoando a baía eficiente. Tempos máximos de renovação para corridas de alta descarga durante a estação chuvosa foram encontrados em condições mistas de maré viva. O intercâmbio entre a baía e a plataforma continental foi mais eficiente para uma maior proporção do Rio Maputo em relação ao Rio Incomati. Este padrão justifica-se pela maior distância da foz do Rio Maputo à entrada da baía. A variação do momento da descarga de água doce em relação à fase da maré tem efeitos pouco significativos (ou pouco relevantes), determinando apenas o grau de mistura que influencia a água doce nas primeiras horas a seguir da descarga.

Concluiu-se que existe um aprisionamento da pluma estuarina da Baía de Maputo. Este aprisionamento ocorre durante a elevada mistura de maré viva. A energia potencial armazenada na baía é maior para uma descarga maior do Rio Maputo.

Contents

List of Figures

List of Tables

1 Introduction

This dissertation investigates the hydrodynamics of Maputo Bay, Mozambique, under varying forcing conditions. The first chapter provides a general introduction to the topic.

Firstly, in section 1.1, a general introduction will be given and the motivation and aim of this dissertation are presented. Section 1.2 will introduce the state of the art of the arrestment of estuarine plumes, induced by local or distant wind as well as by tidal forcing. Section 1.3 will then present the work structure for the complete dissertation.

1.1 Background, Motivation and Aim

Estuaries are diverse and complex dynamic regions in the transitional zone between land and sea. Due to their rich ecosystems and natural navigational facilities, they often support human concentration and the associated economic activities such as fisheries, transport and tourism. These activities can pose threats on the ecosystems that need to be studied to be fully understood and addressed.

The importance of the several forcing mechanisms involved in estuarine dynamics varies from estuary to estuary. Density-driven circulation in estuaries is usually influenced by river inflow. Other possible factors of importance include tidal dynamics and wind-induced circulation on the continental shelf as well as locally. The competition between the various forcing mechanisms as well as other factors such as topography and Coriolis force determine the so-called buoyancy-stirring interaction described by Simpson (1997). Different salinity distributions and circulation patterns are found, depending on the relative importance of buoyancy/stratification and stirring.

River flow induces buoyancy in estuaries. The freshwater input leads to the development of horizontal gradients, with lighter water moving down-estuary in the upper layers and more dense water moving upstream in the deeper layers. This is known as classical estuarine circulation and induces stratification. Mixing can occur on the interface between fresher river water and more saline sea water (Simpson et al., 1990; Dyer, 1998).

Tides in the ocean are generated by centrifugal and gravitational forces of sun and moon. They influence estuaries mainly through barotropic processes arising from an oscillating pressure gradient (Simpson and Sharples, 1991; Officer, 1976). These pressure gradients then drive a circulation into and out of the estuary mouth, leading to tidal currents in the estuary. Most of the tidal energy that reaches the continental shelf is not reflected back into the deep ocean but dissipated in the shelf waters due to friction created in the bottom boundary layer and penetrating up the water column (Simpson, 1998). Through the friction, energy from the flow is transformed into turbulent eddies, inducing stirring. A large proportion of the turbulent kinetic energy is transferred into several decreasing scales of turbulent energy, down to molecular turbulence. If, however, the water column is stratified, some of the turbulent kinetic energy is also used to induce vertical mixing (Simpson, 1998). Apart from inducing stirring, tides can also lead to periodic stratification where horizontal density gradients exist. The vertical shear inserted by tides acts on the existing horizontal density gradients (Simpson et al., 1990). This can, if

horizontal density gradients are sufficiently strong, lead to distortions of the previously vertical isohalines due to surface layers being able to move faster than bottom layers, thus inducing stratification during ebb. In the flood the tide forces heavier water on top of lighter water. This leads to instability and buoyancy production of TKE (Turbulent Kinetic Energy) and then to vertical mixing contributing again to vertical isopycnals and to horizontal gradients, thus introducing periodic fluctuations. This process is called Strain-Induced Periodic Stratification (SIPS). Varying bathymetries can furthermore lead to the so-called tidal rectification, in which residual currents are developed due to the tidal waves travelling over varying topography, often creating a net outflow in deeper channels and a net inflow in more shallow areas (Li and O'Donnell, 1997).

Wind can affect estuarine dynamics in a number of ways: remote wind can have effects on the density field and, through a rise or fall of the sea-level at the bay mouth, force the sea level and currents in the estuary. Furthermore local wind over the estuary can directly lead to surface currents. Through the shear stress that the moving air exerts on the water surface, friction can lead to mixing. Waves from distant and local wind can further lead to increased mixing of the water column. Wind forcing depends both on magnitude and direction of the wind and can also induce significant wave stirring induced by non-local winds (Simpson, 1997).

Atmospheric forcing can influence the stratification of the water column of estuaries by warming or cooling the surface layer or inducing buoyancy at the water surface through rain (Simpson et al., 1990).

Flushing times in estuaries vary largely and depend on various factors, including freshwater discharge and tidal forcing.

Several authors including Piedracoba et al. (2005), Chao (1988) and Lencart e Silva (2007) have suggested that estuarine plumes can be arrested under certain conditions, leading to increased flushing times in the estuary. Two mechanisms that can lead to this arrestment are:

- downwelling winds leading to the partial blocking off of the estuary mouth;
- the buoyancy-stirring interaction induced by large tidal variations leading to turbulence modulations, as explained theoretically by Linden and Simpson (1988).

Linden and Simpson (1986) and Linden and Simpson (1988) undertook laboratory experiments on the influence of turbulence on mixing and frontogenesis and compared their results to three case studies. Through air bubbles, turbulence was induced to a fluid containing a horizontal density gradient. Those authors suggested that, during periods of large turbulence e.g. through tidal mixing, the water column was vertically mixed and baroclinic circulation was weak. When turbulence was decreased, the baroclinic circulation accelerated while the water column stratified. A vertical density gradient developed through the denser fluid having been advected underneath the lighter fluid. The flow furthermore transported mass horizontally. Depending on the duration of the absence of turbulence, a front developed, in which the horizontal density gradient was increased. Once turbulence was increased again, the water column mixed vertically, reducing baroclinic circulation. Density was therefore transported horizontally through turbulence in the phases where air bubbling was increased and through baroclinic circulation in the absence of bubbles, with the latter being more effective. Linden and Simpson (1988) therefore concluded

that the exchange through a cross-gradient section is greater when the baroclinic circulation has more time to develop, i.e. periods between turbulence are larger.

This study will concentrate on the second possible mechanism triggering the arrestment of estuarine plumes. The study area is Maputo Bay in Mozambique.

Maputo Bay is a shallow, subtropical estuary with a surface area of 1875 km². It is tidally-energetic with a large spring:neap tide ratio and characterised by highly varying river run-off. Its coastal resources are economically important for the area. Ravikumar et al. (2004) have shown that salinity can regulate the nutrient cycle in mangrove estuarine ecosystems. Salinities outside the 20 – 30 range will hamper production in the mangroves and affect the early life stages in mangrove habitats that sustain the economically important shrimp stocks (Monteiro and Marchand, 2009). The salinity of Maputo Bay is, for a part, controlled by dam systems of its main rivers. The density-driven circulation is strongly influenced by the neap-spring cycle. Here, a candidate mechanism for the arrestment of the plume is found in the wet season during spring tide, associated with turbulent mixing. During neap tide, the plume can then spread offshore. Lencart e Silva (2007) has suggested the occurrence of this arrestment of estuarine plumes induced by the large freshwater discharge in the wet season, in combination with decreased density forcing during high mixing periods associated with spring tide. This arrestment can influence salinities in the bay, decreasing salinities during times of arrestment.

The above-mentioned phenomenon in Maputo Bay has in the past been suggested from observations. In this study, modelling will be applied to research the conditions under which the arrestment as well as the release of the estuarine plume occurs. The three-dimensional model Delft3D-flow will be applied, using a set of scenarios and investigating flushing times under varying river discharge and tidal conditions. The dissertation will be concerned with the determination of conditions of the storage and release of the estuarine plume in Maputo Bay. A passive tracer will be introduced into the model to determine flushing times. A cross-section across the estuary opening will help determine stratification, velocities and salinity structures at this interface between the estuary and the shelf region.

The influence of varying discharge ratios of the two main rivers Incomati and Maputo will be investigated to find out the relative importance of the two rivers in setting the salinity and density field as well as influencing flushing times.

A set of scenarios of varying total discharge, discharge ratios between the rivers Incomati and Maputo as well as the timing of the discharge in wet and dry season conditions as well as within the spring-neap cycle is developed. A number of runs are conducted with varying durations of discharge to investigate whether managing the duration of the discharge can help maintaining salinities within the 20-30 range, providing optimal conditions for the bay's ecosystem.

The aim of this dissertation is to investigate:

- Possible conditions of the arrestment and release of the estuarine plume;
- The influence of different amounts of discharge of the Incomati and Maputo Rivers into Maputo Bay;

- The influence of the timing of the discharge in the spring-neap tidal cycle on the bay dynamics and flushing times;
- The relative influence of the rivers Incomati and Maputo on the bay dynamics and flushing times;
- The influence of varying discharge durations on bay-average salinities.

Getting a better insight into the flushing times in estuaries is crucial to understanding the estuarine dynamics. Firstly, maintaining a maximum salinity can be important for the sustainability of economically important resources. Secondly, the dilution and transportation of pollutants in the estuary also depend on the flushing times and can strongly be influenced by an arrestment of the estuarine plume.

The following sub-chapter will focus on the state of the art on the arrestment of estuarine plumes. For an introduction and state of the art on the study area Maputo Bay, please refer to Chapter 2.

1.2 The Arrestment of Estuarine Plumes: State of the Art

Literature suggests that local onshore winds as well as remote winds on the continental shelf may lead to a decrease of flushing of estuaries. Furthermore can the buoyancy-stirring interaction induced by large tidal variations lead to turbulence modulations which in turn can arrest the estuarine plume during high mixing of spring tide. This chapter will give a review on some of these investigations. Firstly, an overview of previous investigations concerning wind-induced forcing will be given. Next, an introduction on tide-induced arrestment is given.

Wind-induced

Local wind-induced forcing

Geyer (1997) investigated the effect of local on- and offshore winds on the flushing times of two shallow estuaries in Cape Cod, U.S.A., through observations. That author found that in both, the Childs River estuary and the Quashnet River estuary, onshore winds reduce estuarine circulation and along-estuary salinity gradients increase due to the accumulating freshwater. Through the inhibited estuarine circulation, flushing rates are reduced. Offshore winds, on the other hand, flush out estuarine water, reduce along-channel salinity gradients and lead to increased flushing. That author furthermore found that a constriction, in this case bridge abutments, restrict the flushing of both estuaries.

DeCastro et al. (2003) used a combination of observations and the hydrodynamic model MOHID to examine the influence of local winds on the exchange between the shelf and the Ria de Ferrol, one of the Galician Rias Baixas. They found that the wind-induced flow through the 350 m-wide Strait of Ferrol under real wind conditions can be around 1.5 % of the total flow (20 m^3s^{-1} due to wind, 1200 m^3s^{-1} due to tidal forcing and 2.5 m^3s^{-1} due to freshwater input in summer) and is therefore the main cause of residual circulation. Wind forcing leads to an asymmetric ebb-flood

cycle, with surface currents being offset by 0.5 ms^{-1}, with the offset decreasing with depth and eventually changing sign in deeper layers.

DeCastro et al. (2000) investigated the influence of tides and local winds on the circulation in the Galician Ria de Pontevedra through observations. They found that wind speeds higher than 4 ms^{-1} can dominate the surface currents, leading to a reversal of the normal tidal circulation. During moderate offshore winds with average wind speeds of 5-7 ms^{-1}, surface currents were controlled by winds, leaving the Ria even against tidal forcing, while bottom layer currents were tidally controlled. Moderate onshore winds with wind speeds of 7-12 ms^{-1} forced shelf water to enter the estuary through surface layers, while bottom layers behaved according to the tidal regime, leaving the estuary.

Chao (1988) examined the behaviour of estuarine plumes during different wind events through the application of a three-dimensional primitive-equation model. That author found that a local onshore wind can inhibit gravitational circulation in an estuary, destroy the plume structure on the shelf and accumulate fresh water in the estuary. Once the wind relaxes, a new plume quickly develops, transporting the lower-salinity water out of the estuary, onto the shelf. If the onshore wind is relatively weak compared to buoyancy forcing, a three-layer circulation pattern can also develop, with a landward surface current of shelf water directed into the estuary, below which the positive estuarine circulation is found.

Distant wind-induced forcing

Various investigations over the last years have shown the possibility of the arrestment of estuarine circulation induced by remote winds, often related to downwelling-events blocking the outflow of estuarine surface waters.

Álvarez-Salgado et al. (2000) investigated the influence of upwelling and downwelling winds on the Galician Rias Baixas through observations and a two-dimensional box model. These authors found that during downwelling events, surface shelf waters piled up along the coast and entered the ria, preventing ria waters from leaving the estuary.

Prego et al. (1990) found southerly winds blocking the interchange between the shelf and the Ria de Vigo, leading to a half-closed estuarine circulation due to downwelling.

Piedracoba et al. (2005) investigated the influence of remote and local winds on the residual circulation and thermohaline variations in the Ria de Vigo through observations in 2002. Those authors found that southerly winds lead to a reversed circulation pattern in which the fresh water from river discharge was piled up in surface layers while an outgoing current was established in the bottom layers, transporting higher salinity waters out of the estuary. These findings were also confirmed by Gilcoto et al. (2007).

Chao (1988) applied a three-dimensional primitive-equation model to study the effect of local and shelf winds on estuarine plumes. That author found a hindering of the buoyancy-driven outflowing surface current due to the Ekman drift being directed onshore, leading to surface

currents being weakly downwind. Freshwater export from the estuary onto the shelf was retarded and lead to an increased content of fresh water in the estuary.

Dale et al. (2004) applied a two-dimensional box model to the Ria de Pontevedra, Galicia, to research water exchange with the shelf and flushing times in the estuary. They found that with the presence of a downwelling front in September and October 1998, freshwater was retained in the estuary, with gravitational circulation having been suppressed and flushing times increased in both the inner and central parts of the estuary.

Valle-Levinson et al. (1998) observed the passage of two downwelling wind periods near Chesapeake Bay with similar magnitudes and durations which produced very different hydrodynamic conditions in the bay. One wind event occurred during neap tide and lead to significant stratification after the wind had ceased. The other wind event occurred during spring tide and had produced much weaker stratification. In the wind event that occurred during neap tide, stirring through tides was less strong, therefore stratification developed in the estuary, increasing flushing. After the event that occurred during spring tide, on the other hand, tidal mixing was much stronger, decreasing vertical salinity gradients and retarding the flushing of the accumulated freshwater. Those authors therefore suggest that stronger mixing such as through tides can retard flushing.

Tide-induced

Another possible mechanism for the arrestment of estuarine circulation is related to tidal forcing, where a large spring: neap ratio exists.

The tides influence the flushing of an estuary through four mechanisms:

- Tidal shear dispersion;
- Chaotic dispersion;
- Tidal rectification;
- Tidal advection into shelf currents.

Chaotic dispersion occurs when an oscillatory field is superimposed on a constant field, resulting in a chaotic field. This may occur as a combination of tidal rectification and tidal velocity as described by Ridderinkhof and Zimmermann (1992).

The laboratory experiments by Linden and Simpson (1986) and Linden and Simpson (1988) that were explained in the introduction have shown the correlation between turbulence, stratification and mixing. Linden and Simpson (1988) furthermore compared their laboratory experiments with field observations in three regions where turbulence is induced through tidal stirring.

One of these is Spencer Gulf, a shallow bay in Southern Australia, characterised by hypersaline conditions, making Spencer Gulf a negative estuary. Nunes and Lennon (1987) found that during periods of low turbulence due to light winds in combination with the absence of semidiurnal currents, stratification developed. This occurred on a 14-day cycle due to the equality in amplitude of the lunar and solar semidiurnal tidal constituents. Those authors observed the

development of stratification arising from horizontal density advection when turbulence was very weak. A buoyancy driven circulation developed and adjusted geostrophically to form a large cyclonic gyre. A boundary current into the gulf transported lower salinity water along the western coast while a counterflow transported the saline gulf water along the eastern coast out of the gulf, in accordance with the effect of the Earth's rotation. Salinity differences between in- and outflow of >1 were possible and the gyre therefore lead to the flushing of excess salt from the gulf and the renewal of its water. The onset of winds or tidal currents was able to erode this gyre by mixing the water column again.

Another case study discussed by Linden and Simpson (1988) is that by Simpson et al. (1988), who investigated the control of tidal straining, density currents and stirring on estuarine stratification. Observations in Liverpool Bay showed an alternation between stratified and vertically mixed conditions with semidiurnal frequencies. Maximum stratification occurred during low water slack and Simpson et al. (1988) assumed that this alternation was due to tidal straining. Those authors furthermore found lower frequency periods of more permanent stratification coinciding with weak mixing during neap tides, probably due to reduced tidal mixing allowing an increase in the density current. In Liverpool Bay, those authors therefore concluded from observations and simulations that the semidiurnal signal of stratification pulses was intensified during spring tide and weakened during neap tides, when tidal mixing was weaker. They furthermore argued that in stronger tidal stream amplitudes tidal stirring will become more relevant in comparison with straining, with complete mixing occurring over most of the semidiurnal cycle, with strain induced stratification occurring near neap tide only.

Lencart e Silva (2007) observed the onset and breakdown of stratification during the wet season in Maputo Bay. During neap tides, when tidal stirring was at its minimum, a vertical density gradient established and baroclinic currents were found. A 3-dimensional hydrodynamic model was applied and results suggested that during high mixing of spring tides the estuarine plume was arrested, decreasing overall salinities of Maputo Bay. During low mixing of neap tides, the estuarine plume rapidly spread offshore, with a counter flow of saline water into the bay.

1.3 Work Structure

The present work is divided into 6 Chapters. Chapter 1 gives an introduction into general estuarine dynamics, the aim of this dissertation, as well as the state of the art on the arrestment of estuarine plumes.

The study area Maputo Bay will be introduced in Chapter 2, focusing on the hydrodynamics and also including the regional oceanographic context. Chapter 3 will be concerned with the methodology, giving an overview of the numerical model used, describing the technical data applied in this case, presenting the calibration and validation results and introducing the sets of model runs that were used.

In Chapter 4 the results for the runs during the dry season will be presented and discussed.

Chapter 5 consists of the results and discussion of the wet season runs and Chapter 6 will describe final conclusions.

2 Study Area

This chapter introduces the study are Maputo Bay. In section 2.1, a general introduction will be given, followed by the meteorologic conditions in section 2.2. Next, the hydrography and hydrodynamics are presented in section 2.3, including tidal and river forcing. Section 2.4 introduces the regional oceanographic context off the coast of Mozambique.

2.1 Introduction

Mozambique is situated at the eastern coast of Africa, between 10° 27’ and 26° 52’ South and 30° 12’ and 40° 51’ East (see Figure 1).

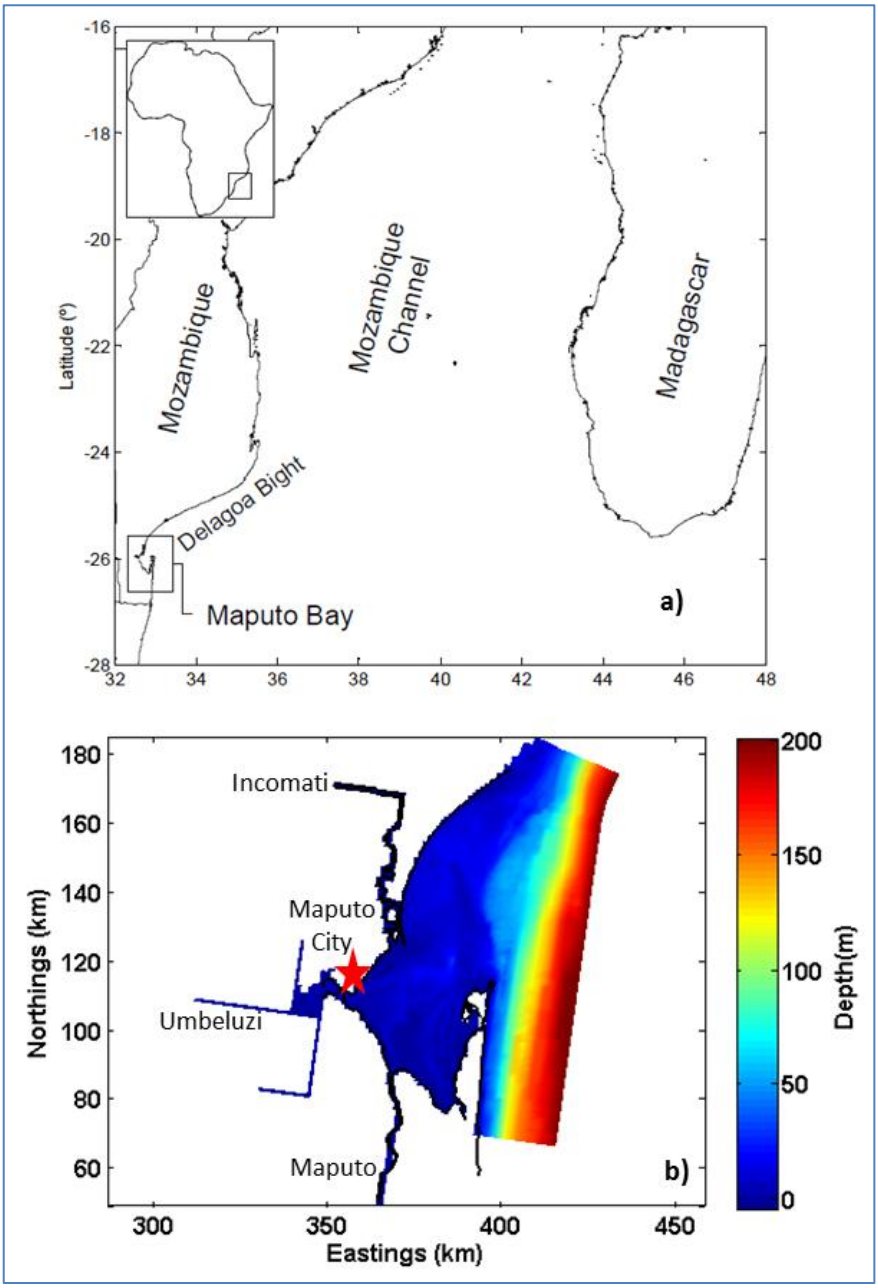

Figure 1: Location and bathymetries of Maputo Bay a) Maputo Bay in a continental context (from Lencart e Silva, 2007), b) bathymetries of Maputo Bay and location of Maputo City.

In 2007, its population was estimated to be 17.2 million people, with an annual growth rate of 2.5 % (Hoguane, 2007). Mozambique has a coastline of approximately 2700 km, characterised by a large variety of ecosystems, including beaches, dune systems, coral reefs, mangrove swamps and estuaries (Canhanga, 2004; Sete et al., 2002).

Maputo Bay is located in the South of Mozambique with its centre at 32°47' East 26°03' South (Lencart e Silva, 2007). The bay covers a total area of approximately 1875 km^2. In the North, it opens towards the Indian Ocean, whereas the East is limited by Machangulo Peninsula, Inhaca Island, Ilha dos Portugueses and several unvegetated islands in between, surrounded by shallow tidal channels and intertidal flats (Cooper and Pilkey, 2002). The city of Maputo is located on the western side and has a population of 2 million people (Sete, 2002). Water depths in the bay are on average around 5 m and reach approximately 30 m at the 18 km wide opening. An area of around 138 km^2 is covered by sand banks (Hoguane, 1994) and the bay's bottom is sandy in the eastern part and muddy in the western part (Canhanga, 2004). The bay is surrounded by mangrove swamps such as the Ponta Rasa mangrove swamp on Inhaca Island, 70% of which is covered by mangroves (Hoguane et al., 1999). The port of Maputo is located within the bay and is one of the three largest ports of Mozambique, being an important infrastructure for not only Mozambique but also the neighbouring countries such as South Africa and Swaziland (Canhanga, 2004; Hoguane, 2007). The port constitutes a possible source of pollution to the area, e.g. through oil, cleaning tanks and rubbish from boats.

The bay is also considered an important fishing ground due to the mangrove swamps and high productivity. The local population benefits from the collection and capture of fish, crabs and shellfish (De Boer and Longamane, 1996). Especially shrimp is an economically important resource for the area (Hoguane, 2007). Inhaca is also one of the most important tourism centres of Mozambique (Hoguane, 2007).

Due to the drainage of several international rivers into the bay, as well as the main industries of Mozambique located in the nearby areas and inadequate domestic waste treatment facilities for the large population of Maputo, the bay is prone to pollution (Sete et al., 2002). Hoguane (2007) describes five main pressures for Mozambique's coastal zones, most of which are also relevant for the Maputo Bay area: coastal erosion, deforestation (especially of mangroves), deficiencies in the conservation of fish stocks, marine pollution and an inadequate distribution of energy, leading in turn to further deforestation due to increased use of biomass energy. Especially marine pollution can be a problem in Maputo Bay. Many cities in Mozambique have an incapacity to treat urban discharges appropriately, which leads to their discharge into the adjacent rivers and eventually reaching the bay.

2.2 Meteorologic Conditions

Average wind speeds are around 4 ms^{-1} and can therefore be characterised as relatively light, with sea breezes often developing in the afternoon (Lencart e Silva et al., 2010). Those authors therefore suggest that winds have a limited influence on the bay hydrodynamics, compared to the strong energy input from tidal forcing. Wind speeds at Mavalene airport station between March

2003 and April 2004 never exceeded 15 ms^{-1}. Wind directions were mainly northward with less frequent W-E or SSW-NNE directions (Lencart e Silva, 2007).

The climate is between tropical and subtropical, with two pronounced seasons: wet season between October and March and dry season between April and September (Canhanga, 2004). The mean annual rainfall is 884 mm (de Boer et al., 2000).

Monthly average minimum and maximum temperatures for Maputo are shown in Table 1.

Table 1: Monthly average maximum and minimum air temperatures in Maputo (Climatemps, 2013).

	Jan	Feb	Mar	Apr	May	Jun	Jul	Aug	Sep	Oct	Nov	Dec
Max	30	30	30	29	27	25	25	26	27	28	28	30
Min	22	22	21	19	16	14	14	15	16	18	20	21

2.3 Hydrography and Hydrodynamics

Three main rivers flow into Maputo Bay: the Maputo, the Incomati and the smaller Umbeluzi (see Figure 1. The rivers Tembe and Matola also discharge in Maputo Bay but carry much smaller volumes of water. The Incomati makes up around 57 % of the freshwater discharge into the bay, being characterised by a mean discharge of 133 m^3s^{-1}. The Maputo River accounts for a further 38 % of runoff, with a long-term mean discharge of 89 m^3s^{-1}, whereas the remaining 5% of runoff come from the Umbeluzi River (Milliman and Meade, 1983). River discharge is characterised by a strong seasonal cycle, with maximum values usually occurring in the wet season between November and April, and reaching values exceeding 1000 m^3s^{-1} during extreme events such as in a catastrophic flooding event with extreme rainfall in the year 2000 when peak discharges were up to 6827 m^3s^{-1} (Lencart e Silva et al., 2010). Inter-annual discharge also shows strong variations, with a variation coefficient of 50-65 % for the Incomati River (Vas and v.d. Zaag, 2003). Since the 1960s, several dams have been built, influencing river runoff into Maputo Bay. Please refer to Vas and v.d. Zaag (2003) for an overview of all major dams of the Incomati basin.

The rivers are clearly influenced by the wet season – dry season cycle: both, the Umbeluzi and Maputo rivers have 67-82 % of their total runoff occurring between January and April and 37-52 % of the runoff occurring in the peak flood period in February and March (Sete et al., 2002). The total volume of fresh water entering the bay is estimated to be around 6 km^3y^{-1} (Hoguane and Dove, 2000).

Sete et al. (2002) observed annual mean sea level variations in Maputo Bay, with maximum sea level coinciding with the wet season (January) and minimum values around 170 mm lower in the dry season (August). Those authors therefore conclude that intra annual sea level variations in Maputo Bay are influenced by rainfall or runoff in the river catchments flowing into the bay.

Canhanga and Dias (2005) studied the tidal characteristics of Maputo Bay through the application of the numerical model SIMSYS2D and observations of free surface elevations in the harbour of Maputo Bay. They found that phases of M_2 and S_2 are 122° and 164°, respectively, and observed a

strong fortnightly modulation, indicating relatively large differences between spring and neap tides, with spring tidal range being around 3 m and neap tidal range being just around 1 m. Those authors furthermore found that the semidiurnal M_2 and S_2 constituents contribute around 90 % of the total astronomical tide, whereas the amplitude of the K_1 constituent is very small, being only 5% of the amplitude of the M_2 constituent. Canhanga and Dias (2005) therefore suggest that constituents with an amplitude smaller than that of K_1 may be neglected in the tidal analysis of Maputo Bay. Tidal amplitudes decrease inside the Bay, with M_2 varying between 0.96 m at the mouth and 0.65 m inside the bay at the Espirito Santo Estuary, whereas the S_2 amplitude varies between 0.47 and 0.32 m and the amplitude of K_1 varies between 0.057 m and 0.045 m. The tidal phase increases towards the inshore zone, with the increase being more pronounced in smaller channels compared to the bay's central part. The form factor

$$F = \frac{O_1 + K_1}{M_2 + S_2} \quad \textbf{(1)}$$

calculated from the amplitudes of the most important diurnal and semidiurnal constituents is smaller than 0.25 across the complete bay, mostly varying near values of around 0.06, confirming the semi-diurnal character of Maputo Bay. Maximum tidal currents are found in the main channel and are around 1 ms^{-1} and 0.5 ms^{-1} for M_2 and S_2, respectively. Taking into account the phase differences between free surface elevations and currents, the tide in Maputo behaves as a mixed wave, showing characteristics of both, a standing wave component and a progressive wave component. This mixed wave character was also observed by Lencart e Silva (2007), who concluded that the tide is close to a standing wave with only a small progressive component, indicated by a short lag between the bay's mouth and locations further inside the bay.

Lencart e Silva et al. (2010) investigated the interactions between tidal stirring and the strongly varying river runoff in Maputo Bay, based on observations and the application of the three-dimensional hydrodynamic model Delft3D-flow. Their observations were in concordance with the previously observed dominance of semi-diurnal tidal constituents, with peak near-surface currents during spring tide being 1.2 ms^{-1} during flood and 1.0 ms^{-1} during ebb, while neap tide currents only reached velocities below 0.2 ms^{-1}. This semi-diurnal characteristic can also be found in the energy dissipation per unit volume, which Lencart e Silva et al. (2010) calculated using

$$\varepsilon = C_d \rho \frac{|\bar{U}|^3}{h} \quad \textbf{(2)}$$

where C_d is the bottom drag coefficient, ρ is density of seawater, $|\bar{U}|$ is the magnitude of the tide-averaged depth mean tidal current magnitude and h is water depth. During spring tides, ε reaches approximately 0.1 Wm^{-3} over most of the bay, with a small area near Inhaca Island reaching 1.0 Wm^{-3}, indicating pronounced mixing during spring tide. During neap tide, on the other hand, values of energy dissipation are two to three orders of magnitude smaller, indicating significantly lower levels of stirring. Tide lags between Clube Naval at the city of Maputo and Inhaca Island of 8 and 12 minutes, for M_2 and S_2, respectively, were found by Lencart e Silva (2007).

Lencart e Silva et al. (2010) observed bay-average salinities between 35.6 at the end of the dry season and 33.5 during the wet season, when freshwater input was largest. Bay-average water

temperatures varied between 21°C in July and 27.5°C in February, which lead to a stratifying effect due to the rate of heating of

$$\left(\frac{\partial \phi}{\partial t}\right)_{heat} = \frac{\alpha g \dot{Q}}{2c_p} \sim 3x10^{-6} Wm^{-3} \quad (3)$$

where α is 10^{4}°C^{-1}, c_p is the specific heat and $\dot{Q}$ is the amplitude of the rate of heat exchange through the sea surface, defined as:

$$\dot{Q} = \omega \frac{c_p \rho h \Delta T}{2} \quad (4)$$

where ω is the angular frequency of the annual cycle, ρ is the density of sea water and h is the water depth.

Those authors also compared this with the stirring effect:

$$\left(\frac{\partial \phi}{\partial t}\right)_{mix} = eC_D \rho \frac{|\overline{U}|^3}{h} = \frac{4}{\pi} eC_D \rho \frac{U_{M2}^3 + s_2}{h} \sim 4x10^{-4} Wm^{-3} \quad (5)$$

where e is the mixing efficiency and U_{M2+S2} is the tidal stream amplitude.

This shows that during spring tide stirring is much stronger than the stratifying effect from heating. During neap tide, stirring still meets the values of stratification from heating, even though tidal energy is much smaller. As stratification occurs and does not seem to be induced by heating, Lencart e Silva et al. (2010) conclude that the estuarine circulation and tidal straining effects must be responsible for the introduction of stratification.

Lencart e Silva (2007) calculated the stratifying effect of freshwater distributed uniformly at the surface for large river runoff:

$$\left(\frac{\partial \phi}{\partial t}\right)_{fw} = \frac{g}{s} \dot{P} \Delta \rho = 3x10^{-4} W.m^{-3} \quad (6)$$

where $\dot{P}$ is the freshwater flow from rivers distributed as rainfall, s is the salinity and $\Delta\rho$ is the density difference between fresh and salt water (=25 kg.m^{-3}).

Comparing the mean potential energy anomaly φ values throughout the year, Lencart e Silva et al. (2010) observed hardly any stratification during dry season and some stratification with φ values of around 1 Jm^{-3} during spring tides in the wet season. They further investigated the wet season stratification-stirring competition along a section of the bay between Inhaca Island and Macaneta sand spit. CTD measurements showed pronounced stratification during neap tide, especially in the deeper parts of the section, with φ ranging between 30 and 80 Jm^{-3}, implying the stratifying effects of estuarine circulation dominating over mixing effects. During spring tide, the section was mixed for most of the tidal cycle, only showing little stratification in the deeper parts around low water, with φ reaching approximately 10 Jm^{-3} associated with larger velocity shear and therefore tidal straining. Wind stirring was found to be negligible compared to tidal stirring over most of the tidal cycle. Lencart e Silva et al. (2010) concluded that Maputo Bay's large variation of freshwater input over the year leads to a vertical homogeneity of the water during the dry season and horizontal density gradients during the wet season due to the input of large amounts of fresh water.

Through the application of a three-dimensional hydrodynamic model, Lencart e Silva (2007) investigated residual currents in Maputo Bay and found a flow into the bay through the deeper, south-eastern channel and an outward flow through the north-western, shallow areas, independent of tidal regime. These two separate flow cells cover the complete water depth of the bay during the dry season, with increased tidal forcing during spring tide leading to larger residual current velocities. During the wet season, spring tide conditions are similar but neap tide conditions are characterised by an estuarine circulation, with the deeper inward cell showing increased velocities while the area of outward flow expands towards the centre and top of the bay's opening. Residual velocities for shallow water constituents were found, with velocities of 0.05 ms^{-1}. Lencart e Silva (2007) assumes that these are due to tidal rectification, produced locally by the varying bathymetry over which the tidal currents propagate, as there was no evidence of these features in sea surface elevations. Furthermore did that author find the less intense vertical tidal mixing during neap tides leading to vertical gradients. These gradients in turn force a strong estuarine-type circulation, transporting surface water out of the bay and deeper, more dense water into the bay, thus increasing transport. During increased tidal mixing associated with spring tides, the water is vertically mixed, leading to an arrestment of the estuarine circulation and a retainment of much of the freshwater in the bay.

Lencart e Silva (2007) also applied different models to calculate the flushing time of Maputo Bay. A tidal prism model produced wet season mean flushing times of 9 and 17 days, for bay water return fractions of 0.8 and 0.9, respectively. Applying Delft3D-flow to Maputo Bay, that author found flushing times varying with freshwater input and tidal velocities, with a flushing time of 24 days during maximum river runoff and 37 days during no river runoff but with maximum tidal forcing. This indicates that Maputo Bay has a larger exchange efficiency when forced by buoyancy (fresh water from river discharge) than by tidal processes.

The freshwater discharge from the several estuaries leads to Maputo Bay being characterised by a gulf-type region of fresh water influence (ROFI), rather than a classic estuary. Simpson defines a ROFI as a "*region between the shelf sea regime and the estuary where the local input of freshwater buoyancy from the coastal source is comparable with, or exceeds, the seasonal input of buoyancy as heat which occurs all over the shelf*" (1997).That author further argues that a gulf-type ROFI is one in which the coastal topography retains the buoyancy input close to its source through constraining by topography. The exchange flow, exporting buoyancy, becomes similar to that of a classical estuarine circulation.

2.4 Regional Oceanographic Context

Saetre and Jorge Silva (1982) classified the water masses along the Mozambican coast up to a depth of 1000 m into four types: warm, low-salinity surface waters in the upper 100-150 m originating from the South Equatorial Current or the centre of the sub-tropical gyre of the Indian Ocean, sub-surface waters with a salinity maximum between 150 and 300 m depth, central water at a depth of 300-600 m and intermediate water of low salinity from the Antarctic or higher salinity water from the northern Indian Ocean.

Surface waters off the coast of southern Mozambique, near Maputo Bay, were found to be characterized by temperatures varying from a maximum of 26-29°C between January and March, to a minimum of 22-25°C between July and September. Surface salinities showed lowest values of 34.4-35.2 between January and March and maximum salinities of 35.3-35.5 occurring at the end of the dry season between October and November (Sete et al., 2002).

Lutjeharms and Jorge da Silva (1988) investigated the existence and characteristics of the cyclonic Delagoa Bight eddy, the Delagoa Bight being the shelf area adjacent to Maputo Bay. Through different sets of hydrographic data as well as sediment patterns they found that an eddy-like feature is located in the bight, covering most of the continental shelf as well as the terrace landward of the Mozambique Current. The feature has a high consistency, being found most or even all the time, and has a diameter of approximately 180 km. Those authors suggest the constriction of the shelf width at the Delagoa Bight causing the development of an upstream coastal countercurrent which forms the landward border of the Delagoa Bight lee eddy and advects warm water towards the North. Unlike in the surrounding areas, subtropical water is not found in the eddy. Instead, the core consists for a large extent of Antarctic Intermediate Water, upwelled from greater depths.

Quartly and Srokosz (2004) used chlorophyll concentrations obtained from satellite data to trace currents and eddies in the Southern Mozambique Channel through chlorophyll concentration fronts. Their results indicate that the previously assumed flow concept of the South Equatorial Current should be discarded. This previous concept consisted of the South Equatorial Current, when reaching Madagascar, dividing into a northward and a southward branch, the southward branch turning westward to feed into the Madagascar Current and forming the Argulhas Current. Instead, those authors suggest a more variable flow field. They found 200 km-diameter features with anticyclonic circulation travelling southward down the western side of the channel, 5-6 of which were observed per year. The Delagoa Bight eddy previously described by Lutjeharms and Jorge da Silva (1988) was confirmed and is expected to be enforced by anticyclonic eddies passing by seaward of the Delagoa Bight eddy. Furthermore were 250 km-diameter cyclonic eddies found near the Southern tip of Madagascar, which are assumed to originate further northward but only become apparent under the influence of the west of Madagascar, in the presence of coastal waters which are advected around the eddies. These eddies then travel west- to south-westward. A retroflecting East Madagascar Current was only found in some instances. Quartly and Srokosz's findings are summarised in Figure 2, showing the long term mean flow (a) as well as varying features (b) of the Southern Mozambique Channel.

Significant wave heights in the high seas off Maputo Bay are between 7 and 11.7 m, with directions coming from mainly southern and eastern sides, whereas the waves in shallow water closer to the coast largely vary in height and direction (JIC Limited, 1998, in Hoguane, 2007).

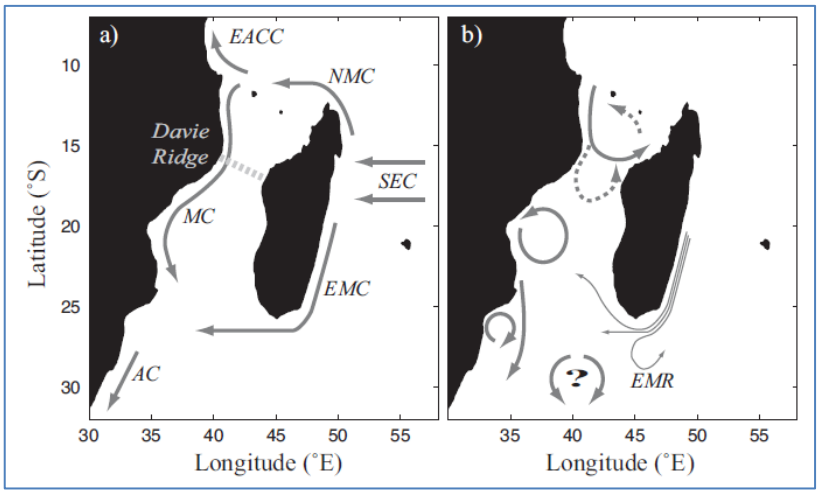

Figure 2: Regional oceanographic context of Maputo Bay; a) long-term flow conditions, b) variability in features. Symbols: SEC: South Equatorial Current, NMC: North Madagascar Current, EACC: East African Coastal Current, EMC: East Madagascar Current, MC: Mozambique Current, AC: Argulhas Current, EMR: East Madagascar Retroflection. (Quartly and Srokosz, 2004).

3 Numerical Modelling

To investigate the hydrodynamics of Maputo Bay, the three-dimensional model Delft3D-flow was applied. This Chapter will introduce the methodology that was used. First, an overview of the hydrodynamic model and its features is given. Next, the model calibration and validation as well as the final model specifications are given. All scenarios that were applied are introduced and the limitations of the model are discussed. The data processing methods applied to transform the model output into the results is described.

3.1 Delft3D-flow

Delft3D-flow is a software for computations of coastal, estuarine and river areas and was developed by Deltares in the Netherlands. While the software Delft3D is able to carry out simulations for sediment transports, flows, waves, water quality, morphological developments and ecology, this chapter will only focus on the flow module, Delft3D-flow, used for this study.

The model used in Delft3D-flow is based on the horizontal equations of motion, the continuity equation and the transport equations for conservative constituents. Various forcing mechanisms and other features are included and a range of options are given to define the horizontal and vertical coordinate systems, initial conditions, boundary conditions, friction, turbulence and other variables (Deltares, 2011).

Features

Delft3D-flow can be applied to both, two- and three-dimensional hydrodynamic modelling, being able to calculate transport phenomena and non-steady flow. Various forcing factors, including

tides, fresh-water discharge, wind, density stratification, thermal heating and cooling and Coriolis force can be taken into account.

The coordinate system can be Cartesian (in metres) or spherical (in decimal degrees). Horizontal grids in Delft3D-flow are staggered, meaning that the different quantities such as water levels, salinities and velocities are defined in different locations of the grid.

The particular staggered grid used in Delft3D-flow is the so-called Arakawa-C grid. In this grid, water level points are defined in grid centres, while velocities are defined perpendicular to the gird cell faces where they are situated. This approach has several advantages, such as an easier implementation of boundary conditions, the use of a smaller number of discrete state variables without losing accuracy, as well as preventing spatial oscillations in water levels (Deltares, 2011).

For the vertical grid, up to 100 layers can be developed and each layer's thickness can be specified. By giving layers non-uniform thickness, the resolution in areas of interest, such as the surface or bottom layer, as well as the pycnocline, can be improved.

A choice between the Z-model and the sigma-coordinate approach is given for the vertical grid direction (see Figure 3).

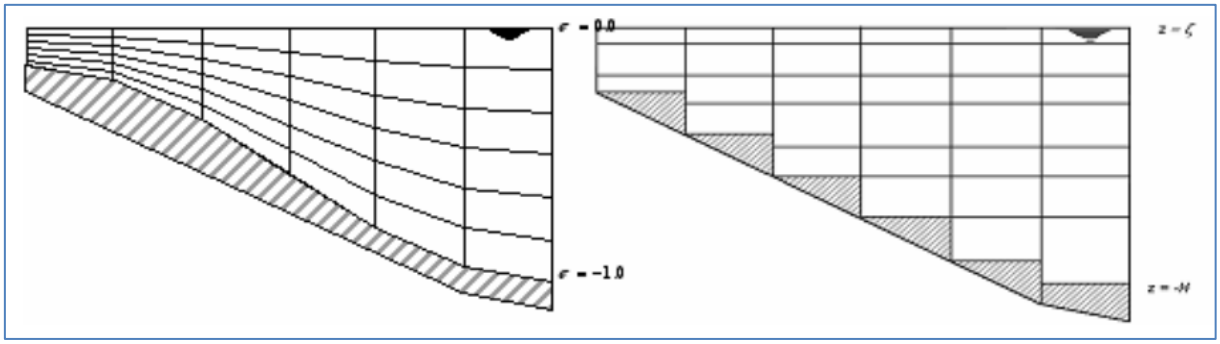

Figure 3: Comparison of the sigma-grid (left) and the Z-grid (right) (Deltares, 2011),

The sigma coordinate system is characterized by layers following the bottom topography and the free surface rather than layers being of uniform depth over the whole area. The number of layers is constant over the whole model domain. This approach therefore provides a refined vertical resolution in shallow areas (Deltares, 2011).

The σ co-ordinates are defined as:

$$\sigma = \frac{z - \zeta}{d + \zeta} = \frac{z - \zeta}{H} \qquad (7)$$

where z is the vertical co-ordinate in physical space, ζ is the free surface elevation above the reference plane ($z = 0$), d is the depth below the reference plane and H is the total water depth ($H = d + \zeta$).

Governing Equations

Delft3D solves the Navier-Stokes equations for incompressible fluids and considers the shallow water assumption as well as the Boussinesq assumption, taking into account variable density only in the pressure term (Deltares, 2011).

The system of equations therefore consists of the horizontal equations of motion, the continuity equation and the transport equations for conservative constituents.

Continuity Equation

The continuity equation is a mathematical statement of the conservation of mass (Officer, 1976). The depth-average continuity equation is given by

$$\frac{\partial \zeta}{\partial t} + \frac{1}{\sqrt{G_{\xi\xi}}\sqrt{G_{\eta\eta}}}\frac{\partial[(d+\xi)U\sqrt{G_{\eta\eta}}]}{\partial \xi} + \frac{1}{\sqrt{G_{\xi\xi}}\sqrt{G_{\eta\eta}}}\frac{\partial[(d+\xi)V\sqrt{G_{\xi\xi}}]}{\partial \eta} = Q \quad (8)$$

with

$$Q = H\int_{-1}^{0}(q_{in} - q_{out})d\sigma + P - E \quad (9)$$

being the contribution per unit area due to the withdrawal or discharge of water, with q_{in} being the local sources of water, q_{out} the local sinks of water, *P* being non-local precipitation, *E* the non-local evaporation and $\sqrt{G_{\xi\xi}}$ and $\sqrt{G_{\eta\eta}}$ being coefficients to transform values from curvilinear to rectangular coordinates (Deltares, 2011).

Horizontal momentum equations

The horizontal momentum equations in the *u* and *v* directions are defined as:

$$\frac{\partial u}{\partial t} + \frac{u}{\sqrt{G_{\xi\xi}}}\frac{\partial u}{\partial \xi} + \frac{v}{\sqrt{G_{\eta\eta}}}\frac{\partial u}{\partial \eta} + \frac{w}{d+\zeta}\frac{\partial u}{\partial \sigma} - \frac{v^2}{\sqrt{G_{\xi\xi}}\sqrt{G_{\eta\eta}}}\frac{\partial \sqrt{G_{\eta\eta}}}{\partial \xi} + \frac{uv}{\sqrt{G_{\xi\xi}}\sqrt{G_{\eta\eta}}}\frac{\partial \sqrt{G_{\xi\xi}}}{\partial \eta} - fv = -\frac{1}{\rho_0\sqrt{G_{\xi\xi}}}P_\xi + F_\xi + \frac{1}{(d+\zeta)^2}\frac{\partial}{\partial \sigma}\left(v_v\frac{\partial u}{\partial \sigma}\right) + M_\xi \quad (10)$$

and

$$\frac{\partial v}{\partial t} + \frac{u}{\sqrt{G_{\xi\xi}}}\frac{\partial v}{\partial \xi} + \frac{v}{\sqrt{G_{\eta\eta}}}\frac{\partial v}{\partial \eta} + \frac{w}{d+\zeta}\frac{\partial v}{\partial \sigma} - \frac{uv}{\sqrt{G_{\xi\xi}}\sqrt{G_{\eta\eta}}}\frac{\partial \sqrt{G_{\eta\eta}}}{\partial \xi} + \frac{u^2}{\sqrt{G_{\xi\xi}}\sqrt{G_{\eta\eta}}}\frac{\partial \sqrt{G_{\xi\xi}}}{\partial \eta} + fu = -\frac{1}{\rho_0\sqrt{G_{\eta\eta}}}P_\eta + F_\eta + \frac{1}{(d+\zeta)^2}\frac{\partial}{\partial \sigma}\left(v_v\frac{\partial v}{\partial \sigma}\right) + M_\eta \quad (11)$$

F_ξ and F_η represent forces due to an imbalance of horizontal Reynold's stresses, M_η and M_ξ represent external sources and sinks of momentum and the vertical eddy viscosity coefficient v_v is given by

$$v_V = v_{mol} + \max(v_{3D}, v_H^{back}) \quad (12)$$

where v_{mol} is the kinematic viscosity of water, v_{3D} is the three-dimensional part of viscosity and v_H^{back} is an ambient vertical mixing coefficient.

The Coriolis parameter *f* is given by

$$f = 2\Omega sin\varphi \quad (13)$$

and is dependent on the latitude and the Earth's rotational speed. As the Boussinesq approximation is applied, density variations are only taken into account in the baroclinic pressure terms.

Vertical Velocities

The vertical velocity *w* can be obtained from the continuity equation (Equation 8) and is defined at the iso-*σ*-layer surfaces, representing the vertical velocity relative to the moving *σ*-plane (Deltares, 2011).

$$\frac{\partial \zeta}{\partial t} + \frac{1}{\sqrt{G_{\xi\xi}}\sqrt{G_{\eta\eta}}}\frac{\partial[(d+\zeta)u\sqrt{G_{\eta\eta}}]}{\partial \xi} + \frac{1}{\sqrt{G_{\xi\xi}}\sqrt{G_{\eta\eta}}}\frac{\partial[(d+\zeta)v\sqrt{G_{\xi\xi}}]}{\partial \eta} + \frac{\partial w}{\partial \sigma} = H(q_{in} - q_{out}) \quad (14)$$

Hydrostatic Pressure Assumption

In areas where the depth is assumed to be much smaller than the horizontal length scale, vertical accelerations are considered to be small compared to gravitational acceleration and can therefore be neglected. In this case, the shallow water assumption is valid and the vertical momentum equation can be reduced to the hydrostatic pressure relation, not taking into account effects of sudden variation of bottom topography on vertical accelerations due to buoyancy variations, so:

$$\frac{\partial P}{\partial \sigma} = -g\rho H \quad (15)$$

After integration, the hydrostatic pressure assumption becomes:

$$P = P_{atm} + gH \int_\sigma^0 \rho\,(\xi, \eta, \sigma', t)d\sigma' \quad (16)$$

where P_{atm} is the atmospheric pressure.

Considering water of uniform density, the pressure gradients in the ξ and η direction are given by

$$\frac{1}{\rho_0\sqrt{G_{\xi\xi}}}P_\xi = \frac{g}{\sqrt{G_{\xi\xi}}}\frac{\partial \zeta}{\partial \xi} + \frac{1}{\rho_0\sqrt{G_{\xi\xi}}}\frac{\partial P_{atm}}{\partial \xi} \quad (17)$$

and

$$\frac{1}{\rho_0\sqrt{G_{\eta\eta}}}P_\eta = \frac{g}{\sqrt{G_{\eta\eta}}}\frac{\partial\zeta}{\partial\eta} + \frac{1}{\rho_0\sqrt{G_{\eta\eta}}}\frac{\partial P_{atm}}{\partial\eta} \quad \textbf{(18)}$$

and represent the barotropic pressure gradients. Atmospheric pressure is included for storm surge events (Deltares, 2011). If the density is assumed to be non-uniform, the baroclinic term of the pressure gradient must be taken into account and equations (17) and (18) become:

$$\frac{1}{\rho_0\sqrt{G_{\xi\xi}}}P_\xi = \frac{g}{\sqrt{G_{\xi\xi}}}\frac{\partial\zeta}{\partial\xi} + g\frac{d+\zeta}{\rho_0\sqrt{G_{\xi\xi}}}\int_\sigma^0\left(\frac{\partial\rho}{\partial\xi} + \frac{\partial\rho}{\partial\sigma}\frac{\partial\sigma}{\partial\xi}\right)d\sigma' \quad \textbf{(19)}$$

and

$$\frac{1}{\rho_0\sqrt{G_{\eta\eta}}}P_\eta = \frac{g}{\sqrt{G_{\eta\eta}}}\frac{\partial\zeta}{\partial\eta} + g\frac{d+\zeta}{\rho_0\sqrt{G_{\eta\eta}}}\int_\sigma^0\left(\frac{\partial\rho}{\partial\eta} + \frac{\partial\rho}{\partial\sigma}\frac{\partial\sigma}{\partial\eta}\right)d\sigma' \quad \textbf{(20)}$$

where the first two terms on the right are due to barotropic forcing, while the third term represents the baroclinic component due to non-uniform density (Deltares, 2011).

Transport equation

The transport of dissolved substances, heat or salinity in Delft3D-flow is expressed by a three-dimensional advection-diffusion equation. In a conservative form, with σ co-ordinates in the vertical and orthogonal curvilinear co-ordinates in the horizontal direction, the transport equation can be expressed by:

$$\begin{aligned}\frac{\partial(d+\zeta)c}{\partial t} + \frac{1}{\sqrt{G_{\xi\xi}}\sqrt{G_{\eta\eta}}}\left\{\frac{\partial[\sqrt{G_{\eta\eta}}(d+\zeta)uc}{\partial\xi} + \frac{\partial[\sqrt{G_{\xi\xi}}(d+\zeta)vc}{\partial\eta}\right\} + \frac{\partial\omega c}{\partial\sigma} \\ = \frac{d+\zeta}{\sqrt{G_{\xi\xi}}\sqrt{G_{\eta\eta}}}\left\{\frac{\partial}{\partial\xi}\left(D_H\frac{\sqrt{G_{\eta\eta}}}{\sqrt{G_{\xi\xi}}}\frac{\partial c}{\partial\xi}\right) + \frac{\partial}{\partial\eta}\left(D_H\frac{\sqrt{G_{\xi\xi}}}{\sqrt{G_{\eta\eta}}}\frac{\partial c}{\partial\eta}\right)\right\} \\ + \frac{1}{d+\zeta}\frac{\partial}{\partial\sigma}\left(D_v\frac{\partial c}{\partial\sigma}\right) - \lambda_d(d+\zeta)c + S\end{aligned} \quad \textbf{(21)}$$

where D_v and D_H are the vertical and horizontal diffusion coefficients, respectively, λ_d is a first-order decay process and *S* represents the sources and sinks due to exchange of heat at the free surface and discharge and withdrawal of water (Deltares, 2011).

Boundary Conditions

The boundary conditions describe the influence of the outer world on the model area. This chapter will explain the flow boundary condition as well as the transport boundary conditions.

Flow boundary conditions

Concerning vertical flow boundary conditions, the water surface and bottom are assumed to be impermeable, not allowing any flow:

$$w|_{\sigma=-1} = 0 \; and \; w|_{\sigma=0} = 0 \quad \textbf{(22)}$$

The boundary conditions for the momentum equations at the sea bed in the ξ and η directions are defined by:

$$\frac{v_v}{H}\frac{\partial u}{\partial \sigma}|_{\sigma=-1} = \frac{1}{\rho_0}\tau_{b\xi} \quad \textbf{(23)}$$

and

$$\frac{v_v}{H}\frac{\partial v}{\partial \sigma}|_{\sigma=-1} = \frac{1}{\rho_0}\tau_{b\eta} \quad \textbf{(24)}$$

where $\tau_{b\xi}$ and $\tau_{b\eta}$ represent the horizontal bed stresses (Deltares, 2011).

In a three-dimensional model, the bed shear stress, related to the current just above the bed, is given by:

$$\vec{\tau}_{b3D} = \frac{g\rho_0 \vec{u}_b|\vec{u}_b|}{C_{3D}^2} \quad \textbf{(25)}$$

where $|\vec{u}_b|$ is the horizontal velocity in the bottom layer and C_{3D} is the three-dimensional Chézy coefficient, given by

$$C_{3D} = \frac{\sqrt{g}}{k}\ln\left(1 + \frac{\Delta z_b}{2z_0}\right) \quad \textbf{(26)}$$

with z_0 being the roughness height of the bed and *k* being the turbulent kinetic energy.

At the free surface, the momentum equations are characterised by the boundary conditions

$$\frac{v_v}{H}\frac{\partial u}{\partial \sigma}|_{\sigma=0} = \frac{1}{\rho_0}|_{\vec{\tau}_s}|\cos(\theta) \quad \textbf{(27)}$$

and

$$\frac{v_v}{H}\frac{\partial v}{\partial \sigma}|_{\sigma=0} = \frac{1}{\rho_0}|_{\vec{\tau}_s}|\sin(\theta) \quad \textbf{(28)}$$

where θ is the angle of the wind stress and $\vec{\tau}_s$ is its magnitude, defined by the quadratic expression

$$|\vec{\tau}_s| = \rho_a C_d U_{10}^2 \quad \textbf{(29)}$$

with ρ_a representing the density of air, C_d being the wind drag coefficient and U_{10} representing the wind velocity at 10 m above the free surface. For wind drag depending on wind velocity, e.g. due to increased surface roughness due to wave development with stronger winds, a wind drag coefficient varying with wind speed may be defined (Deltares, 2011).

The open boundary is the zone where the model is connect to the open ocean or freshwater areas such as rivers. Here, boundary conditions can be defined from river discharge data, tidal data, a larger model in which the current model can be “nested”, or measured water level data. The boundary conditions are defined at a number of points and linearly interpolated to cover the complete open boundary.

Depending on data availability and flow conditions, a choice can be made between a number of boundary conditions:

- Water level;
- Velocity;

- Discharge;
- Neumann (water level gradient);
- Riemann invariant.

The **water level** boundary condition is described by

$$\zeta = F_{\zeta}(t) + \delta_{atm} \quad \textbf{(30)}$$

and can describe e.g. tidal oscillations of the water level.

The **velocity** boundary condition in the normal direction is defined by

$$U = F_U(t) \quad \textbf{(31)}$$

The **discharge** boundary condition is defined as

$$Q = F_Q(t) \quad \textbf{(32)}$$

The **Neumann** boundary condition can only be applied to cross-shore boundaries in combination with a water level boundary at the sea-ward boundary and imposes the along-shore water level gradient:

$$\frac{\partial \zeta}{\partial \vec{n}} = f(t) \quad \textbf{(33)}$$

The **Riemann** boundary condition simulates a weakly reflective boundary, meaning that outgoing waves are not reflected back into the model area at the open boundary. In the Riemann boundary condition, the zero order boundary condition assuming no flow along the boundary can be obtained through the "Riemann invariants":

$$R = U \pm 2\sqrt{gH} \quad \textbf{(34)}$$

in which the Riemann invariants are two waves propagating with velocities $R = U \pm \sqrt{gH}$ in opposite directions. At the offshore boundary, the linearized Riemann invariant is then:

$$U + 2\sqrt{gH} = U + 2\sqrt{g(d+\zeta)} \approx U + 2\sqrt{gd} + \zeta\sqrt{\frac{g}{d}} \qquad \frac{|\zeta|}{d} \ll 1 \quad \textbf{(35)}$$

In the water level and velocity boundary conditions, a weakly reflective boundary condition such as in the Riemann condition can be obtained by defining the α reflection coefficient (Deltares, 2011).

Applying α, the time-derivative of the Riemann invariant can be added to the water level boundary condition to make the boundary less reflective for disturbances with the eigen frequency of the model domain:

$$\zeta + \alpha \frac{\alpha}{\alpha t}\{U \pm 2\sqrt{gH}\} = F_{\zeta}(t) \quad \textbf{(36)}$$

Different forcing types are available:

- Astronomic using tidal constituents
- Harmonic through defined frequencies, amplitudes and phases

- QH-relation describing the water level from computational discharge leaving the domain through the boundary (only for water level boundaries)
- Time-series

At closed boundaries between land and water, the flow normal to the boundary has to be zero, as the boundary is impermeable. Shear stress along the boundary is usually assumed to be zero tangential shear-stress (free slip), unless very small-scale flows are simulated, such as laboratory scale, in which case a partial slip condition is used at the closed boundaries (Deltares, 2011).

Transport boundary conditions

The horizontal transport processes in environments such as estuaries and coastal seas is dominated by advection, with horizontal diffusion terms being less important. At an open boundary, during inflow, a boundary condition is needed to describe this advective transport. During the outflow, however, the concentration must be free. The concentration transported into the model area through the open boundary may also be influenced by the concentration that left the model area during previous outflows. To make up for this effect, a boundary condition taking into account both, the concentration in the modelling area and a return time (the time it takes before the concentration along the boundary reaches the maximum concentration value prescribed outside the model area) is used, the so-called Harleman-Thatcher boundary condition (Deltares, 2011). The return time depends on the renovation of the water at the open boundary.

Vertical transport conditions along the boundary can be specified in four ways: as a uniform profile, as a linear profile interpolated between surface- and bottom layer, as a step profile from surface- and bottom layer and the location of a discontinuity, or a three-dimensional profile from a nested model.

The concentration as defined by advection from the interior area can be defined as

$$\frac{\partial C}{\partial t} + \frac{U}{\sqrt{G_{\xi\xi}}}\frac{\partial C}{\partial \xi} = 0 \qquad \textbf{(37)}$$

The so-called memory-effect of transition time taken after slack water until the concentrations at the boundary reach those defined as boundary condition can be defined by

$$C(t) = C_{out} + \frac{1}{2}(C_{bnd} - C_{out})\left(\cos\left(\pi\frac{T_{ret} - t_{out}}{T_{ret}}\right) + 1\right), \qquad 0 \le t_{out} \le T_{ret} \qquad \textbf{(38)}$$

where C_{out} and C_{bnd} are the computed concentration at the open boundary at the last time of outward flow and the background concentrations, respectively and t_{out} and T_{ret} are the time passed since the last outflow and the constituent return period, respectively. While t_{out} is positive but smaller than the constituent return period, the concentration will return to the background concentration. Once t_{out} has reached the constituent return period, the concentration will remain at the level of the background concentration (Deltares, 2011).

Vertical transport at the free surface and seabed boundaries is usually zero. An exception is the transport of heat, which can be transferred through the sea surface, described by:

$$\frac{D_v}{H}\frac{\partial c}{\partial \sigma}|_{\sigma=0} = 0 \quad \textbf{(39)}$$

and

$$\frac{D_v}{H}\frac{\partial c}{\partial \sigma}|_{\sigma=-1} = 0 \quad \textbf{(40)}$$

Turbulence

Turbulent processes in Delft3D-flow usually occur "sub-grid", meaning that the spatial grid and temporal scales of the model are too coarse to resolve turbulent motion. Closure assumptions are needed to filter the equations when using space- and time averaged quantities.

In shallow water, as assumed in Delft3D-flow, the horizontal eddy viscosity coefficient and eddy diffusivity coefficient are much larger than the vertical coefficients. They consist of three factors: one due to molecular viscosity, one due to two-dimensional turbulence associated with the contribution of horizontal motions and forces on a sub-grid scale and one due to three-dimensional turbulence computed following a turbulence closure model (Deltares, 2011).

Delft3D-flow offers a choice of four turbulence closure models:

1. Constant coefficient
2. Algebraic Eddy viscosity closure Model (AEM)
3. K-L turbulence closure model
4. K-ε turbulence closure model

While the first model is very simple and based only on a constant value defined by the modeller, the latter three models are based on the eddy-viscosity concepts of Kolmogorov (1942) and Prandtl (1945) which has the form

$$v_{3d} = c'_{\mu} L\sqrt{k} \quad \textbf{(41)}$$

Where *L* is the mixing constant, k is the turbulent kinetic energy and c'_{μ} is a constant c'_{μ} = 0.09

In this context, only the k-ε turbulence closure model will be explained in more detail.

The *k-ε* model is a second-order turbulence closure model in which the turbulent kinetic energy *k* and the dissipation rate of turbulent kinetic energy *ε* are calculated by a transport equation. The mixing length *L*, calculated from *ε* and *k*, can become a property of the flow, making damping functions unnecessary:

$$L = C_D \frac{k\sqrt{k}}{\varepsilon} \quad \textbf{(42)}$$

The transport equations for k and ε, assuming that horizontal length scales are larger than vertical length scales and that production, buoyancy and dissipation are the dominating terms, becomes:

$$\frac{\partial k}{\partial t}+\frac{u}{\sqrt{G_{\xi\xi}}}\frac{\partial k}{\partial \xi}+\frac{v}{\sqrt{G_{\eta\eta}}}\frac{\partial k}{\partial \eta}+\frac{w}{d+\zeta}\frac{\partial k}{\partial \sigma} = \frac{1}{(d+\zeta)^2}\frac{\partial}{\partial \sigma}\left(D_k\frac{\partial k}{\partial \sigma}\right)+P_k+P_{kw}+B_k-\varepsilon \quad (43)$$

and

$$\frac{\partial \varepsilon}{\partial t}+\frac{u}{\sqrt{G_{\xi\xi}}}\frac{\partial \varepsilon}{\partial \xi}+\frac{v}{\sqrt{G_{\eta\eta}}}\frac{\partial \varepsilon}{\partial \eta}+\frac{w}{d+\zeta}\frac{\partial \varepsilon}{\partial \sigma} = \frac{1}{(d+\zeta)^2}\frac{\partial}{\partial \sigma}\left(D_\varepsilon\frac{\partial \varepsilon}{\partial \sigma}\right)+P_\varepsilon+P_{\varepsilon w}+B_\varepsilon-c_{2_\varepsilon}\frac{\varepsilon^2}{k} \quad (44)$$

where

$D_k = \frac{v_{mol}}{\sigma_{mol}}+\frac{v_{3d}}{\sigma_k}$ and $D_\varepsilon = \frac{v_{3D}}{\sigma_\varepsilon}$,

$P_k = v_{3D}\frac{1}{(d+\zeta)^2}\left[\left(\frac{\partial u}{\partial \sigma}\right)^2+\left(\frac{\partial v}{\partial \sigma}\right)^2\right]$,

$B_k = \frac{v_{3D}}{\rho\sigma_\rho}\frac{g}{H}\frac{\partial \rho}{\partial \sigma}$,

$P_\varepsilon = c_{1\varepsilon}\frac{\varepsilon}{k}P_k$,

$B_\varepsilon = c_{1\varepsilon}\frac{\varepsilon}{k}(1-c_{3\varepsilon})B_k$ and

The calibration constants are:

$c_{1\varepsilon}$ = 1.44

$c_{2\varepsilon}$ = 1.92

$c_{3\varepsilon}$ = 0.0 for unstable stratification; 1.0 for stable stratification

(Deltares, 2011).

3.2 Model Calibration and Validation

Hydrodynamic models can be used to reproduce real phenomena occurring in environments such as estuaries. Before such a model can be used, it must first be calibrated to test how well it represents reality. For this calibration, short time series of measured data are compared with modelled data for the same time series and location (Cheng et al., 1993). Various factors, such as sea surface elevations, velocities, water temperatures and salinities can be compared this way. A number of model parameters can be adjusted to improve the model's performance in reconstructing reality.

In the model validation, the accuracy of the model predictions can be tested, using data sets independent of those used in the model calibration (Dias et al., 2009).

Model Establishment and Hydrodynamic Model Calibration

The model applied to Maputo Bay is based on a model published by Lencart e Silva et al. (2010). Those authors applied a curvilinear grid with 96x135 cells to Maputo Bay in Delft3D-flow. This irregular grid has a mean resolution of approximately 500 m, with higher resolution within parts of the embayment and lower resolution outside the bay. The bathymetry data is composed of the results of a number of surveys undertaken between the 1960s and the 1980s. More recent bathymetric data is not available. Atmospheric input data was obtained from an observation station located at Mavalene Airport. Five equally-spaced vertical cells were used, applying sigma layers. Lencart e Silva et al. (2010) calibrated the model and increased the Nikuradse parameter from an initial Nikuradse length of k_s=3x10^{-2} to 10^{-1} m to increase bottom roughness and prevent the underestimation of frictional dissipation, which occurred previously. The propagation of the tide is modelled by prescribing tidal harmonics, interpolated across the open boundary, and vertical mixing is determined by a k-ε closure scheme. A heat model is applied, taking into account air temperature, wind speed at a meteorological station at Mavalene Airport, atmospheric radiation, relative humidity as well as net solar and atmospheric radiation to calculate heat losses from convection, evaporation and back radiation. Wind data obtained from a station at Mavalene Airport is applied at the water surface. Salinities and water temperatures, obtained from data from Sete et al. (2002) who developed a compilation of the available cruise data between 1977 and 1980, are defined for each of the vertical layers at the open oceanic boundary, divided into 14 horizontal sections. Salt transport is calculated based on inputs from freshwater of the rivers and salinities prescribed at the oceanic open boundary.

Lencart e Silva et al. (2010) concluded that the model represented tidal motion and dissipation. Furthermore was the model able to satisfactorily reproduce the tidal and subtidal features during the dry season. However, during the wet season spring tides, vertical mixing was overestimated, possibly as a consequence of the insufficient vertical resolution as well as the increased bottom roughness. This also lead to an overestimation of flushing times and the salinity deficit in the bay due to artificial freshwater storage. In turn, the horizontal density gradient was exaggerated, increasing neap tide estuarine circulation. This study uses the model published by Lencart e Silva et al. (2010) as a basis, improving its ability to represent the wet season dynamics. Figure 4 shows the grid as well as the location stations of the several observation stations that were used for model calibration as well as for the production of results.

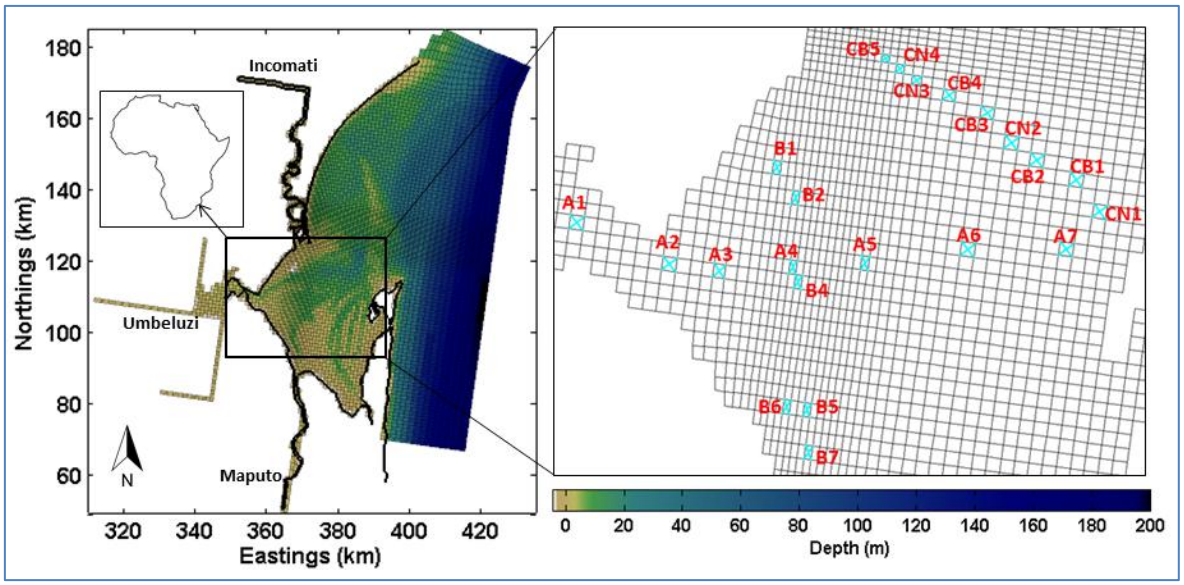

Figure 4: Bathymetry and grid of Maputo Bay. Blue circles indicate locations of observation stations used for the calibration. Stations with the index CB and CN were used to create results over the cross section of the bay's opening.

The original horizontal grid was maintained, increasing vertical resolution from five equally spaced sigma layers to 15 sigma layers, with refined surface layers, to improve the model's ability to resolve mixing. The surface layers were refined compared to intermediate and bottom layers due to the most important dynamics related to the freshwater plumes occurring in the surface layers. The percentages of depth of each layer are given in Table 1.

Table 2: Percentage of Depth per Layer, with Layer 1 Representing The Surface Layer and Layer 15 Representing the Bottom Layer

Layer	1	2	3	4	5	6	7	8	9	10	11	12	13	14	15
Percentage of Depth	2	3	4	5	6	8	8	8	8	8	8	8	8	8	8

The bottom roughness applied in the previous model was maintained.
The modeling time step was refined from 5 minutes to 1 minute to be in a accordance with the Courant-Friedrichs-Lewy number (CFL).

The CFL number of wave propagation is given by

$$CFL_{wave} = 2\Delta t\sqrt{gH}\sqrt{\frac{1}{\Delta x^2}+\frac{1}{\Delta y^2}} < 1 \qquad (45)$$

where t is the time step, g is gravity, H is the depth of the water column and $\Delta x = \sqrt{G_{\xi\xi}}$ and $\Delta y = \sqrt{G_{\eta\eta}}$ are the smallest grid spaces in the ξ- and η-direction, respectively (Deltares, 2011).

If the time step of a model is is too large in relation to grid cell size and water depth, instabilities can develop from the tidal wave propagations. Decreasing the time step lead to a change in CFL. The maximum values decreased from 55 to 11 in the shelf region and from 16 to 3.5 within the bay, with values now being in the range recommended by Deltares (2011).

Background horizontal eddy viscosity and diffusivity were changed from 10 to 1 m^2s^{-1}. Background vertical eddy viscosity and diffusivity were not integrated in the original model and are 10^{-4} m^2s^{-1} in the new model. Including background horizontal eddy viscosity can help dampen out short oscillations developing in the model, which appeared in other calibration runs without background horizontal eddy viscosity.

Several model runs were performed to calibrate the numerical model, in order to reduce the differences between the available observational data and modelled predictions.

The calibration runs were set up from a cold start, including wind forcing, river flow from the rivers Incomati, Maputo, Umbeluzi, Tembe and Matola, a heat flux model as well as open-boundary forcing with tidal harmonic water levels, salinities and water temperatures. Model predictions were compared against observations, consisting of CTD profiles from Lencart e Silva (2007). The CTD profiles were taken in 18 stations within Maputo Bay, with 14 surveys taken for each station, spread over wet and dry season in 2003/04.

As a first step, the model's ability to represent the propagation of the tide inside the model domain was evaluated. Due to the limited amount of observational data available over an extended period of time, only two stations were chosen for this evaluation. Water levels were compared with tide gauge data for the station Clube Naval, located at the harbour of Maputo City. Current velocities were compared with moorings containing bottom and surface current meters located at station CB2 (see Figure 4). Both data sets were collected in the framework of the Lencart e Silva (2007) PhD Thesis and have a duration of approximately 4 months.

Following the methodology proposed by Dias and Lopes (2006) at first a visual comparison of observed and predicted water levels was performed. For this, the data set for the station Clube Naval was compared with modelled sea surface elevations for the same locations, the results of which can be seen in Figure 5.

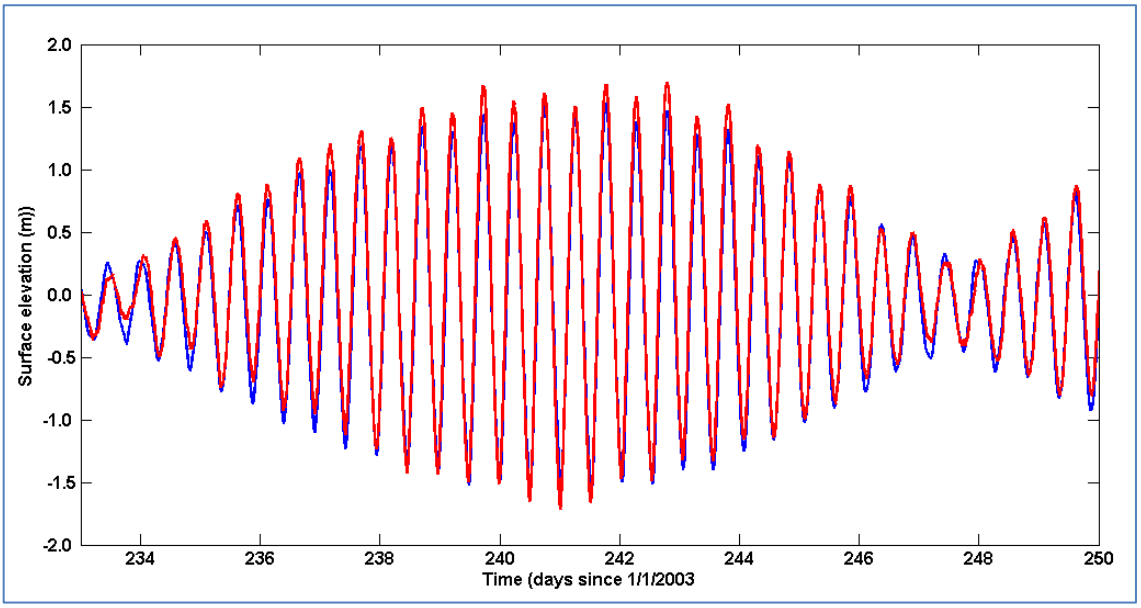

Figure 5: Comparison between observations and model results of SSE time series. Observations shown in red, model results shown in blue.

The visual comparison shows that the model represents very well the sea surface elevations over the spring-neap cycle. Next, a visual comparison of surface and bottom currents at station CB2 was undertaken, separated into *u*- and *v* components of the current, shown in Figure 6.

The surface *u*-component velocities predicted by the model are very close to the observed velocities (Figure 6a). Surface *v* velocities are overestimated by the model, but still do represent the semidiurnal and spring-neap cycles (Figure 6b). Bottom velocities are slightly underestimated by the model but still show an acceptable fit.

After the visual comparison, the model performance was quantified by two error parameters: the Root Mean Square Error (RMSE) and the Skill parameter.

Stow et al. (2003) formulated the RMSE as:

$$RMSE = \sqrt{\frac{\sum_{i=1}^{N}[\zeta_o(t_i) - \zeta_m(t_i)]^2}{N}} \quad \textbf{(46)}$$

where $\zeta_o(t_i)$ is the observed sea surface elevation at time t_i, $\zeta_m(t_i)$ is the modelled sea surface elevation at time t_i and N is the number of observations.

The RMSE is a measure of the discrepancies between predictions and observations, considering magnitude rather than direction (Stow et al., 2007). A value close to zero indicates a good model performance. Dias et al. (2009) suggested that an RMSE lower than 5% of the local amplitude represents an excellent agreement between model and observations, while an RMSE between 5% and 10% indicates a very good agreement.

The model predictive skill is a method developed by Willmott (1981) and has previously been applied in several studies (e.g. Warner et al., 2005 and Li et al., 2005).

The skill parameter is formulated as:

$$Skill = 1 - \frac{\sum|\zeta_m - \zeta_o|^2}{\sum[|\zeta_m - \bar{\zeta}_o| + |\zeta_o - \bar{\zeta}_o|]^2} \quad \textbf{(47)}$$

where $\bar{\zeta}_o$ is the time average of observed sea surface elevations over the research period.

A skill of one means a perfect representation of observations by the model. Dias et al. (2009) suggested that sea surface elevation skills higher than 0.95 can be considered excellent. Values for RMSE and skill can be found in Table 3. For water levels, the RMSE is approximately 10% of the local mean amplitude of the tide and therefore represents a very good performance of the model. The Skill value shows an excellent performance.

Table 3: Error values for tidal water levels and currents

Parameter	RMSE	Skill
Water Level	0.101	0.995
Surface Velocities in *u*-direction	0.173	0.968
Surface Velocities in *v*-direction	0.174	0.920
Bottom Velocities in *u*-direction	0.150	0.949
Bottom Velocities in *v*-direction	0.083	0.969

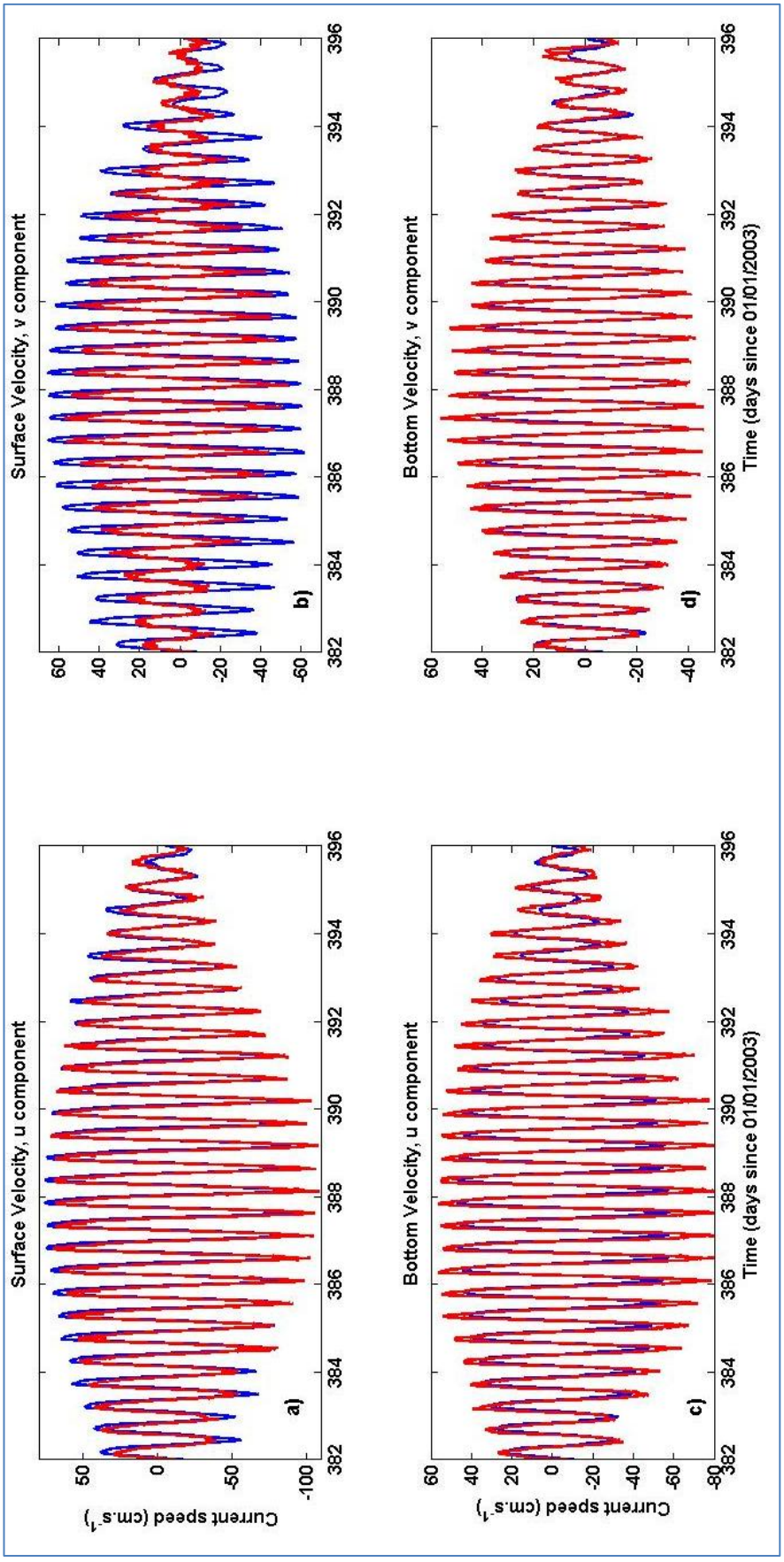

Figure 6: Comparison between observations and model predictions of tidal currentsfor a) surface velocities of the *u*-component, b) surface velocities for the *v*-component, c) bottom velocities for the *u*-component and d) bottom velocities for the *v*-component. Observations shown in red, model results shown in blue.

The model's ability in predicting the tidal velocities is slightly smaller, indicated by the smaller skill values. Surface velocities of the *u*-component and bottom velocities of the *v*-component show a better representation by the model, while surface velocities in the *v* direction are represented less accurately. Generally, however, the model predicts the velocities and water levels to a satisfactory level.

In the next step, a comparison between observed and predicted tidal amplitudes and phases of the mean tidal constituents was conducted. The analysis focused on the two diurnal constituents O_1 and K_1, the semidiurnal constituents M_2, S_2 and N_2 as well as the shallow water constituents M_4 and M_6 and was performed using the software package developed by Pawlowicz et al. (2002).

Figure 7 shows a comparison of water level amplitudes and Figure 8 shows a comparison of phases.

For a table containing a more extensive number of constituents, please refer to Appendix A. Generally, the model represents the tidal amplitudes well, especially for the most important semidiurnal constituents M_2 and S_2. The diurnal constituent O_1 also shows a good agreement between observations and predictions. K_1, on the other hand, is underestimated by the model by approximately 1 cm, corresponding to 20% of the amplitude of that constituent. The shallow water constituents show very different performances: While the M_6 overtide shows a very close agreement between observation and model, M_4 is overestimated by approximately 1 cm. These errors in the shallow water constituent may be due to the bathymetries, either caused by an insufficiently fine horizontal resolution of the model grid or due to the fact that the bathymetry of the model is based on data several decades old, possibly not accurate any more.

The phase lags are generally represented well by the model. Discrepancies are larger for the shallow-water constituents M_4 and M_6. The largest phase difference is 30° for the M_4 overtide. The model predicts the arrival of this constituent approximately half an hour too late.

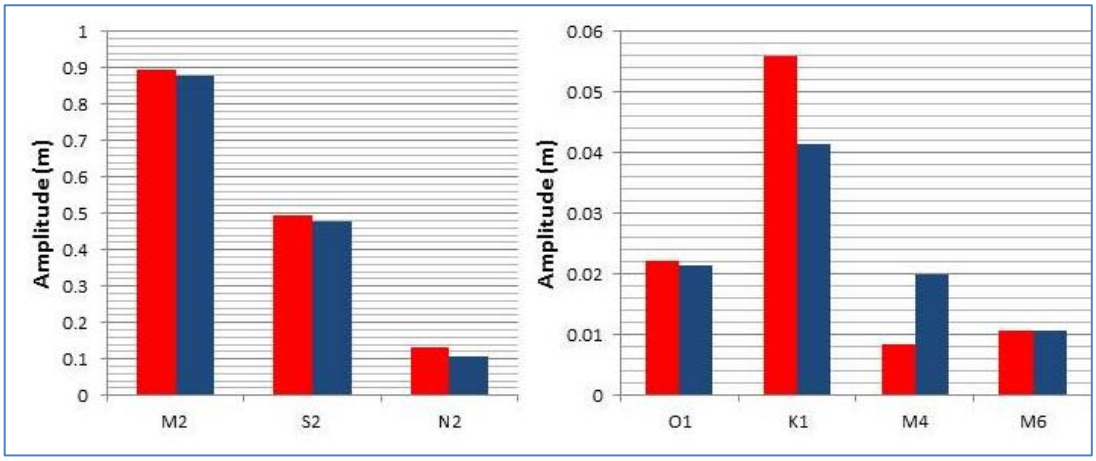

Figure 7: Comparison between predicted and observed tidal amplitudes for several constituents: for the semi-diurnal constituents M_2, S_2 and N_2, the diurnal constituents O_1 and K_1 and for the shallow water constituents M_4 and M_6. The red and blue bars represent the observed and predicted values, respectively.

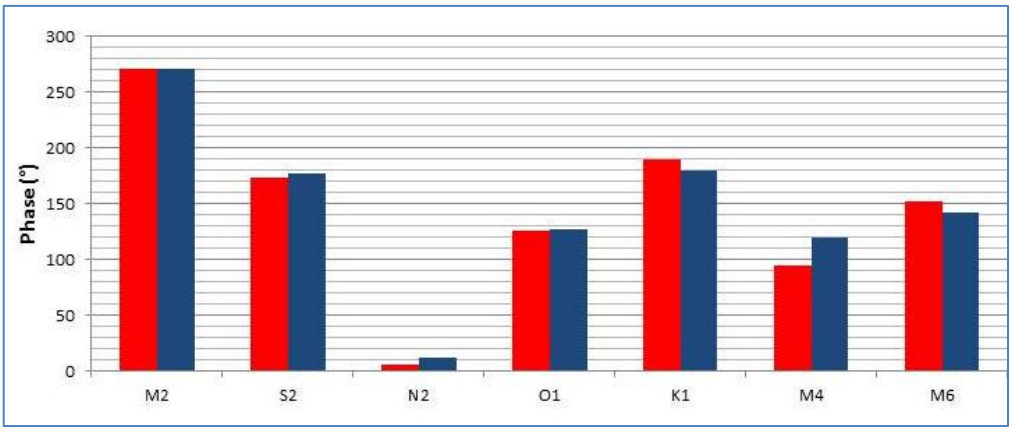

Figure 8: Comparison between predicted and observed phases for several constituents: the semi-diurnal constituents M_2, S_2 and N_2, the diurnal constituents O_1 and K_1 and for the shallow water constituents M_4 and M_6. The red and blue bars represent the observed and predicted values, respectively.

The visual analysis as well as the error analysis based on RMSE and skill values have shown that the model represents well the tidal water levels and current velocities. The harmonic analysis has shown that the tidal constituents with the largest amplitudes are represented well, while the model underestimated the diurnal constituent K_1. The shallow water constituent M_4 was overestimated. Shortcomings in representing the shallow water constituents may be due to an insufficient horizontal grid resolution or out-dated bathymetric data. Generally, the model may be considered calibrated to reproduce tidal processes for the aim of this investigation.

Whether the model is able to represent satisfactorily the salinity and water temperature structures was tested in a number of ways. Observational data for the calibration was obtained from the CTD surveys undertaken by Lencart e Silva (2007) in Maputo Bay in 2003/04. A total of 11 surveys were used for the calibration, each of which was undertaken in 18 stations. All stations can be found in Figure 4. Please note that stations with the index “CN” were not used for calibration but only added to the model later for the production of results.

First, a bay-average comparison of salinities and water temperatures over several months was undertaken. This was done by interpolating the data obtained from the surveys over the bay area indicated by the mask in Figure 20 on page 50.

Figure 9b shows that the representation of temperatures by the model is good. Figure 9a, on the other hand, indicates that the model overestimates the salinity deficit in the wet season and freshens already before the arrival of the first freshwater pulse from the Incomati (Figure 9c), a problem that already was encountered in the previous model version. Lencart e Silva (2007) argues that this is possibly caused by overmixing of the model or due to the modelled river discharge for the Maputo River. For this river, no observations of discharge were available. The model was therefore forced with modelled discharge from the Maputo. It is possible that this modelled river discharge differs from the actual discharge over the research period, leading to differing salinities between observations and model predictions.

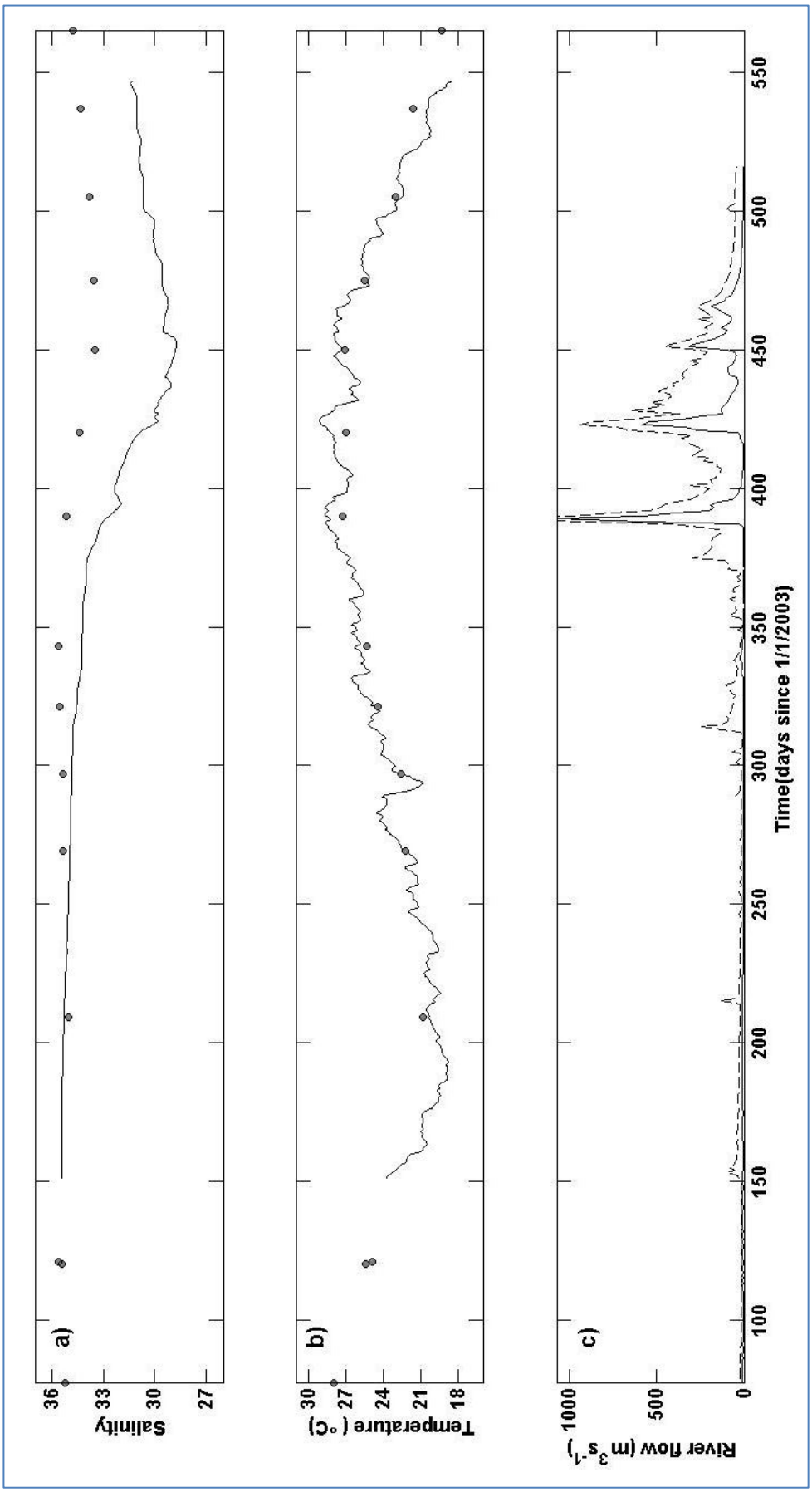

Figure 9: Comparison of predicted and observed seasonal evolution of bay-average salinity and water temperature with forcing agent river flow: a) bay average salinity (line: model results, dots: CTD observations from Lencart e Silva, 2007), b) bay average water temperature (line: model result, dots: CTD observations from Lencart e Silva, 2007, c) Incomati River flow from Magude River Gauge (solid line), input of flow for Delft3D model (dotted line) (reproduced with permission from Lencart e Silva, 2007).

Next, a more detailed analysis was undertaken to analyse the model's performance. Short time series of predicted and observed salinity, water temperature and the potential energy anomaly (φ) in one location at the bay's opening, station CB2 (see Figure 4 for location), were compared. For a description of φ please refer to page 51

The spring tide time series for the observations created by Lencart e Silva (2007) can be seen in Figure 10. A comparison with the predicted time series, Figure 11, shows that the general dynamics during spring tide are represented by the model. Figure 12 shows the results of the old model.

During spring tide, stratification in the observations was generally low, with values reaching a maximum of approximately 10 Jm^{-3}. While the old model (Figure 12a) underestimates the stratification during spring tide, showing maximum values of only 3 Jm^{-3}, the new model (Figure 11a) overestimates stratification at the station located 11.1 km south of station CB2, showing values of φ of around 17 Jm^{-3} . The stratification in station CB2 is underestimated. Observed salinities vary between 34.8 and 35.3. Minimum salinities are generally underestimated by both models, with the old model ranging between 34.1 and 35.2 and the new model ranging between 33.4 and 35.2. Water temperatures ranged between 26 and 28.5°C and were generally represented well by both models. Both models represented the mainly mixed conditions during spring tide, with very little stratification occurring during slack water.

For neap tide, observed time series produced by Lencart e Silva (2007) can be seen in Figure 13, predicted time series are shown in Figure 14 for the new model and in Figure 15 for the old model.

The observations during neap tide show very clear stratification in all three subplots. Maximum values of φ of around 70 Jm^{-3} are found and salinity shows a wide range, with surface salinities of 30 and bottom salinities of 34.5. The new model represents this strong stratification well and overestimates maximum values of φ, showing values of around 160 Jm^{-3} . The range in salinity is estimated well, with surface salinities of 30.5 and bottom salinities of 34.5. The old model, on the other hand, only produces φ values of up to 30 and a salinity ranging between 33.1 at the surface and 34.6 in the bottom. Observed water temperatures range between 27 and 29 and temperature ranges are underestimated by both models.

Concluding, the new model is able to represent the mixing-stirring dynamics occurring during wet season neap tide and spring tide. The overestimation of stratification during neap tide may be due to the larger amount of freshwater in the bay due to smaller predicted bay-average salinities. A cause for these may be the predicted data of Maputo river discharge that was used as an input in this model.

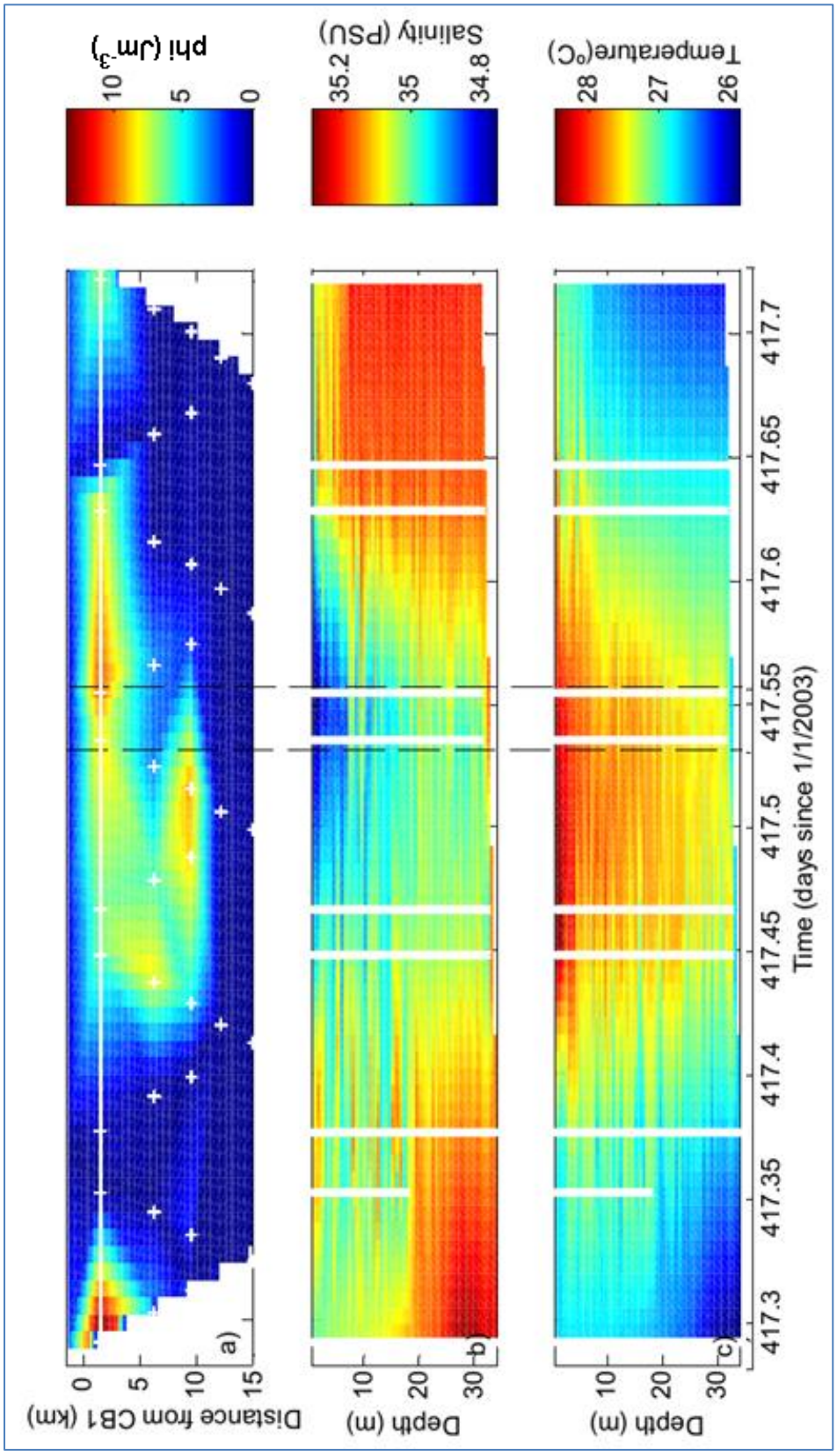

Figure 10: Observed water column properties at section CB during spring tide: a) variation of potential energy anomaly φ over section CB, b) salinity profile at station CB2, c) water temperature profile at station CB2. The dashed lines indicate time of low water slack. Reproduced with permission from Lencart e Silva (2007) .

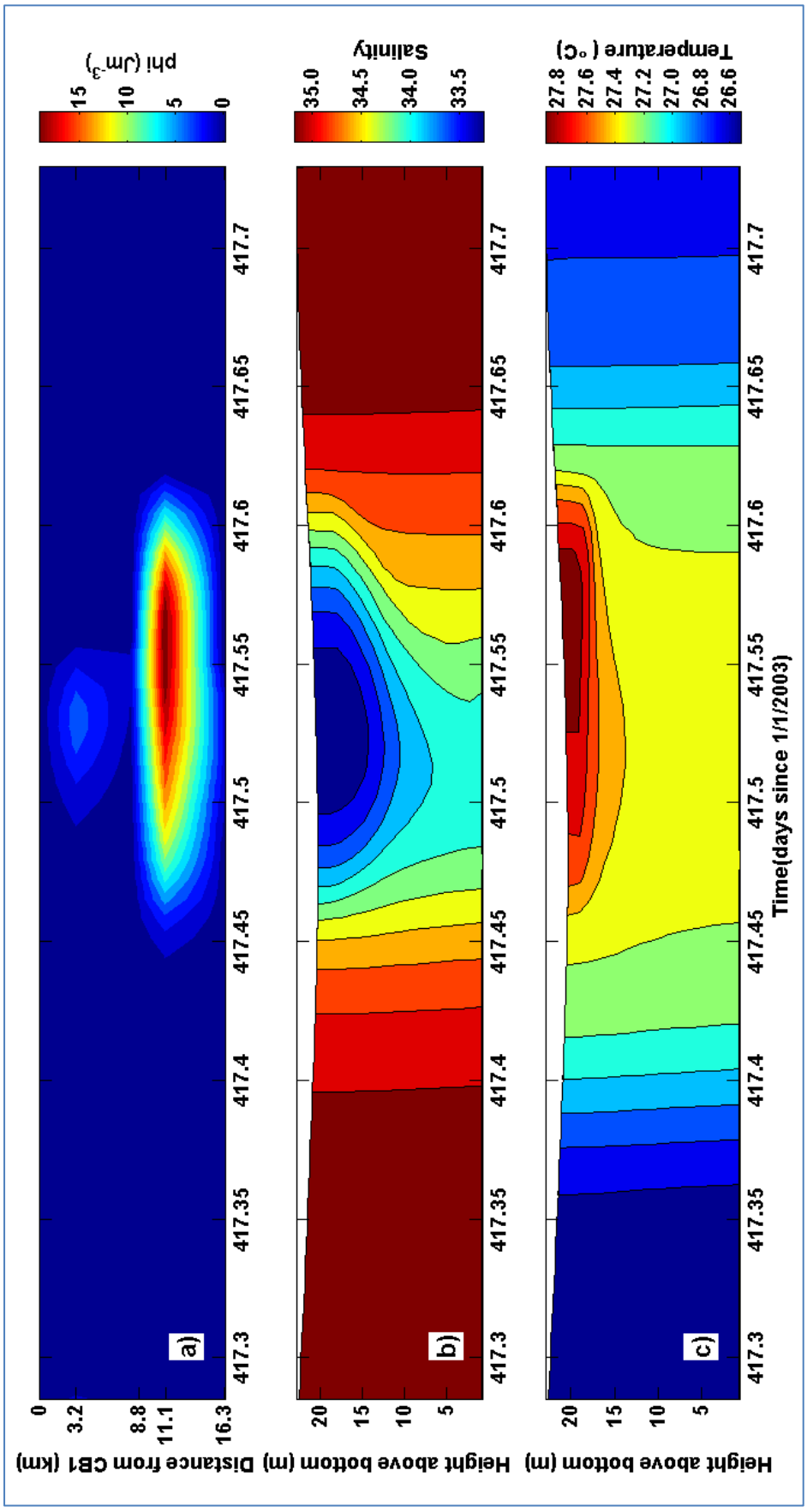

Figure 11: Predicted water column properties at section CB during spring tide for the new model: a) variation of potential energy anomaly φ over section CB, b) salinity profile at station CB2, c) water temperature profile at station CB2.

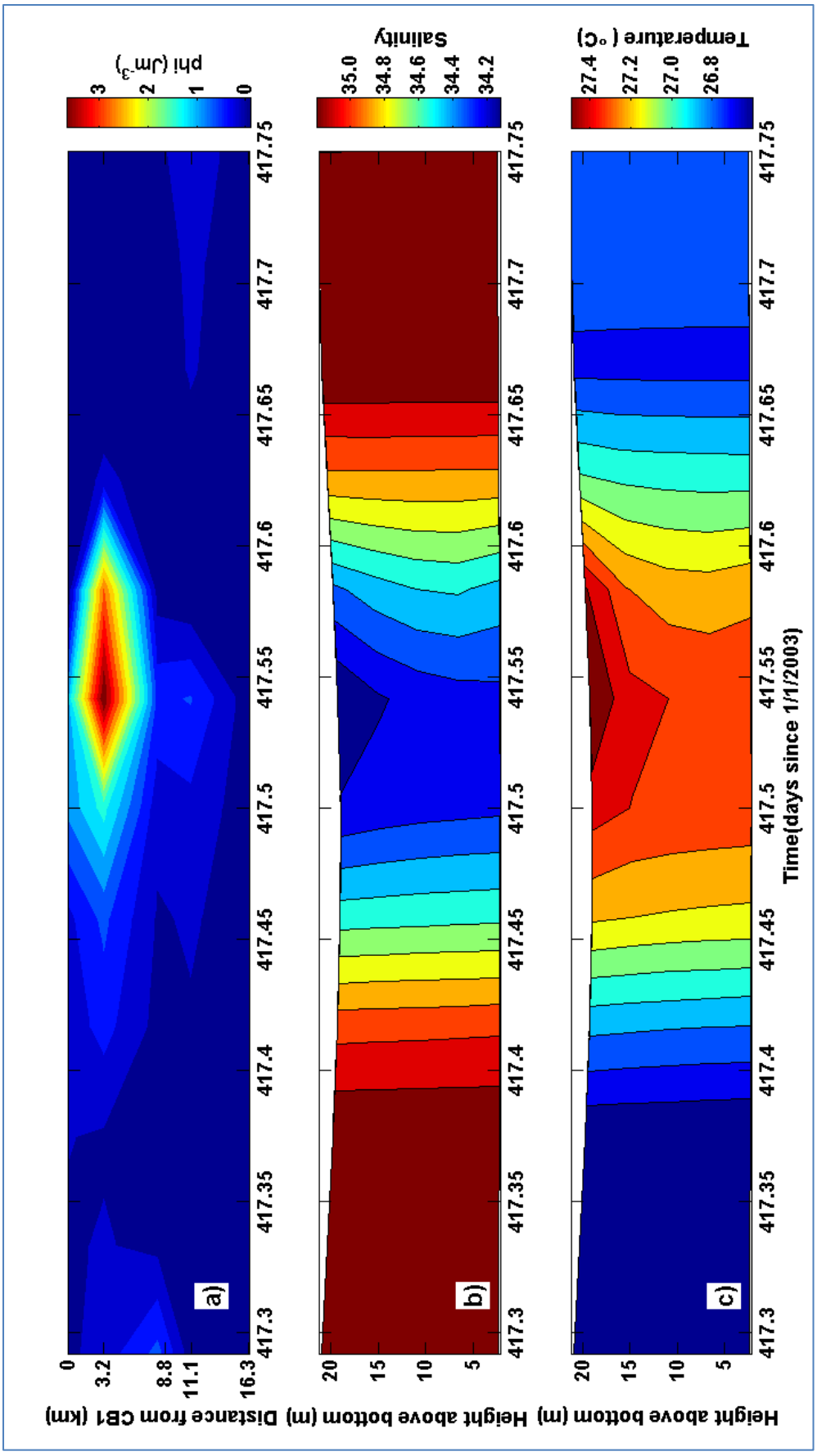

Figure 12: Predicted water column properties at section CB during spring tide for the old model: a) variation of potential energy anomaly φ over section CB, b) salinity profile at station CB2, c) water temperature profile at station CB2.

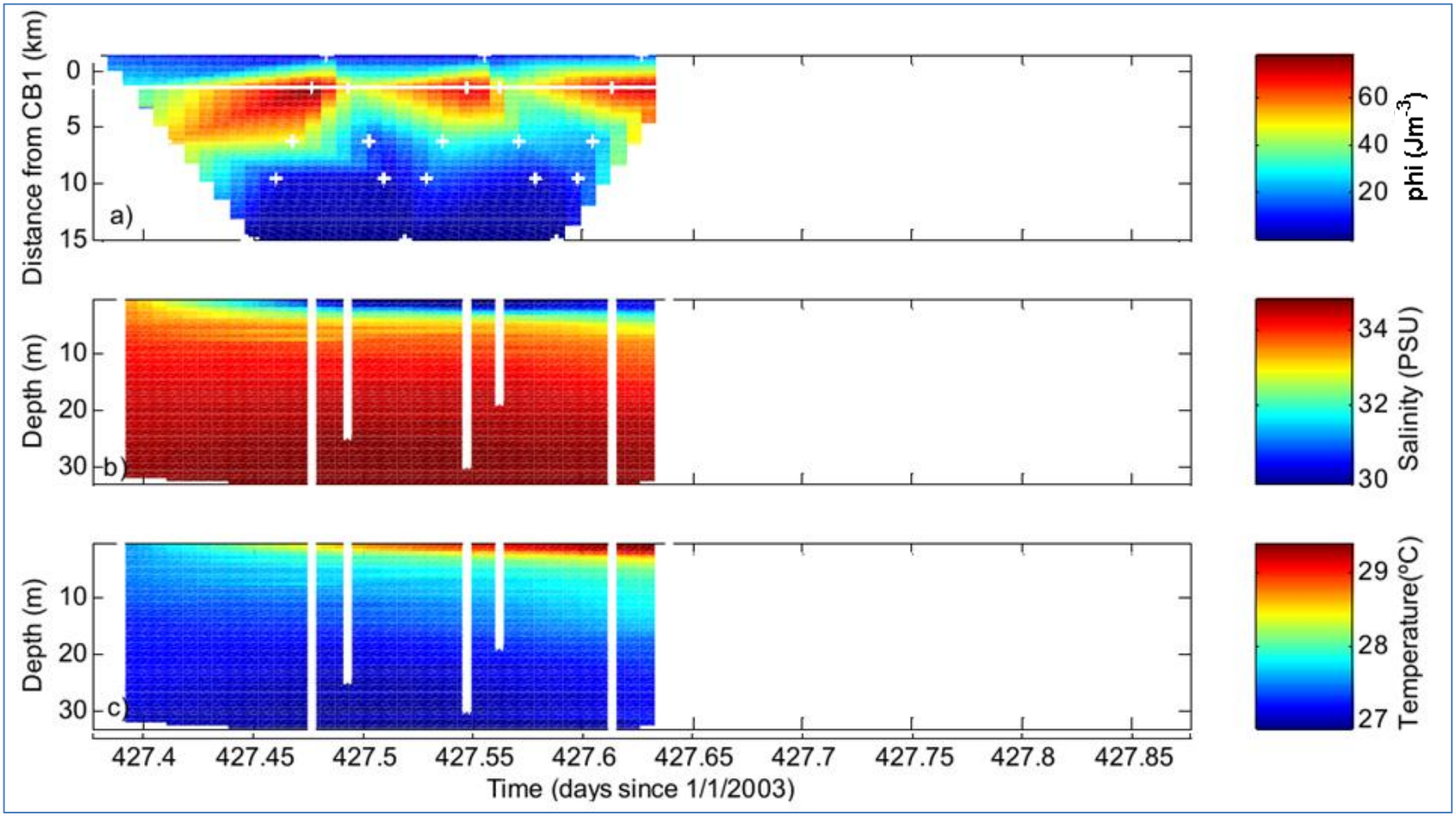

Figure 13: Observed water column properties at section CB during neap tide: a) variation of potential energy anomaly φ over section CB, b) salinity profile at station CB2, c) water temperature profile at station CB2. Reproduced with permission from Lencart e Silva (2007).

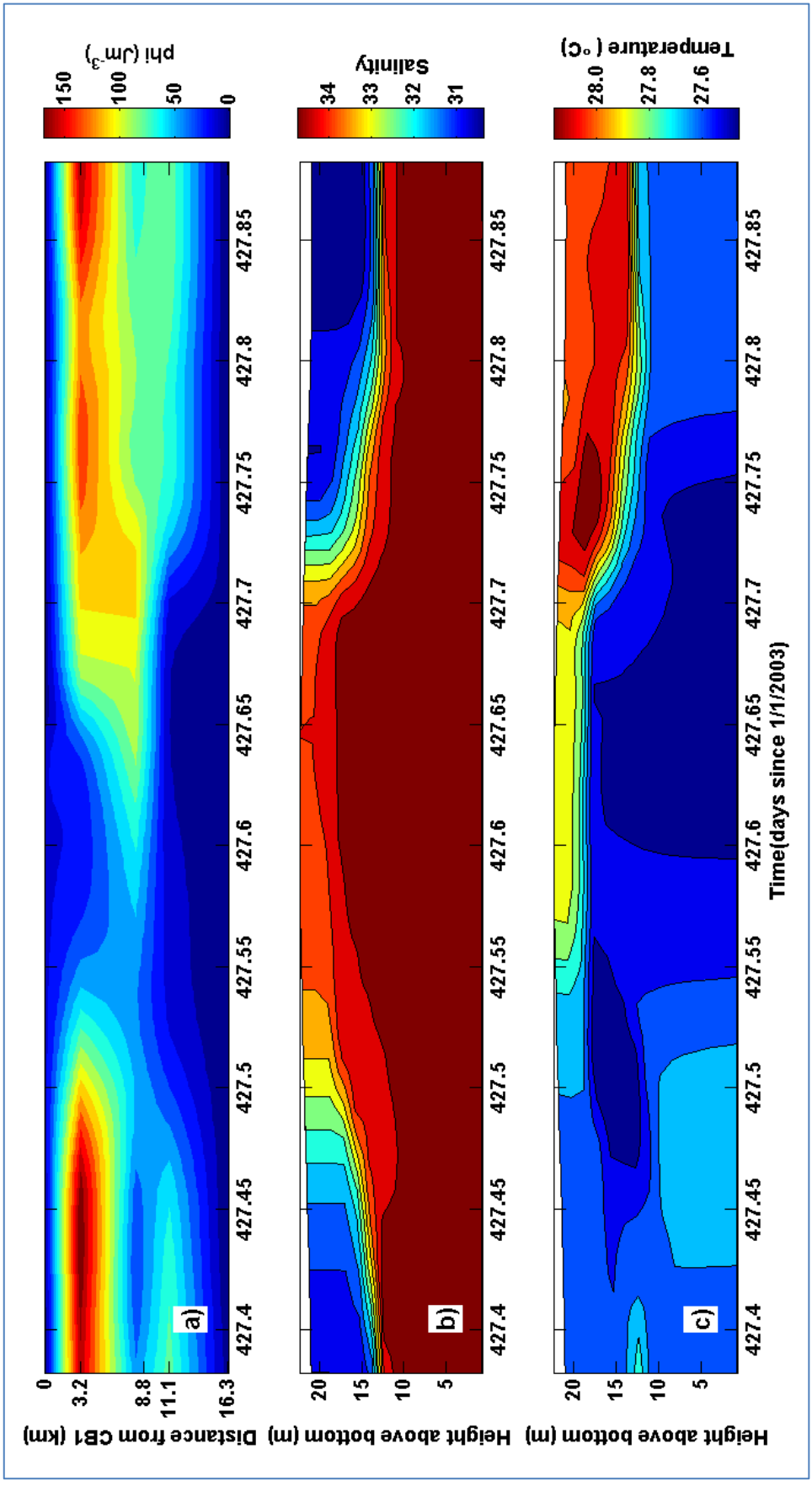

Figure 14: Predicted water column properties at section CB during neap tide for the new model: a) variation of potential energy anomaly φ over section CB, b) salinity profile at station CB2, c) water temperature profile at station CB2.

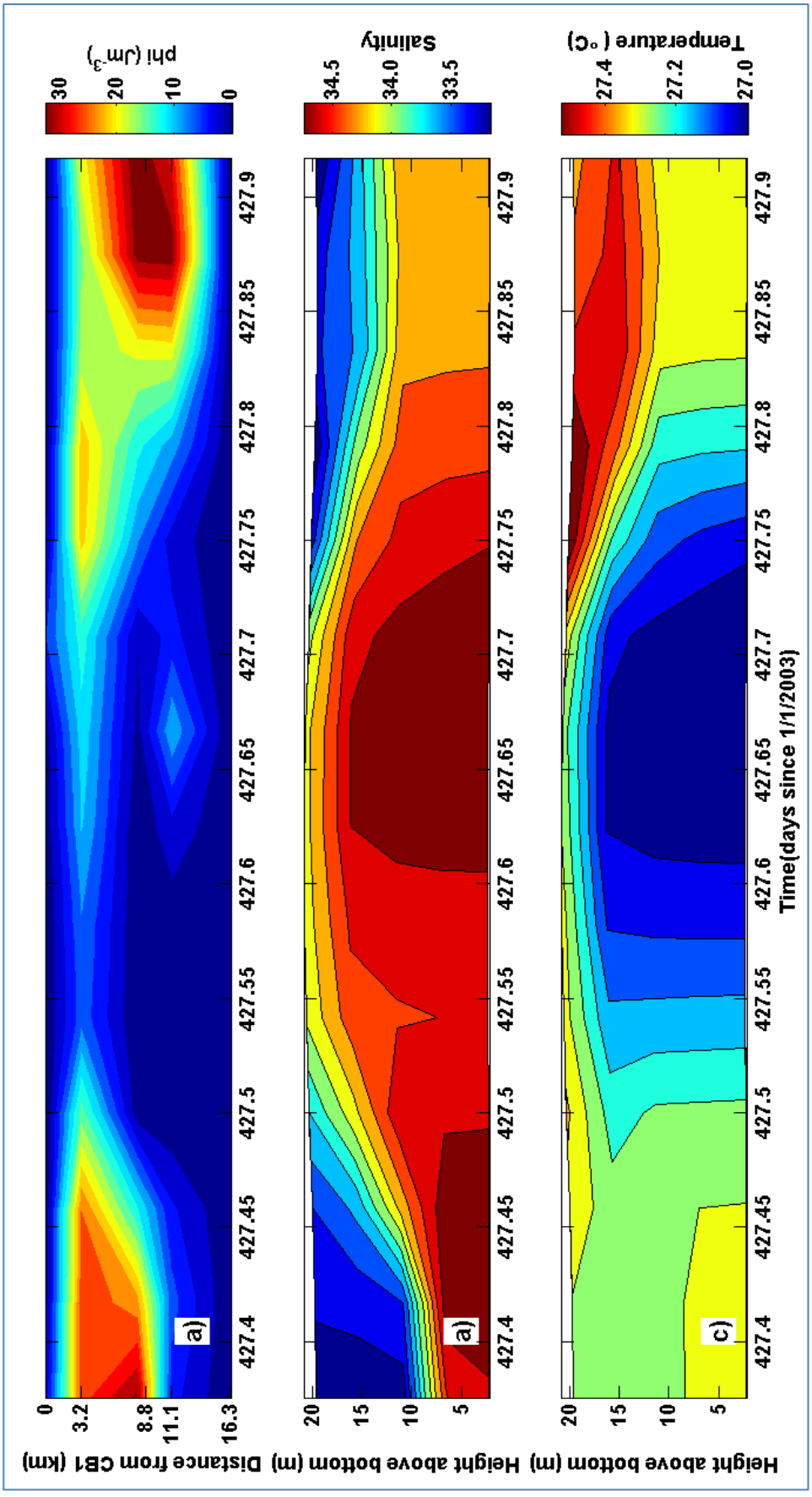

Figure 15: Predicted water column properties at section CB during neap tide for the old model: a) variation of potential energy anomaly φ over section CB, b) salinity profile at station CB2, c) water temperature profile at station CB2.

The model's performance concerning salinity and water temperature structures was furthermore determined by applying the RMSE and skill error parameters. Table 4 shows bay-wide and section-wide values of RMSE and skill for both, salinities and water temperatures. For this analysis, values for all depths as well as 11 different survey dates, ranging from dry to wet season conditions, were taken into account.

Table 4: RMSE and Skill Values for salinities and water temperatures per Section

	Salinity		Temperature	
	RMSE	Skill	RMSE	Skill
Bay-wide	1.66	0.84	0.62	0.99
Section A	1.46	0.88	0.56	0.99
Section B	2.33	0.78	0.66	0.99
Section CB	0.81	0.78	0.66	0.98

The water temperatures are represented well over all stations, with differences between predicted and observed temperatures of around 0.6°. Salinities, on the other hand, show different performances for the different sections. The worst performance, based on RMSE, was found for section B, while the best performance was found for section CB.

Next, a more detailed analysis was undertaken, taking into account values of RMSE and skill for each of the stations. The results can be found in Table 5 and the skill values are visually represented in Figure 16.

Table 5: RMSE and Skill Values for salinities and water temperatures per station

	Salinity		Temperature	
Station	RMSE	Skill	RMSE	Skill
A1	2.62	0.82	0.71	0.99
A2	1.50	0.90	0.60	0.99
A3	1.37	0.90	0.46	0.99
A4	1.31	0.88	0.44	0.99
A5	1.03	0.87	0.45	0.99
A6	1.06	0.84	0.44	0.99
A7	0.48	0.90	0.72	0.98
B1	1.54	0.87	0.74	0.98
B2	1.55	0.86	0.70	0.98
B4	1.63	0.87	0.67	0.99
B5	2.92	0.68	0.66	0.99
B6	2.64	0.71	0.72	0.98
B7	3.14	0.74	0.50	0.99
CB1	0.45	0.80	0.66	0.97
CB2	0.49	0.82	0.52	0.98
CB3	1.43	0.83	0.48	0.99
CB4	1.03	0.71	0.59	0.98
CB5	1.36	0.77	0.98	0.96

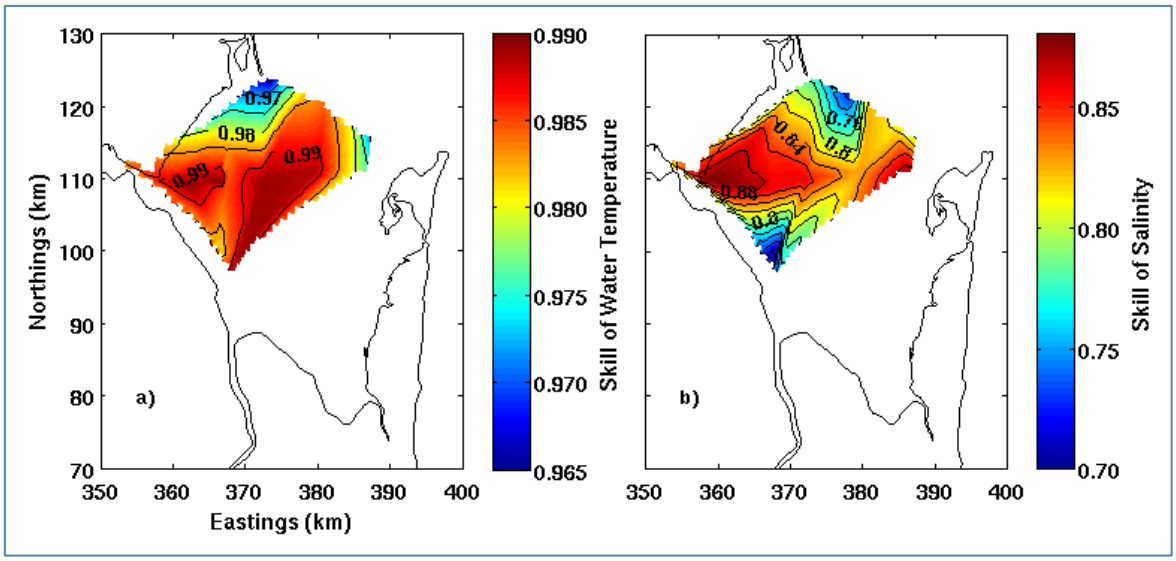

Figure 16: Skill values for a) water temperature and b) salinity, interpolated over part of the bay, over the 11 survey dates.

The data shows that water temperature is represented very well by the model, with maximum differences between predicted and observed temperatures of just under 1° found in station CB5. The skill map shows that generally water temperature differences were slightly larger near the river mouth of the Incomati River. This might be due to the predicted discharge water temperature being slightly different from the actual discharge temperatures. Salinities are represented less accurately by the model, with skill values of between 0.9 in the western part of the bay and down to around 0.68 in the southern part of the bay, indicating locally salinity differences of up to 3.

An analysis of the uncertainty in time was undertaken, considering observed and predicted salinities and water temperatures in all depths of all stations (Table 6).

Table 6: RMSE and Skill values for salinities and water temperatures per survey

	Salinity		Temperature	
Day	RMSE	Skill	RMSE	Skill
29. Jul 03	0.86	0.43	0.47	0.87
27-Sep-03	0.19	0.44	0.40	0.57
25-Oct-03	0.81	0.28	0.61	0.38
18. Nov 03	0.92	0.26	0.31	0.84
10-Dec-03	1.78	0.21	0.77	0.57
26. Jan 04	1.29	0.53	0.51	0.86
25-Feb-04	1.12	0.86	0.48	0.85
26. Mar 04	2.05	0.84	0.32	0.88
20-Apr-04	2.36	0.65	0.67	0.38
20-May-04	2.16	0.69	1.10	0.46
21. Jun 04	2.63	0.55	0.62	0.89

Due to the small variability within the data, the skill values are comparably low, even if the RMSE indicates a good fit of the model, with small differences in water temperatures and salinities.

Looking at the values of the RMSE for salinities it becomes evident that the model performance worsens with the season, changing from dry to wet season, with an increasing amount of freshwater in the bay. This means that the more freshwater is introduced, the more the model underestimates salinities.

To better understand the model's performance and get an insight into whether the model's overestimation of the salinity-deficit is possibly due to the predicted Maputo River discharge, a comparison of salinities of a total of 18 points in the bay (see Figure 4) was undertaken. Root Mean Square Errors (RMSE) were calculated to evaluate the model's performance based on differences in observed and predicted salinities.

A table summarising the RMSE result for salinities in all stations can be found in Appendix B. Figure 17 represents the results visually, interpolated over part of the bay, for 6 different survey dates.

High values of RMSE are generally found due to the model predicting lower salinities than those found in observations.

The results show that the RMSE increases in the wet season and with decreasing distance from the inflow of the Maputo River. Until the 18th of November, RMSE is generally at or below one, apart from a small stretch at the southern coast of the bay, adjacent to the area where the Maputo River flows into the bay, where RMSE increases to a value of around 2

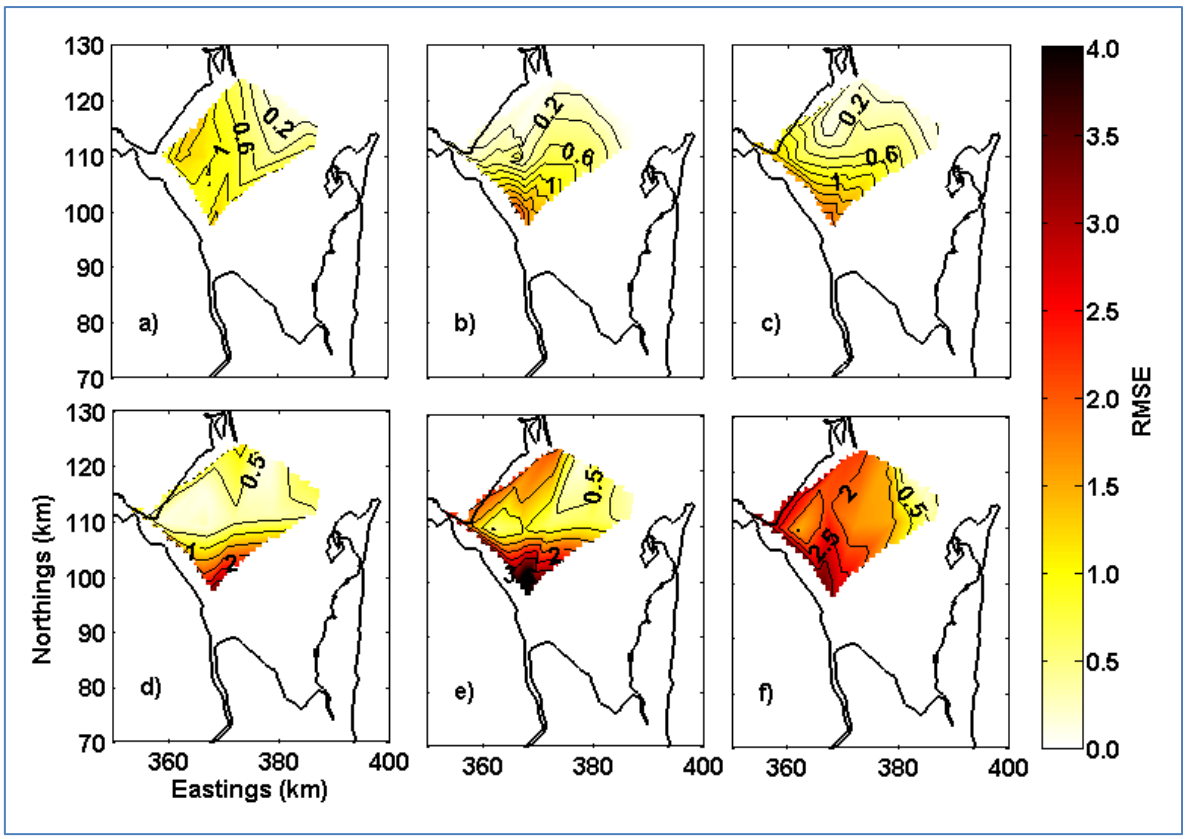

Figure 17: Maps of bay-wide salinity RMSE distribution over time in the Cartesian coordinate system: a) 29th of July, b) 25th of October, c) 18th of November, d) 26th of January, e) 26th of March, f) 20th of May.

Further into the wet season, after the first river discharge pulses have arrived, on the 26th of January, the RMSE near the Maputo River inlet has increased further, reaching values of up to 3.5 while the RMSE over most of the bay remains at values of 0.5. Two months later, on the 26th of March, after most of the wet season's fresh water has been discharged into the bay, the RMSE near the inlet of the Maputo River reaches its maximum value of around 4. Additionally, a tongue of high RMSE values extends from the river inlet along the coast towards the west. The bay's opening now has RMSE values of around 2 on the western part closer to the mouth of the Incomati and between 0.5 and 1 over most of the remaining opening. Towards the end of the wet season, on the 20th of May, the RMSE at the eastern side of the bay remains around 0.5 while most of the bay has RMSE values of 1.5-2.5 and the tongue of very high RMSE values of around 3.5 is still present, stretching from the Maputo River inlet towards the west along the coast.

Figure 18 shows the total RMSE for each of the sections. Section CB shows the best results, with RMSE values ranging between 0.5 in station CB1 at the eastern part of the bay's opening and between 1 and 1.5 over the western part. Section A shows highest RMSE values of 2.5 at the far western part of the bay, values of around 1.5 over most of the middle part of the bay, and around 0.5 in the eastern part. Section B, along the western part of the bay, shows the worst performance, with RMSE ranging between 1.5 in the North to a maximum of around 3.2 close to the Maputo River inlet. The bay-wide RMSE increases over time, ranging between 0 and 1 in the dry season and reaching values of up to 2.5 after the wet season.

The data therefore shows that uncertainties increase towards the inlet of the Maputo River into the bay, as well as with increasing freshwater discharge along the season. This is especially evident in the areas of very high RMSE on the 26th of March and the 20th of May, as well as the extensions of these lines towards the West along the coast.

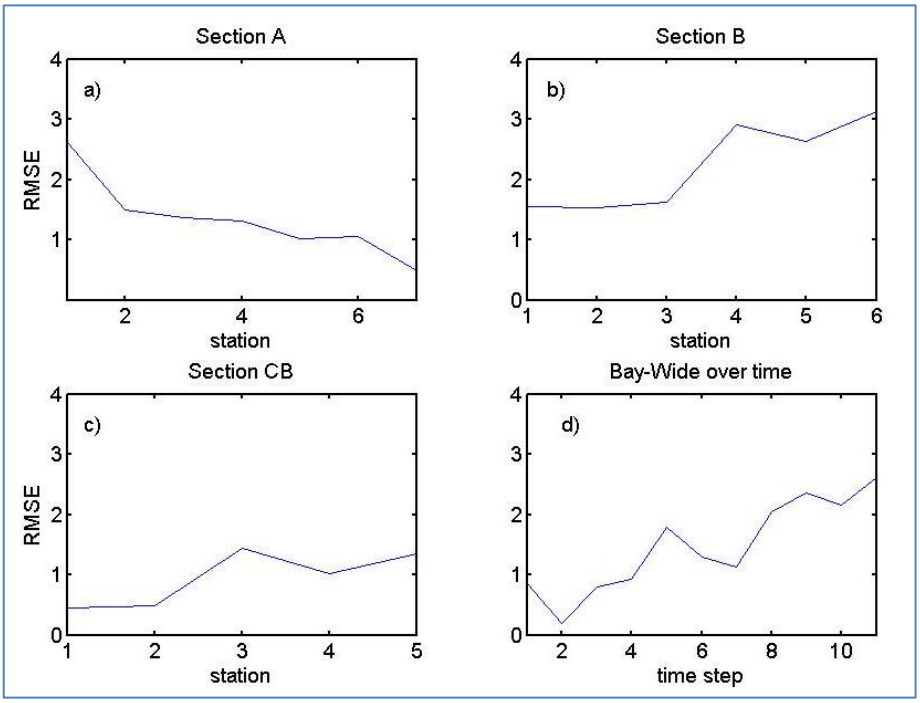

Figure 18: Comparison of RMSE of salinity per station, a) Section A, b) Section B, c) Section CB, d) Bay-wide over time

This thin high RMSE area can be explained by the spreading of the freshwater from the Maputo towards the west along the coast, which has been observed in the model runs.

Concluding, it was shown that now the model reproduces more accurately the semidiurnal and fortnightly stratification-mixing cycles occurring during the wet season. However, the model still predicts salinities lower than those found in observations. An analysis was conducted to investigate the spatial distribution of the uncertainty. Uncertainties increase towards the mouth of the Maputo River, for which only predicted river flow data was available to force the bay model, indicating this input as a possible source of the salinity deficit. Considering that the objective of this calibration was not a point-by-point calibration but rather to develop a model which is able to reproduce the general bay dynamics, it can be concluded that the model is calibrated to be applied to the purpose of this investigation.

3.3 Limitations of the Model

As stated by Lencart e Silva (2007), a hydrodynamic model's performance is largely influenced by the accuracy of the bathymetry used. The bathymetry that was applied in this model resulted from a number of surveys undertaken between the nineteen sixties and the nineteen eighties. Considering that Maputo Bay is a dynamic system, the bathymetry in 2003/04, when the observational data was obtained, may significantly differ from the bathymetry in the nineteen sixties to nineteen eighties.

Even after the calibration, uncertainties remain as to the origin of the high RMSE of the salinities as well as bay-average salinities over the year. A possible source of these uncertainties has been suggested to be the predicted origin of the Maputo River discharge, used as the input discharge of the model. Vertical overmixing by the model may also play a role. However, the model was able to reproduce the general bay dynamics during both spring and neap tides of the wet and dry season.

The dry season scenarios applied here, even runs not introducing any discharge, start after a spin-up time of three months during dry season. During these months, small amounts of freshwater are already introduced into the model domain. However, it is expected that these amounts of fresh water are sufficiently small not to significantly affect the model runs assuming no discharge into the model.

Another weakness of the model is the lack of mesoscale dynamics due to the limited spatial extent of the model outside of the bay. This means that no fronts on the shelf or mesoscale currents outside the bay can be represented.

3.4 Establishment of Modelling Specifications and Model Runs

After the model has been calibrated to a satisfying level, the final modelling specifications common to all production runs are those given in Table 7.

Table 7: Modelling specifications for Maputo Bay, adapted from Lencart e Silva (2007).

Parameter	Specification
Layers	15, top layers refined
Time Step	1 minute
Duration	20 days (runs 1-30)/40 days (runs 31-38)
Constituents	Salinity, water temperature, conservative tracer
Wind	No
Waves	No
Tide	Full harmonics
Initial Conditions for "dry season runs"	Warm start after 3 months-long dry season run
Initial Conditions for "wet season runs"	Warm start after 9 months-long dry-to-wet season run
Boundary Forcing	Water level with harmonic constituents
Reflection parameter alpha	100
Bottom roughness method	0.15 White-Colebrook Uniform
Wall slip condition	Free
Background horizontal eddy viscosity	1 m^2s^{-1}
Background horizontal eddy diffusivity	1 m^2s^{-1}
Background vertical eddy viscosity	10^{-4} m^2s^{-1}
Background vertical eddy diffusivity	10^{-4} m^2s^{-1}
Turbulence closure	*k-ε*
Drying and flooding threshold	0.1 m
Temperature	From heat flux model
Heat flux model	Absolute flux, net solar radiation

The production runs were set up from a warm start. This warm start is comprised of the same conditions as the final calibration run, including wind forcing, river flow from the rivers Incomati, Maputo, Umbeluzi, Tembe and Matola, a heat flux model as well as open-boundary forcing with tidal harmonic water levels, salinities and water temperatures. The production runs are divided into two main sets of scenarios: dry season and wet season scenarios. The dry season scenarios start after a three-months spin-up under dry season conditions. The wet season runs start after a 9-months spin up, starting in the dry season and ending in the middle of the wet season. They therefore represent wet season conditions, with a larger amount of freshwater already in the system.

The open boundary was divided into 14 sections and forced with water levels from harmonic constituents.

All production runs only use river discharge from the two main rivers, Incomati and Maputo.

Lencart e Silva (2007) concluded that wind forcing did not play an important role in forcing Maputo Bay. Furthermore could the wind from the observation station at Mavalene Airport not be directly related to the bay's hydrodynamics. No other wind data was available. The fact that

the wind could not be connected to the bay's hydrodynamics may be due to the large influence of tidal forcing and seasonal variation in river discharge, which may outweigh any effects of the usually light winds in Maputo Bay. Furthermore is the observation station possibly too far inland to represent the wind acting on the shelf region off Maputo Bay. It was therefore chosen not to include wind forcing in the production runs.

A conservative tracer was introduced to all runs at the moment of the start of discharge. The tracer was applied with a concentration of I kgm^{-3} to the area covered by the mask in Figure 20 on page 50. Using the conservative tracer helps determine flushing times in the bay which can be inferred from the development of tracer concentrations in time.

Dry season runs

For the dry season runs, a set of four different river discharges was chosen as a parameter in the model runs:

- The first scenario was the basecase, where no freshwater is discharged into the bay;
- The second scenario was an average dry season discharge with a return period of around twelve days during the dry season;
- The third scenario was an average wet season discharge, with a return period of five times per wet season;
- The fourth scenario represented an extreme wet season discharge, with a return period of five years.

All values were calculated from a data set of daily values for the Maputo and Incomati River discharge for a period of 10 years. A generalized extreme value inverse cumulative distribution function was fitted to the data (RMSE 0.0746) and the discharges for the various return periods were calculated. In order to get a pulse-like discharge, the discharge that would usually occur over five days was used and forced in the model as a three-day discharge. This way, the amount of freshwater represented the return periods and would force the hydrodynamics as a pulse. It is thus easier to discharge the water in a certain moment of the spring-neap cycle. Only the rivers Incomati and Maputo were taken into account, as the remaining rivers play a much less significant role in forcing the hydrodynamics of Maputo Bay. To find out whether the influence of the Incomati and Maputo on the bay's hydrodynamics differ, the relative discharge ratios were varied. As a basecase, a ratio of 3:2 (discharge Incomati : discharge Maputo) was chosen, which is approximately the ratio found in reality. The other ratios applied were 4:1 (more Incomati discharge) and 1:4 (more Maputo discharge). To find out whether the timing of the arrival of the freshwater pulse in the bay (in relation to the moment in the spring-neap tidal cycle) has an influence on the dynamics, the pulses were introduced in four different timings:

- During spring tide;
- In the transition from spring to neap tide;
- During neap tide;
- In the transition from neap and spring tide.

Wet season runs

For the wet season runs, only the extreme discharge was used. In the initial conditions, a lot of fresh water is already present in the bay. Introducing a small or no discharge would therefore not produce useful results. The discharge was introduced during spring or neap tide and ratios of Incomati : Maputo discharge were varied in the same way as for the dry season runs. The initial conditions for the wet season runs consisted of a warm start after 9 months of model run. This included the large freshwater discharge around days 390-400 (please refer to Figure 9c on page 32 for the development of river discharge for the model input before the start of the scenarios), after which an average discharge was introduced consistently over the following 25 days for runs starting at neap tide and 32 days for runs starting at spring tide. This approach was chosen to reach similar initial salinity fields for runs starting during spring and neap tide, even though their start days lie 7 days apart. The discharges chosen as a base discharge are the average discharges during February and March for the Incomati and the Maputo and had values of 230 m^3s^{-1} and 200 m^3s^{-1}, respectively. Unlike the dry season runs, the baseline discharge of the wet season runs was also maintained after the introduction of the extreme freshwater pulse. The discharge did not go to zero after the introduction of the pulse, but was maintained at the baseline discharge values. On top of varying the timing of the discharge pulse as well as the ratio between the two main rivers, the duration of the pulse was also varied.

Apart from the runs with a 3-day pulse as was the case in all previous runs, the same total amount of freshwater was also introduced over different time spans:

- 3 days (basecase);
- 2 days;
- 5 days;
- 10 days.

Figure 19 shows the pattern of the discharge used for the runs with varying durations of the freshwater pulse. The total amount of freshwater introduced over the duration of the simulation is the same for all runs.

Varying these different characteristics, a set of 38 different scenarios was developed in order to study the bay's hydrodynamics as well as the possible conditions of the arrestment of estuarine plumes. All scenarios are summarised in Table 8.

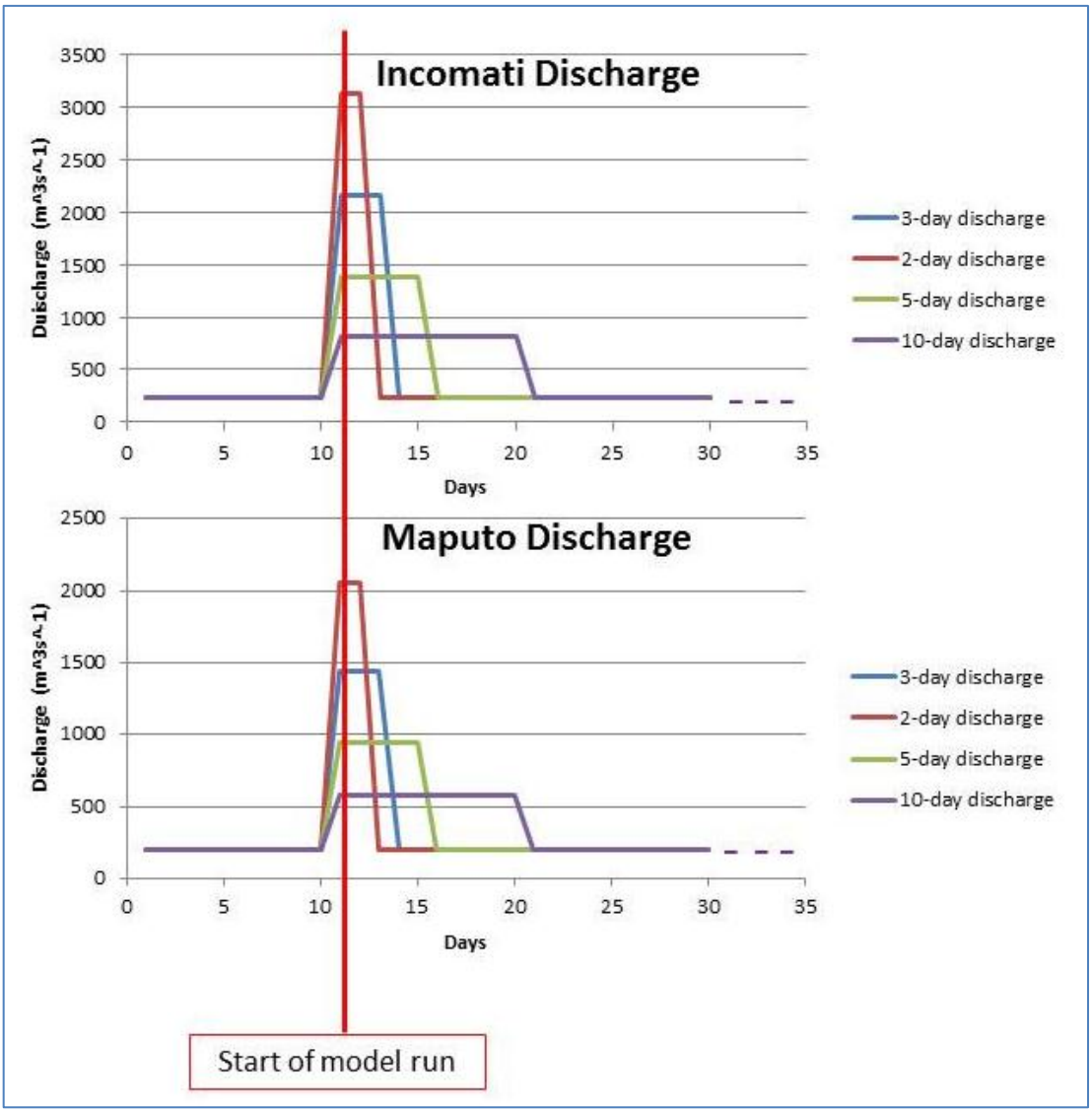

Figure 19: Pattern of varying durations of discharge pulses for wet season runs.

Table 8: Overview of the characteristics for each of the model runs

Nr	Name	Incomati River		Maputo River		Ratio Incomati: Maputo	Timing of Discharge	Season
		Discharge (m^3s^{-1})	Duration (days)	Discharge (m^3s^{-1})	Duration (days)			
1	nofwSpring	0	3	0	3	3:2	Spring Tide	Dry
2	nofwSpNp	0	3	0	3	3:2	Spring to Neap	Dry
3	nofwNeap	0	3	0	3	3:2	Neap Tide	Dry
4	nofwNpSp	0	3	0	3	3:2	Neap to Spring	Dry
5	nlowSpring	48	3	32	3	3:2	Spring Tide	Dry
6	nlowSpNp	48	3	32	3	3:2	Spring to Neap	Dry
7	nlowNeap	48	3	32	3	3:2	Neap Tide	Dry
8	nlowNpSp	48	3	32	3	3:2	Neap to Spring	Dry
9	navSpring	612	3	408	3	3:2	Spring Tide	Dry
10	navSpNp	612	3	408	3	3:2	Spring to Neap	Dry
11	navNeap	612	3	408	3	3:2	Neap Tide	Dry
12	navNpSp	612	3	408	3	3:2	Neap to Spring	Dry
13	nexSpring	2160	3	1440	3	3:2	Spring Tide	Dry
14	nexSpNp	2160	3	1440	3	3:2	Spring to Neap	Dry
15	nexNeap	2160	3	1440	3	3:2	Neap Tide	Dry
16	nexNpSp	2160	3	1440	3	3:2	Neap to Spring	Dry
17	iavSpring	816	3	204	3	4:1	Spring Tide	Dry
18	iavNeap	816	3	204	3	4:1	Neap Tide	Dry
19	iexSpring	2880	3	720	3	4:1	Spring Tide	Dry
20	iexNeap	2880	3	720	3	4:1	Neap Tide	Dry
21	mavSpring	204	3	816	3	1:4	Spring Tide	Dry
22	mavNeap	204	3	816	3	1:4	Neap Tide	Dry
23	mexSpring	720	3	2880	3	1:4	Spring Tide	Dry
24	mexNeap	720	3	2880	3	1:4	Neap Tide	Dry
25	wnexSpring	2160	3	1440	3	2:3	Spring Tide	Wet
26	wnexNeap	2160	3	1440	3	2:3	Neap Tide	Wet
27	wmexSpring	720	3	2880	3	1:4	Spring Tide	Wet
28	wmexNeap	720	3	2880	3	1:4	Neap Tide	Wet
29	wiexSpring	2880	3	720	3	4:1	Spring Tide	Wet
30	wiexNeap	2880	3	720	3	4:1	Neap Tide	Wet
31	wnex2Spring	3125	2	2060	2	2:3	Spring Tide	Wet
32	wnex2Neap	3125	2	2060	2	2:3	Neap Tide	Wet
33	wnex3Spring	2160	3	1440	3	2:3	Spring Tide	Wet
34	wnex3Neap	2160	3	1440	3	2:3	Neap Tide	Wet
35	wnex5Spring	1388	5	944	5	2:3	Spring Tide	Wet
36	wnex5Neap	1388	5	944	5	2:3	Neap Tide	Wet
37	wnex10Spring	809	10	572	10	2:3	Spring Tide	Wet
38	wnex10Neap	809	10	572	10	2:3	Neap Tide	Wet

3.5 Data Processing Methods

This section will explain the methodology applied to the model outputs to produce the results shown in Chapters 4 and 5.

Vertical Salinity/Water Temperature Differences

Vertical salinity and water temperature differences were calculated along a cross section of the bay's opening. A total of 9 stations were used to produce the cross-section figures: CB1, CB2, CB3, CB4, CB5, CN1, CN2, CN3 and CN4 (please refer to Figure 4 for the locations of these stations). The vertical differences were calculated by subtracting surface layer values from bottom layer values:

ΔS_v =Salinity$_{bottom}$ - Salinity$_{Top}$

ΔT_v =Temperature$_{bottom}$ - Temperature$_{Top}$

The vertical differences were then plotted taking into account the distances between the stations, interpolating values in between two stations. The *y*-axis represents values as a function of distance from CB5, so that the top of the plots represents the Northwest of the bay's opening and the bottom of the plots represents the Southeast of the bay's opening. Values were linearly interpolated.

Bay-Average Salinities and Tracer Concentrations

Bay-average values were calculated from map-data for each of the grid cells. A mask was applied to filter out the areas of the river arms as well as the area offshore of Maputo Bay. The extent of the mask can be seen in Figure 20.

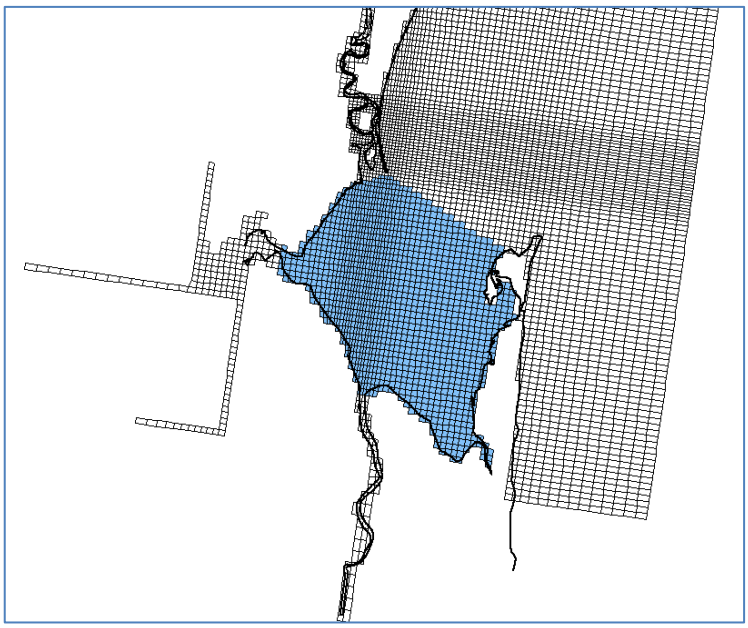

Figure 20: Grid area included in the mask to calculate bay-average values. Blue area indicates mask.

After all data outside the bay was masked out, weighed averages as a function of volume were calculated to take into account the temporally-varying water depths as well as different vertical layer depths and horizontal cell areas. To filter out the tidal signal, a pl33 filter was applied.

This low-pass filter is described by the following generating function for weights (Woods Hole Oceanographic Institute, 1985):

$$weight = \left[\frac{2\sin(0.06\pi t)}{0.0009\pi^3 t^3} - \frac{\sin(0.03\pi t) + \sin(0.09\pi t)}{0.009\pi^3 t^3}\right] \quad \textbf{(48)}$$

The filter has a half-amplitude period of 33 hours. Therefore, the first and last 33 hours of the data should not be taken into account after filtering.

Potential Energy Anomaly

To define the stability of the vertical stratification, the potential energy anomaly φ was calculated.

Simpson et al. (1978) defined φ as the amount of work required to bring about complete vertical mixing, written as:

$$\varphi = \frac{1}{h}\int_{-h}^{0}(\rho - \langle\rho\rangle)\, gz\, dz \quad \textbf{(49)}$$

with $\langle\rho\rangle = \frac{1}{h}\int_{-h}^{0}\rho\, dz$,

where h is the depth of the water column and ρ is density. When the water column is vertically completely mixed, φ is zero. The larger φ is, the stronger is the stratification.

Φ was calculated from the density values in the centres of the vertical layers over the cross section described earlier in this chapter.

Residual Velocities

The residual velocities were calculated over the cross section of the bay's mouth to help understand bay-shelf exchange. The pl33 filter was applied to obtain subtidal residual velocities. The velocities were then plotted for various time steps separately, with the *x*-axis representing the horizontal cross section and the *y*-axis representing depth. Values were linearly interpolated.

Flushing Times

The tracer concentrations were translated into dynamic flushing times. According to Monsen et al., the flushing time is a "*bulk or integrative parameter that describes the general exchange characteristics of a waterbody without identifying the underlying physical processes, the relative importance of those processes, or their spatial distribution*" (2002).

The flushing times were calculated from the decay of bay-average tracer concentrations. It was assumed that the tracer concentration declines exponentially within the bay.

The decay of the tracer concentration in the bay can then be described by

$$\frac{\partial C}{\partial t} = -\frac{Q_o}{V} C \quad \textbf{(50)}$$

The logarithm of tracer concentration for each time step is then:

$$\ln\big(C(t)\big) = C_0 - kt \quad \textbf{(51)}$$

where $k = \frac{1}{\tau}$ with τ being the flushing time.

This decay is exponential if Equation 50 is integrated with respect to time from the initial concentration C_0

$$C(t) = C_0 e^{-kt} \quad \textbf{(52)}$$

Flushing times were obtained by fitting a regression line to a moving 5-day window of concentrations for each time step.

The original concentrations were plotted with the concentrations calculated from the regression analysis to analyse visually the fit of the regression (please see Appendix C for the figures). The R^2 statistic varies around 0.94-0.99 over most of the research period. The fit of the regression lines was thus confirmed and the lines were used to calculate dynamic flushing times for the 5-day window. The figures showing the fit of the regression line are shown in Appendix C.

Even though the models were run for 20 days, after filtering and applying the regression analysis the first and last 63 hours should not be taken into account. Flushing times are therefore only shown for a decreased time span. Due to the large variation of the tidal amplitude between spring and neap tide, the run time of the model is not enough to reach a final flushing time for each of the model runs as flushing times show very strong variations over the spring-neap cycle. It is, however, possible to determine the dynamic flushing times over the spring-neap cycle.

4 Dry Season Runs – Results and Discussion

This Chapter will present the results for the runs that are considered "dry season runs", including runs 1-24 (please see Table 8 for details). This means that they begin from a warm start initial condition set in the dry season. Different river discharges are applied. The "average" and "extreme" discharge runs are more typical for the wet season but may occur during the end of the dry season when the first freshwater pulses arrive or as extreme events throughout the year.

Firstly, the vertical salinity differences across the bay opening are investigated to understand the timing of the freshwater pulses at the bay's opening as well as the cycle of mixing and stratification induced by tidal stirring. Next, bay-average salinities are shown to get an understanding of the export of salt water over time under varying timings of discharge as well as varying discharge ratios between the Incomati and the Maputo. Vertical water temperature differences across the bay's opening are then shown to help interpret the stratification-mixing cycles due to the influence of water temperature variations. The stratification-mixing cycle is then investigated over the duration of the model runs to understand how the tidal spring-neap cycle in combination with different overall amounts, ratios and timings of discharge influence the stratification and mixing of the bay. Residual velocities are shown during different conditions, including spring and neap tide, to investigate whether the estuarine circulation is arrested under any of the conditions covered by the various scenarios. Bay-average concentrations of a passive tracer are then shown and used to calculate flushing times in the bay to help understand under which conditions the bay-shelf exchange is most and least efficient.

4.1 Vertical Salinity Differences

Results

The vertical salinity differences (ΔS_v) were determined along a cross-section of the bay's opening by subtracting surface salinities from bottom salinities.

Figure 21 shows the bathymetry across the bay's opening.

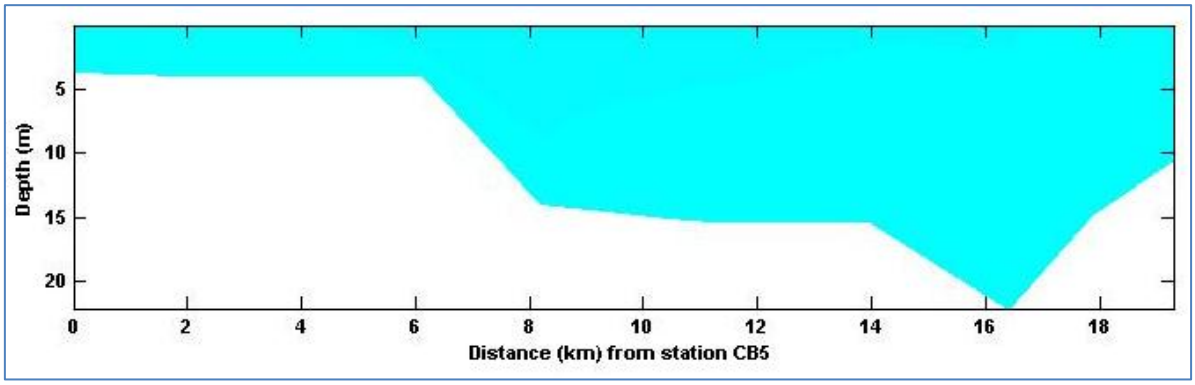

Figure 21: Bathymetry over the bay's opening.

For the runs without freshwater discharge, with dry season discharge and with average wet season discharge, these values were very similar and very small, usually reaching variations of less than ±0.1. These results are therefore not visually represented here.

ΔS_v for the extreme discharge runs showed larger variations and can be seen in Figure 22. Here, ΔS_v were always positive, indicating lower salinities in the surface compared to the bottom layer. A clear semidiurnal cycle alternating between no/small and large ΔS_v was observed. The differences were largest when discharge was introduced during spring tide (Figure 22a) or between spring and neap tide (Figure 22b), reaching differences of up to 30. The largest values of ΔS_v were usually found at the stations 6.1 and 8.1 km away from station CB5 at the north-western end of the bay opening. This does not correspond to the deepest parts of the bay, but to water depths of 3-15 m. If discharge occurred during neap tide or between spring and neap tide, maximum ΔS_v of 25 were found. However, the extension of these peaks, both in time and over the bay's opening, was much smaller than for discharge during spring or between spring and neap tide. The earliest arrival of ΔS_v peaks was found for the run with discharge between spring and neap tide (approximately after 60 hours, Figure 22b), while all other runs showed arrivals of ΔS_v peaks around 12 hours later. The longest period of ΔS_v peaks was found when discharge was introduced during spring tide (Figure 22a), lasting approximately until 240 hours after the simulation start and extending over most of the bay's opening. First peaks of ΔS_v for discharge during spring or between spring and neap tide occurred at the stations located 6.1 and 8.1 km away from CB5, in the northwest of the bay. During neap tide, significant values of ΔS_v spread further towards the northwest, while between neap and spring tide. Significant values of ΔS_v were observed further towards the Southeast. For the runs starting at neap or between neap and spring tide, however, the peaks did not extend over a large area of the opening.

Apart from the first spring tide in Figure 22, representing discharge between neap and spring tide, there were no significant ΔS_v during spring tide. Neap tides, on the other hand, usually showed the largest values of ΔS_v .

Summarising, values of ΔS_v start to be significant around 60-70 hours after the start of freshwater discharge and are largest around 6-8 km away from the north-western part of the mouth. When freshwater discharge occurs during spring tide or between neap and spring tide, variations are larger than when discharge occurs during neap or between neap and spring tide. Generally, values of ΔS_v are large during neap tide and small during spring tide.

Discussion

The absence of significant vertical salinity differences for the runs without discharge, with dry season discharge and with average wet season discharge can be explained by the significantly lower input of freshwater. Taking into account that the runs start in a dry season environment with little freshwater present in the bay, even the average wet season discharge over three days is not enough to produce significant vertical salinity differences.

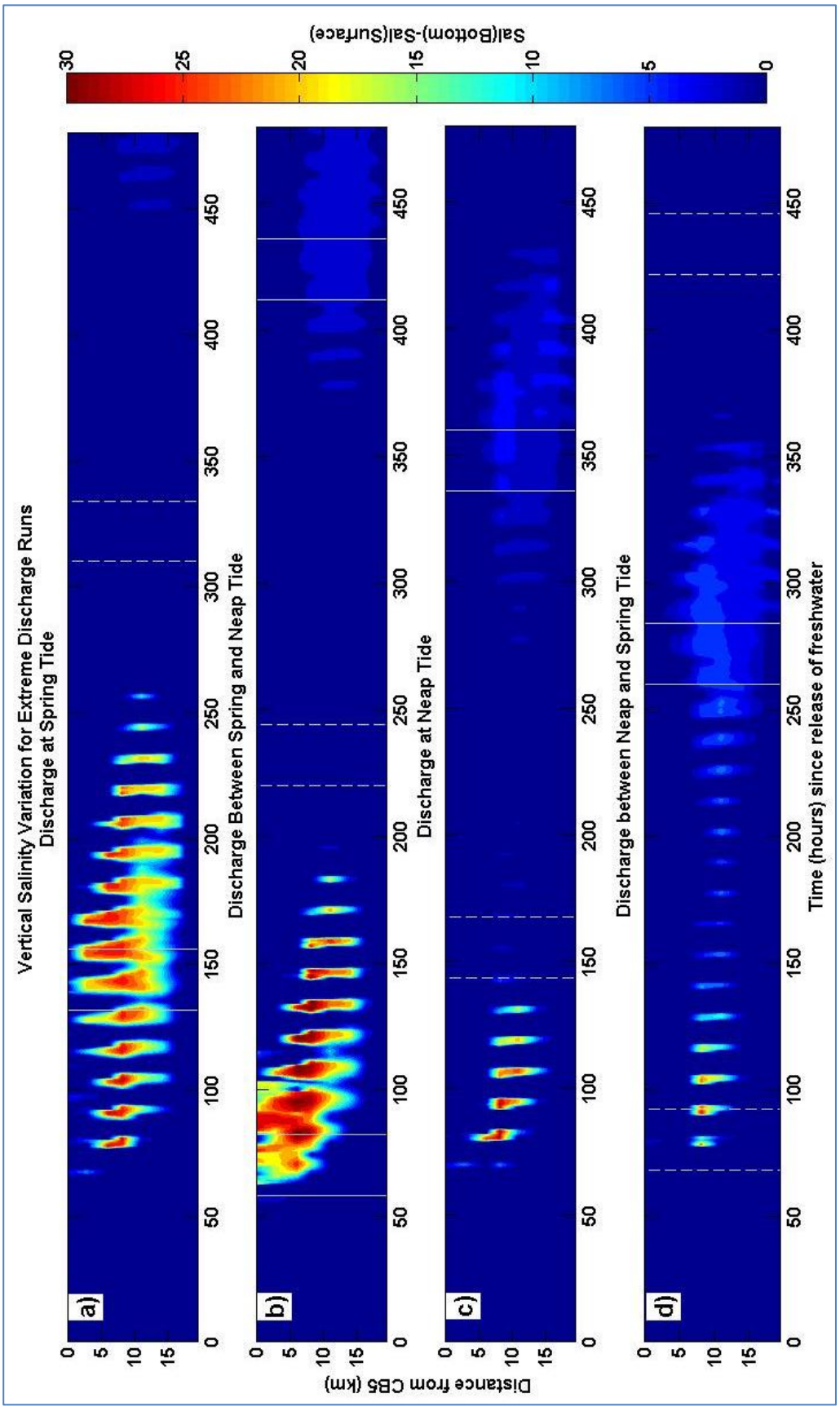

Figure 22: Variation of salinity differences between bottom and surface layer across Maputo Bay's mouth for extreme discharge during the dry season at a) spring tide , b) between spring and neap tide, c) at neap tide and d) between neap and spring tide. Solid vertical lines indicate time of neap tide, dashed vertical lines indicate time of spring tide.

The tide works on the bay hydrodynamics in a number of ways: directly through advection and dispersion, through shear dispersion as a combination of vertical mixing and tidal straining, as well as through tidal rectification. When the tidal range is larger, all of these mechanisms become stronger.

Largest vertical salinity differences were usually found during neap tide, when mixing from tides was weak and the water column could stratify. During spring tide, on the other hand, mixing was stronger and eroded any vertical salinity gradients. The only time that vertical salinity variations were observed during spring tide was for the run where discharge was introduced between neap and spring tide. In this case, the arrival of the estuarine plume from the rivers at the bay opening corresponded to the timing of spring tide. The vertical salinity differences were limited over a small area across the opening and were eroded soon after by the mixing forces of the tide.

A possible reason for the varying spatial extent of salinity differences with the moment of discharge in relation to the spring-neap cycle can be found in mixing. If the freshwater discharge is induced during spring tide or between spring and neap tide it is prone to less tidal forcing in the first days of being in the bay, due to the tidal forces decreasing towards neap tide. There is therefore significantly less mixing of the fresh river water with the saline bay water. If, on the other hand, the discharge is induced during neap or between neap and spring tide, the tidal forcing becomes increasingly stronger towards spring tide. This means that the freshwater from the rivers, once entering the bay, is subjected to a much stronger tidal forcing, mixing freshwater from the rivers with saline bay water. This can explain the larger salinity differences as well as the longer presence of large salinity variations for the model runs with discharge during spring or between spring and neap tide. The large salinity differences are first found approximately 6-8 km away from the north-western end of the bay's opening as the freshwater leaves the bay at the north-western part of the opening, turning left when leaving the bay. The salinity differences at the far north-western part of the bay-opening are often smaller due to the smaller water depth. The amount of mixing induced from tidal currents depends on the water depth. Simpson and Hunter (1974) developed the criterion h/u_t^3 to define the spatial position of a front between mixed and stratified conditions, where h is the depth of the water column and u_t is the tidal velocity amplitude. This criterion can help to determine whether or not stratification develops. Considering a case of small horizontal advection and small wind effects, the criterion can be used to determine the balance between heating and stirring:

$$\frac{Q_h h}{u_t^3} \geq \frac{8 \in k_d \rho c_p}{3\pi \alpha_v g} \qquad \textbf{(53)}$$

where c_p is the specific heat, Q_h is the heating rate, $\in$ is the efficiency of tidal mixing, α_v is the volume expansion coefficient, k_d is the drag coefficient and ρ the density. This equation represents the exact balance between heating and stirring and therefore indicates the location of a front between mixed and stratified conditions (Simpson, 1998).

The more shallow the water is, the more friction is induced, mixing the water column. Therefore the water column is vertically mixed over the shallow banks in the north-western part of the bay-opening, not producing significant vertical salinity gradients. Only during neap tide, when mixing

is very weak, can the water column stratify over these shallow banks, producing the vertical salinity differences seen in Figure 13 a and b. Later on, when the Maputo River water also reaches the bay's opening, as well as with more mixing occurring after neap tide, the extension of the estuarine plume over the bay's opening increases and the larger salinity differences can be found extending over a larger area of the bay's opening.

The semi-diurnal cycle of the salinity difference signal can be explained by tidal straining: apart from inducing stirring, tides can also lead to periodic stratification where horizontal density gradients exist. Simpson et al. (1990) investigated this phenomenon theoretically and confirmed their theories through observations for Liverpool Bay. They found that the vertical shear inserted by tides acts on the existing horizontal density gradients. This can, if horizontal density gradients are sufficiently strong, lead to distortions of the previously vertical isohalines due to surface waters being able to move faster than bottom layers, thus inducing stratification during ebb. During flood, the tide forces heavier water on top of lighter water, creating instabilities. Through these instabilities the water mixes vertically and horizontal gradients develop again, thus introducing periodic fluctuations. This process is also called Strain-Induced Periodic Stratification (SIPS). The periodic absence and presence of vertical salinity gradients was therefore only found until approximately halfway between neap and spring tide, before tidal stirring increased again.

4.2 Bay-average Salinities

Results

Bay-average salinities were calculated and the tidal signal was filtered out. Results are shown in Figure 23. Due to the filter that was applied, the first and last 33 hours of the data should not be taken into account.

Over the first 72 hours, corresponding to the duration of the discharge, the bay-average salinities dropped most significantly. In the runs where an average discharge was induced, bay-average salinities for the 3:2 ratio (discharge Incomati : discharge Maputo) dropped from around 35 to 34.8. Runs with the extreme discharge dropped to around 32.9 in the same period. Afterwards, during neap tide, average discharge runs showed a further decrease in bay-average salinities, which was smaller just after neap tide.

The dry season runs with an extreme wet season discharge showed increasing bay-average salinities during neap tide and stable bay-average salinities during spring tide.

Overall, bay-average salinities at the end of the simulation were slightly lower when discharge was induced during neap tide. Changes in bay-average salinities were always larger when the discharge of the Maputo was larger (1:4 discharge ratio), independent of timing or amount of discharge.

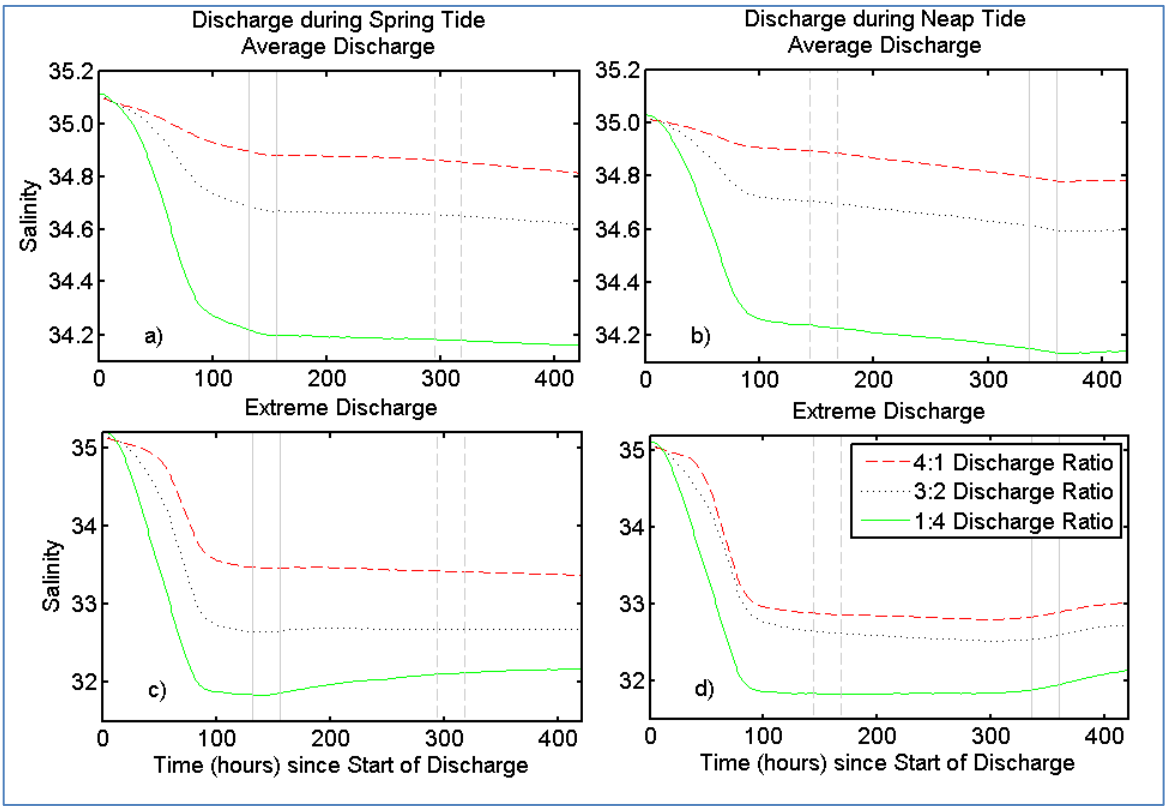

Figure 23: Tidally-filtered bay-average salinities over time during dry season for a) average discharge during spring tide, b) average discharge during neap tide, c) extreme discharge during spring tide and d) extreme discharge during neap tide. The red dashed line represents a 4:1 ratio of Incomati discharge : Maputo discharge, the dotted black line represents a 3:2 Incomati : Maputo discharge ratio and the solid green line represents a 1:4 Incomati : Maputo discharge ratio. Solid vertical lines indicate time of neap tide, dashed vertical lines indicate time of spring tide.

Discussion

Bay-average salinities were lower when more freshwater was introduced. In the average discharge runs, the longer time it takes to recover from the discharge is a clear indication of tidal stirring disrupting the density driven current. In the extreme discharge case the density-driven currents through the bay opening are stronger. The larger discharge leads to increased buoyancy inside the bay which generates density driven currents sooner after spring tide in comparison with the average discharge case. The relative differences between runs with different discharge ratios can be explained by the locations of the river mouths in the bay. The Incomati River mouth is located close to the north-western part of the opening of Maputo Bay, whereas the Maputo River mouth is located in the southern part of the bay. Discharge introduced to the Incomati therefore tends to leave the bay quicker, without influencing a large area of the bay. Discharge introduced to the Maputo, on the other hand, influences a larger area of the bay and takes longer to reach the bay's opening.

Therefore, if the discharge of the Maputo is larger than that of the Incomati, bay-average salinities decrease more significantly. The differences between discharge during spring and neap tide can be explained by tidal mixing. The discharge that is introduced during spring tide is, in the first days in the bay, influenced by decreasing tidal mixing.

After the 72 hours of discharge, bay average salinities for some runs kept lowering, probably due to the freshwater present in the rivers which were not part of the calculation of bay-average salinities. The average discharge runs showed a stabilizing of bay-average salinity corresponding with neap tide. It is assumed that in this moment, exchange with the shelf was larger so that export of freshwater from the bay to the shelf was about the same as input of freshwater that was still present in the river arms.

When discharge is introduced during neap tide, tidal mixing increases over the first days. Confirming the conclusions by Linden and Simpson (1988), bay-average salinities for the runs with extreme discharge at neap tide showed salinities plateauing over a longer period of stronger mixing during spring tide, and started to increase again during neap tide, when mixing was decreased and the water column could stratify again, developing efficient density currents which transported salinity out of the bay. The increase in salinities was smaller and slower for the runs with an average discharge, due to less buoyancy having been present in the bay. Furthermore can this increase in salinity during weaker mixing associated with neap tide also be found in the runs with a 1:4 discharge introduced at spring tide. After an initial strong decrease of salinities in the first 100 hours, the bay-average salinities reached a minimum at around neap tide and then increased visibly, with increases becoming smaller towards the larger mixing associated with spring tide. The effect is largest for an extreme discharge with a ratio of 1:4 (more Maputo river discharge), as the Maputo plume influences a larger area of the bay.

4.3 Vertical Water Temperature Differences

Results

Differences between the bottom and surface water temperatures were calculated in the same way as the salinity differences, with positive values indicating larger bottom temperatures and negative values indicating larger surface temperatures. The results for runs without discharge can be found in Figure 24. For these runs, vertical water temperature differences (ΔT_v) were usually negative, indicating larger surface temperatures. A pattern can be found which is common to all runs: a peak of ΔT_v of around 3.5° C which occurred after around 430 hours for the run starting between spring at neap tide (Figure 24b), 355 hours for the run starting at neap tide (Figure 24c) and 280 hours for the run starting between neap and spring tide (Figure 24d). The runs with dry season discharge and average wet season discharge showed very similar results and are therefore not represented here. Results for extreme discharge runs can be seen in Figure 25. The same pattern of a moving 3.5°C temperature difference that was found for the no-discharge runs is also present here. Furthermore were some values of up to +5°C found, indicating surface water temperatures 5°C colder than bottom temperatures. This was found for the runs starting at spring tide or between spring and neap tide and occurred especially near station CB5 and later also extending over a larger area.

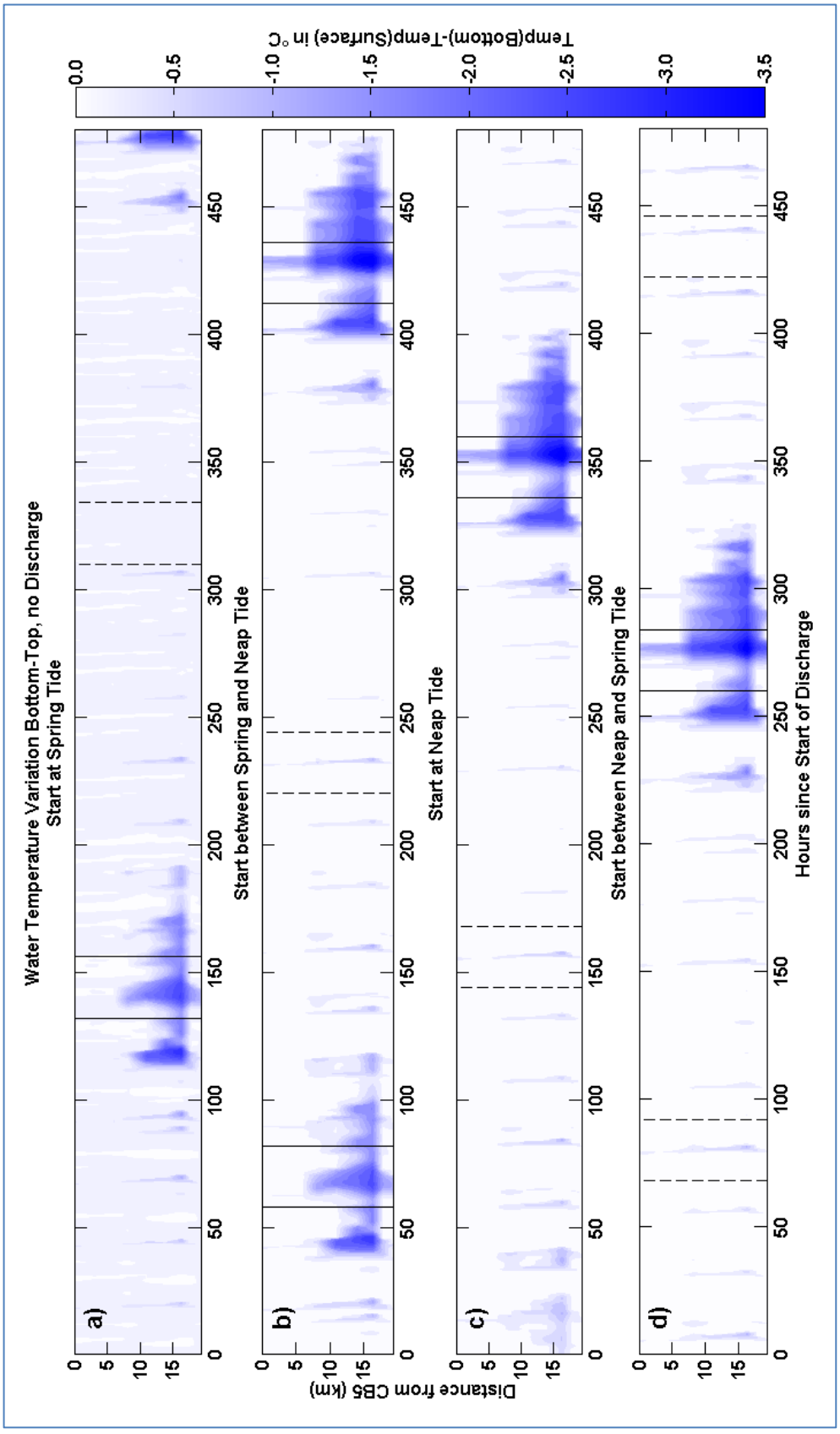

Figure 24: Variation of water temperature differences between bottom and surface layer across Maputo Bay's mouth for runs without river discharge during dry season, a) starting at spring tide, b) starting between spring and neap tide, c) starting at neap tide and d) starting between neap and spring tide (d). Solid vertical lines indicate time of neap tide, dashed vertical lines indicate time of spring tide.

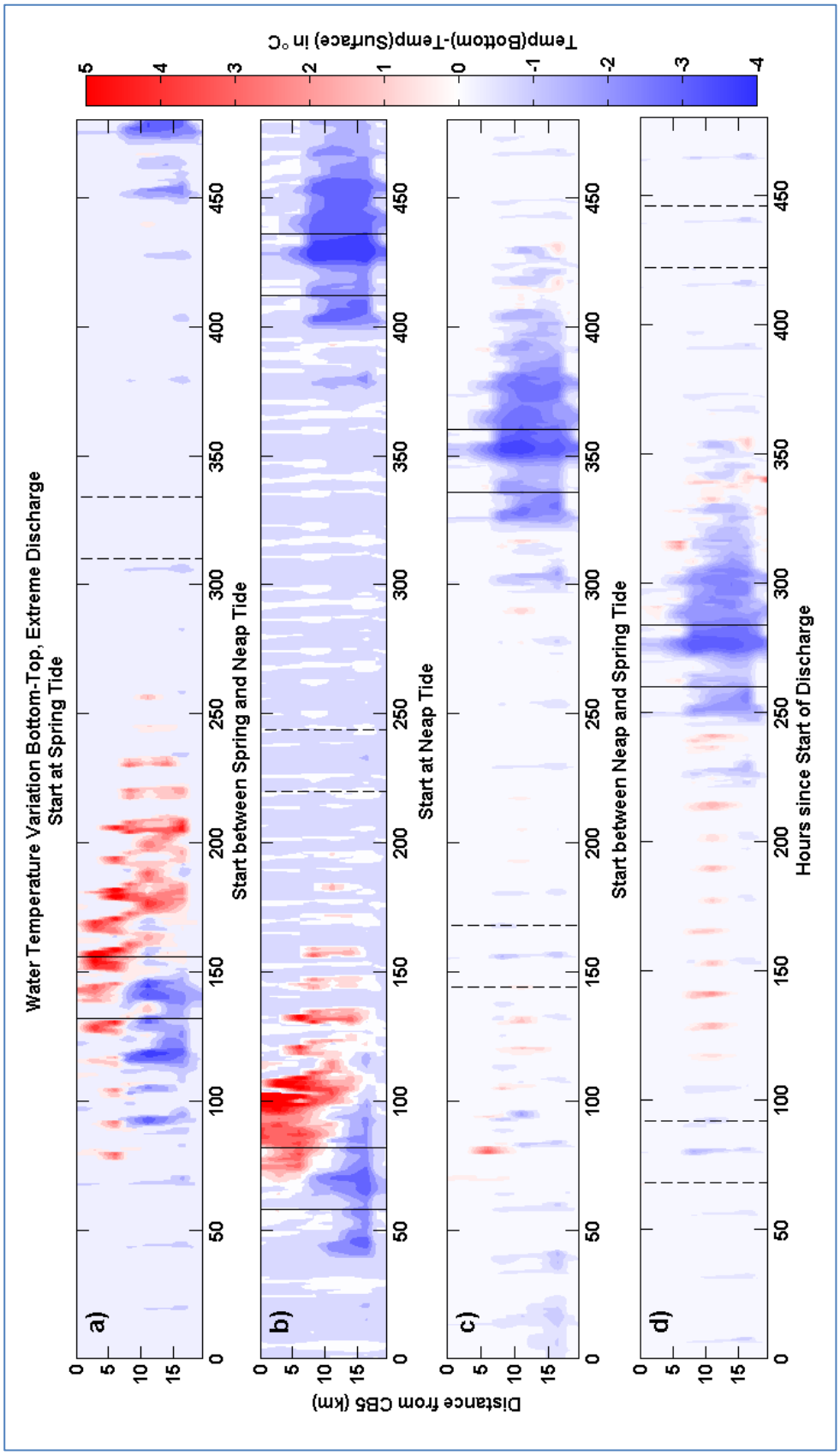

Figure 25: Variation of water temperature differences between bottom and surface layer across Maputo Bay's mouth for extreme river discharge during dry season, a) starting at spring tide, b) starting between spring and neap tide, c) starting at neap tide and d) starting between neap and spring tide (d). Solid vertical lines indicate time of neap tide, dashed vertical lines indicate time of spring tide.

Discussion

The apparent movement of the peak of ΔT_v for the no-discharge runs can be explained by the delay of the start of the model runs, indicating that these peaks represent in fact the same days of the year. After analysing the atmospheric model input it became apparent that this peak in temperature differences is, for a part, due to high inputs of air temperatures and solar radiation for the time of the peak, which warm surface waters and therefore increase water temperature differences between surface and bottom layers. The development of very high vertical water temperature differences was furthermore supported by the weak mixing, as the large surface heating coincided with neap tide and therefore weak tidal mixing.

The positive peaks in ΔT_v in the extreme discharge runs are probably due to the lower temperatures of the discharged river water, compared to the surrounding bay water temperature. The river water has a lower salinity and therefore promotes vertical water column stability which in turn prevents warming of the surface water by vertical mixing with denser but warmer water. The development of vertical salinity gradients is furthermore supported by the low mixing associated with neap tides. The temperature differences are therefore largest for the runs in which the river water is prone to decreasing mixing in its first days in the bay (Figure 16 a and b). In the runs starting at neap tide or between neap and spring tide this effect is not so apparent due to the larger mixing related to the following spring tide (Figure 16 c and d), where cold and fresh river water and warm and saline bay water are mixed more efficiently.

As the river water from the Incomati arrives at the bay's opening first and is usually closer to its north-western part, this is where the larger values of ΔT_v are found first. Later, when the water from the Maputo also reaches the opening, the larger ΔT_v values are found over a larger part of the opening

4.4 Stratification vs Mixing (ϕ)

Results

To represent the extent to which the water column is vertically stratified, the potential energy anomaly was calculated from vertical density variations. Simpson et al. (1990) defined the scalar parameter φ as the work required to bring about complete mixing. A φ close to 0 indicates that the water column is vertically mixed. The higher the φ value, the more stratified the water column is. Please refer to page 51 for a more detailed description of φ.

Figures 26 to 29 show the unfiltered evolution of φ over time along a cross section of the bay's opening, with the *y*-axis representing distance from station CB5, located at the north-western part of the mouth.

The average wet season, dry season (not shown) and no-discharge runs show the same evolution of φ, with values reaching up to ~15 Jm^{-3} if discharge occurs during spring tide and up to 20 Jm^{-3} if discharge occurs at another moment.

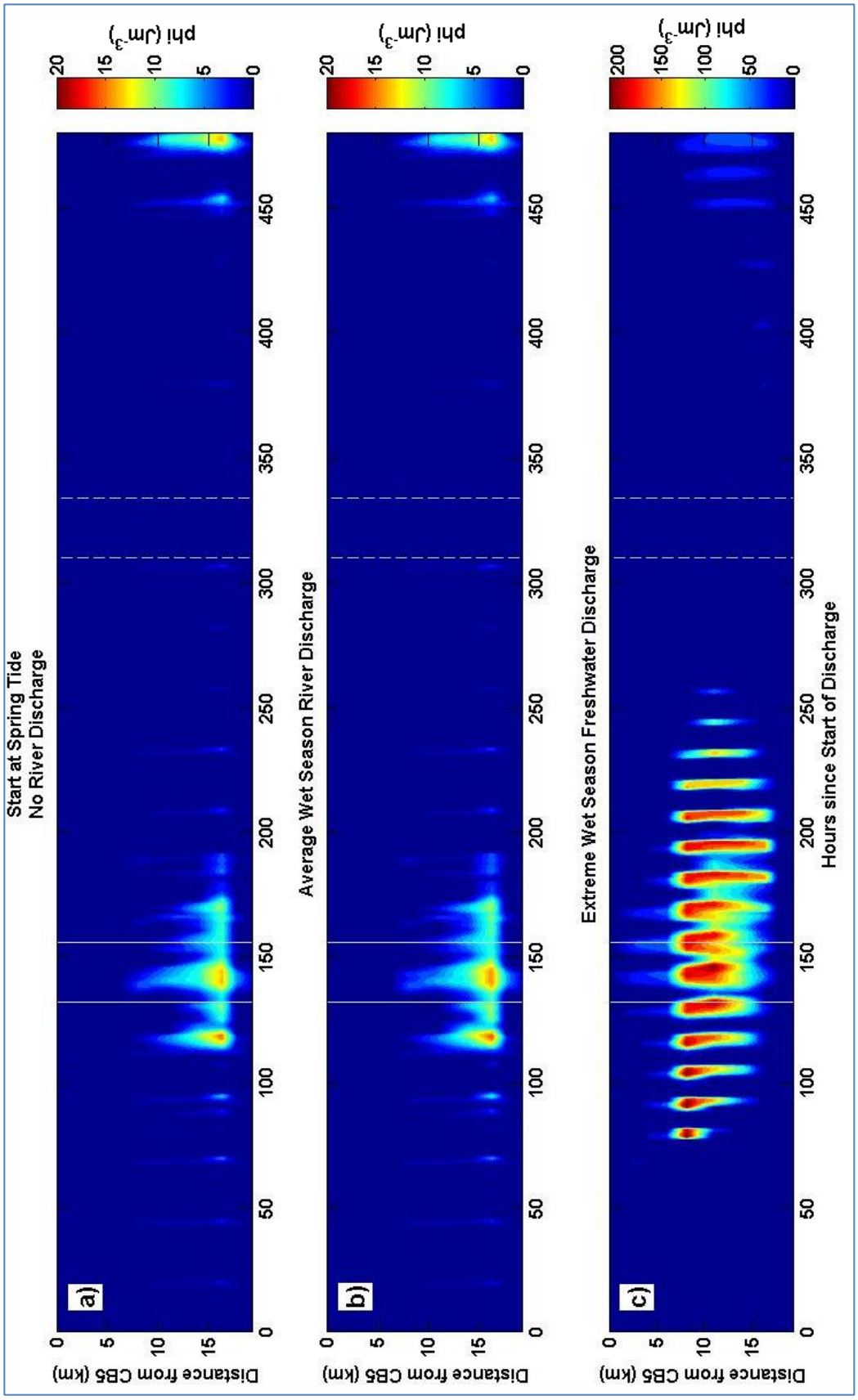

Figure 26: Development of φ over time along Maputo Bay's mouth, for model start during spring tide in dry season with a) no river discharge, b) average wet season discharge and c) extreme wet season discharge. Solid vertical lines indicate time of neap tide, dashed vertical lines indicate time of spring tide

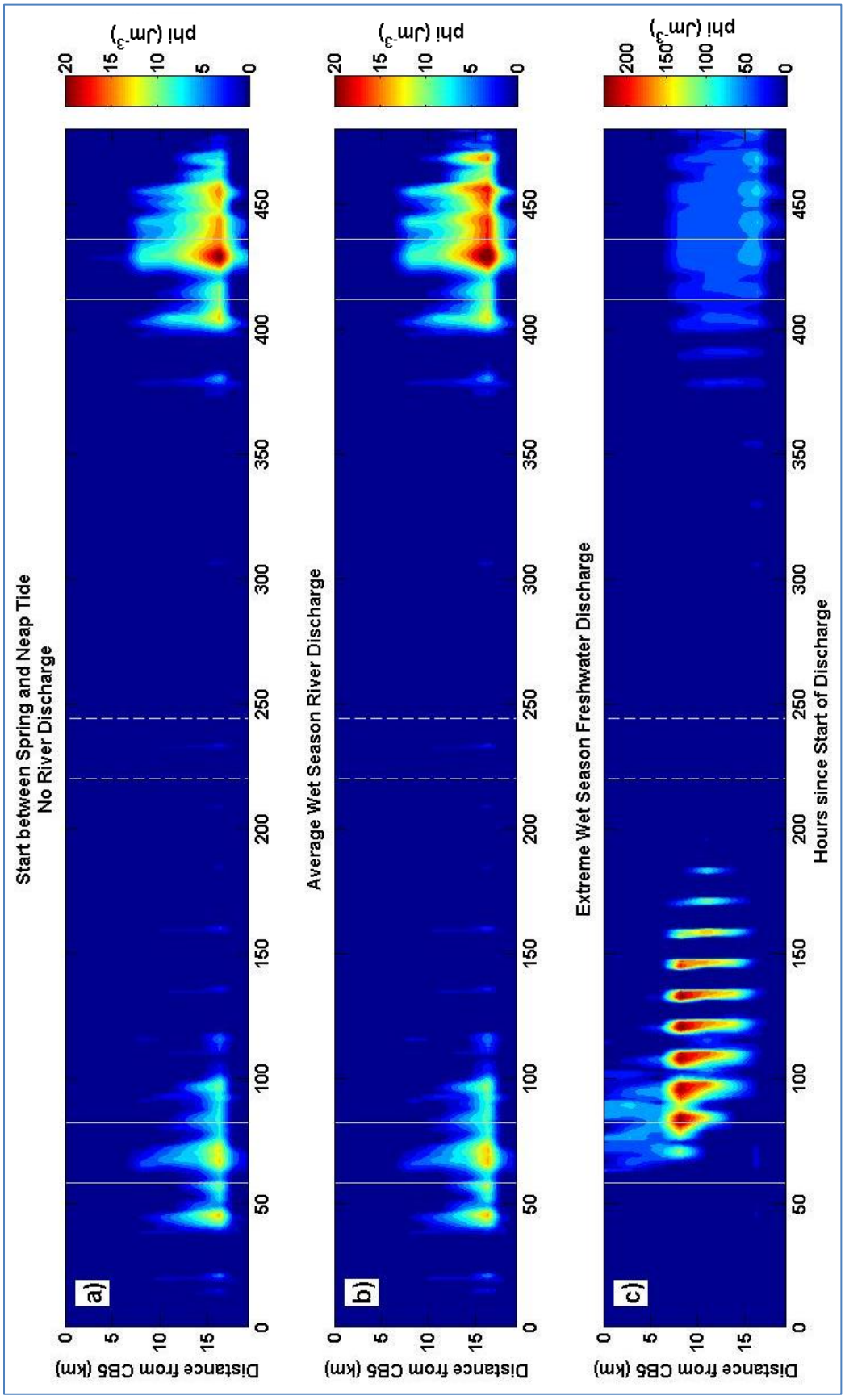

Figure 27: Development of φ over time along Maputo Bay's mouth, for model start between spring and neap tide in dry season with a) no river discharge, b) average wet season discharge and c) extreme wet season discharge. Solid vertical lines indicate time of neap tide, dashed vertical lines indicate time of spring tide.

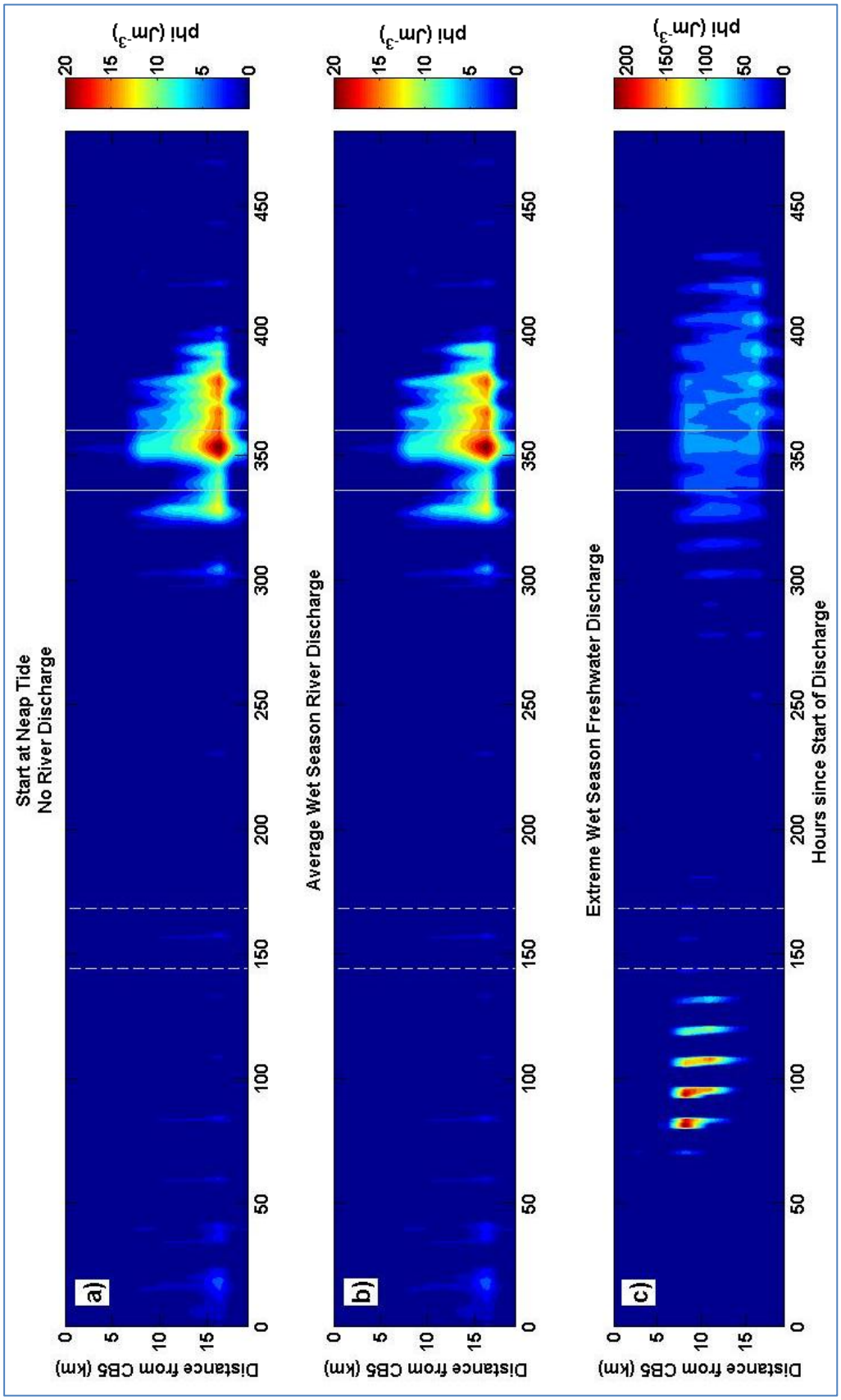

Figure 28: Development of φ over time along Maputo Bay's mouth, for model start during neap tide in dry season with a) no river discharge, b) average wet season discharge and c) extreme wet season discharge. Solid vertical lines indicate time of neap tide, dashed vertical lines indicate time of spring tide.

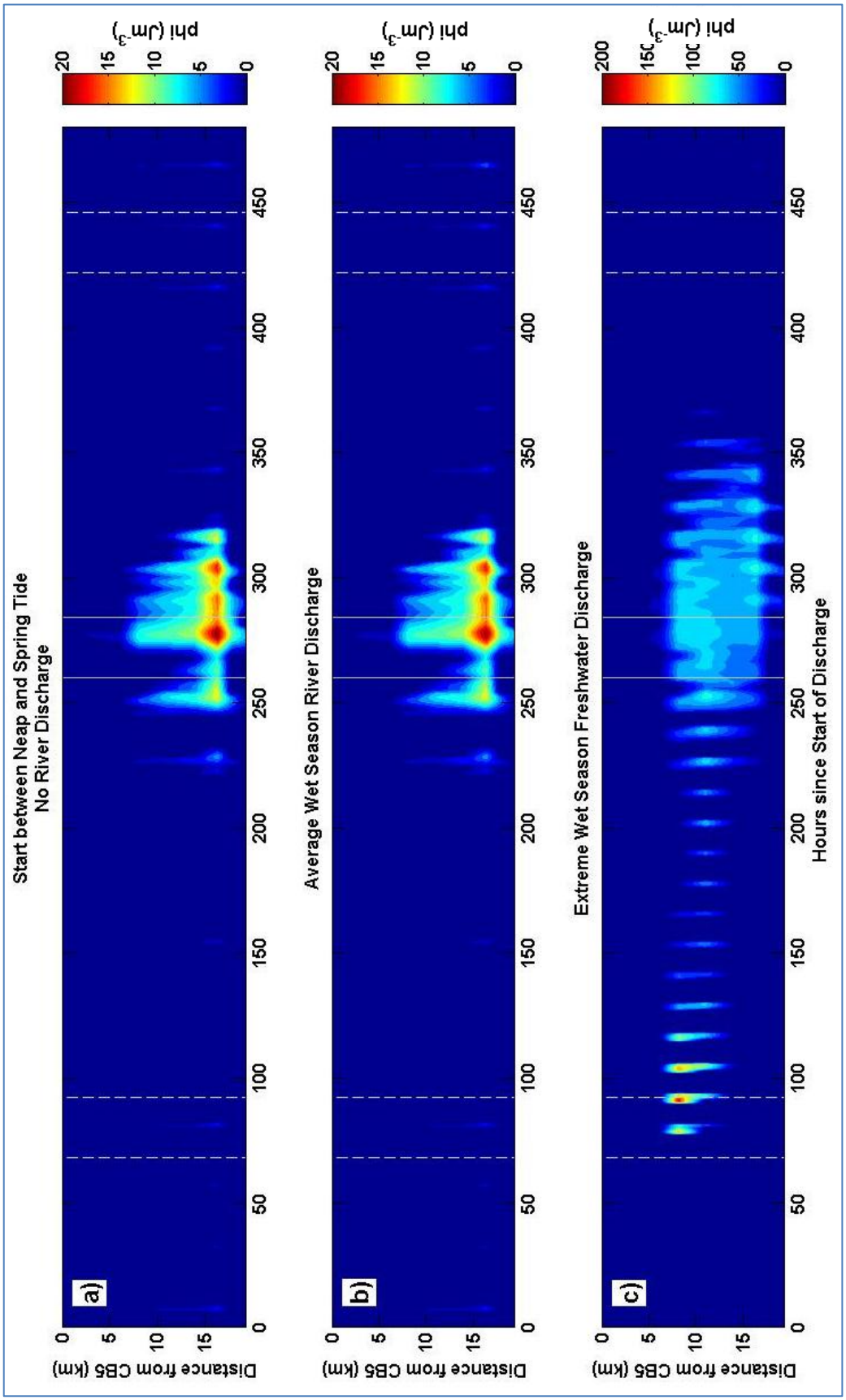

Figure 29: Development of φ over time along Maputo Bay's mouth, for model start between neap and spring tide in dry season with a) no river discharge, b) average wet season discharge and c) extreme wet season discharge. Solid vertical lines indicate time of neap tide, dashed vertical lines indicate time of spring tide

Peaks of φ differ depending on the moment of the start of the model run and occur around 425 hours after model start for the run starting between spring and neap tide (Figure 27 a and b); 350 hours after start of the model run starting during neap tide (Figure 28 a and b) and 275 hours after the start of the model run beginning between neap and spring tide (Figure 29 a and b). The peak therefore occurs always on the same days of the year. In none of the average wet season runs can a significant increase in φ related to the freshwater input be observed. The situation is very different for the model runs with an extreme wet season discharge. There is a clear tidal cycle, with large φ values alternating between being absent and being strongly visible. The first peaks of φ are usually observed approximately 80 hours after the start of the freshwater discharge and arrive slightly earlier if freshwater discharge occurs between spring and neap tide.

The magnitude of φ reaches values as high as 100 Jm^{-3} if the freshwater is introduced between neap and spring tide (Figure 29c), 200 Jm^{-3} if freshwater is introduced at spring or neap tide (Figure 26c and Figure 28c, respectively), and 220 Jm^{-3} if freshwater is introduced between spring and neap tide (Figure 27c).

The temporal extension of the φ peaks varies significantly with the timing of the introduction of freshwater discharge. For discharge at neap tide or between neap and spring tides, peaks are only visible until approximately 130 days after the freshwater discharge (Figure 28c and Figure 29c). For discharge between spring and neap tide, φ peaks are observed until 180 hours after discharge (Figure 27c). The longest influence of the river discharge on the water stratification is found when the discharge is introduced during spring tide (Figure 26c). For this run, the φ peaks can be observed until approximately 245 hours after discharge. The first φ peaks appear at a distance of 8 km from station CB5 at the north-western end of the bay's opening. Later, increased φ values are found over a larger part of the mouth, mainly extending further towards the south-eastern part of the mouth, where water reaches depths of approximately 22 m. The spatial extension over the bay's opening is larger for discharge during spring tide or between spring and neap tide. For these runs, stratification is visible over more than a complete semidiurnal tidal cycle, with φ values above 100 Jm^{-3} found over more than 24 consecutive hours.

Discussion

Taking into account the results of the vertical salinity and water temperature differences, the origins of the varying φ values can be interpreted.

In the model runs without discharge and with average wet season discharge, the variation in φ is not due to the introduction of the freshwater but rather an effect of temperature variations. The φ peaks seem to move from one model run to the other due to the different starting moments of the model runs but represent in fact the same days of the year. The moving φ peaks for the model runs without discharge or with average discharge correspond to the same moments in time as the vertical temperature differences for these runs. In the no-discharge and average discharge runs, the higher φ values can therefore be attributed to the heating of surface waters, coinciding with low mixing of neap tide, leading to a more stratified water column. Salinities did not show significant variations and are therefore assumed not to influence φ greatly.

For the extreme discharge runs, on the other hand, very large salinity variations were found, with the surface layer showing salinities of up to 30 units below bottom salinities. At the moments of

these large differences, φ values are also very large. The freshwater floating on top of the more saline bay water has therefore lead to the high φ values observed in the extreme discharge runs. Both, vertical salinity differences as well as φ peaks were significantly larger when discharge was introduced at spring tide or between spring and neap tide. This can be explained by the amount of mixing that the freshwater plume is subject to after arriving in the bay. When the discharge is introduced to the bay during spring tide or between spring and neap tide, it will not be mixed very strongly until the following spring tide. If, on the other hand, the discharge is introduced at neap tide or between neap and spring tide, the following spring tide will act on the river plume shortly after entering the bay. The spring tide, characterized by a much larger tidal range, mixes the water column much more efficiently, mixing the fresh river water down into deeper layers. Vertical salinity differences are therefore smaller, which also mean less intense stratification and therefore smaller values for φ.

For the runs of an extreme discharge between spring and neap tide, both, vertical salinity and water temperature differences coincided with the peaks in stratification around 300 hours after the start of the simulation. An estimate was made on the contributions of salinity and water temperature in influencing φ for a location of 13 m depth, characterised by a φ of approximately 70 Jm^{-3} at a moment 290 hours after start of the simulation. This analysis has shown that approximately 90% of the stratification here is due to vertical salinity differences while the remaining 10% of stratification are induced by vertically differing temperatures.

Summarising, the potential energy anomaly φ was influenced mainly by vertical temperature gradients for the runs with no, very little or average freshwater discharge, while the vertical salinity gradients had a larger influence on the potential energy in the runs with extreme discharge.

4.5 Stratification for Different Ratios of Incomati and Maputo Freshwater Discharge

Results

To find out how the rivers Maputo and Incomati influence the stratification of the bay, an analysis of φ along the cross-section of the mouth was conducted with varying discharge ratios. Figure 30 shows the variation of φ for extreme discharge, introduced during spring tide, with subplot a) showing the 3:2 ratio, subplot b) showing the 1:4 ratio and subplot c) showing the 4:1 ratio. From the figures it becomes clear that if the discharge of the Incomati is larger than the discharge of the Maputo, the φ peaks can be seen earlier (approximately after70 hours, Figure 30c) than when the discharge of the Maputo is larger (approximately 140 hours, Figure 30b). Figure 31: Development of φ over time along Maputo Bay's mouth, for model start during neap tide and extreme river discharge with varying Incomati : Maputo river discharge ratios during dry seasonFigure 31 is similar but for a model run starting at neap tide.

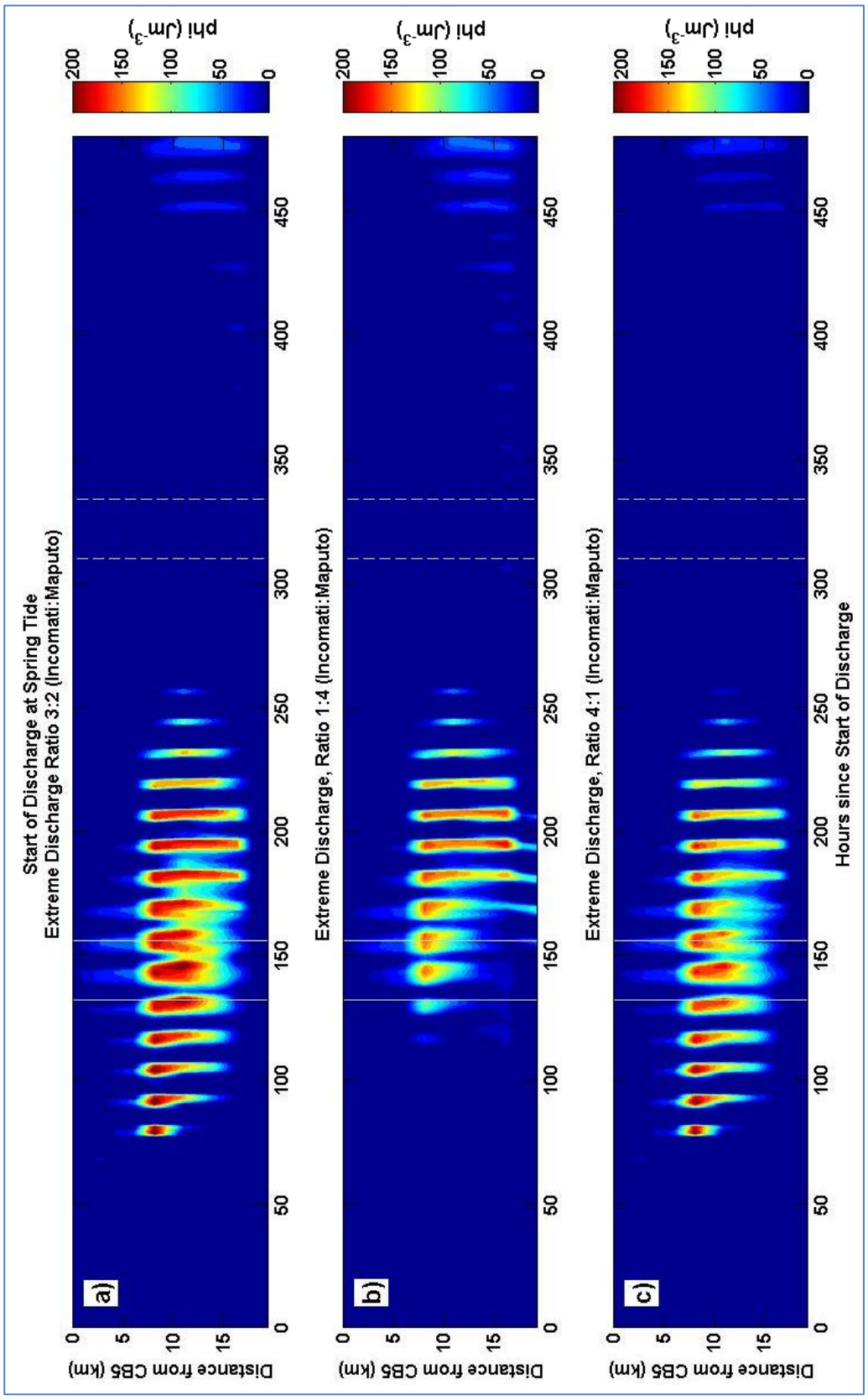

Figure 30: Development of φ over time along Maputo Bay's mouth, for model start during spring tide and extreme river discharge with varying Incomati : Maputo river discharge ratios during dry season: a) 3:2 ; b) 1:4; c) 4:1. Solid vertical lines indicate time of neap tide, dashed vertical lines indicate time of spring tide.

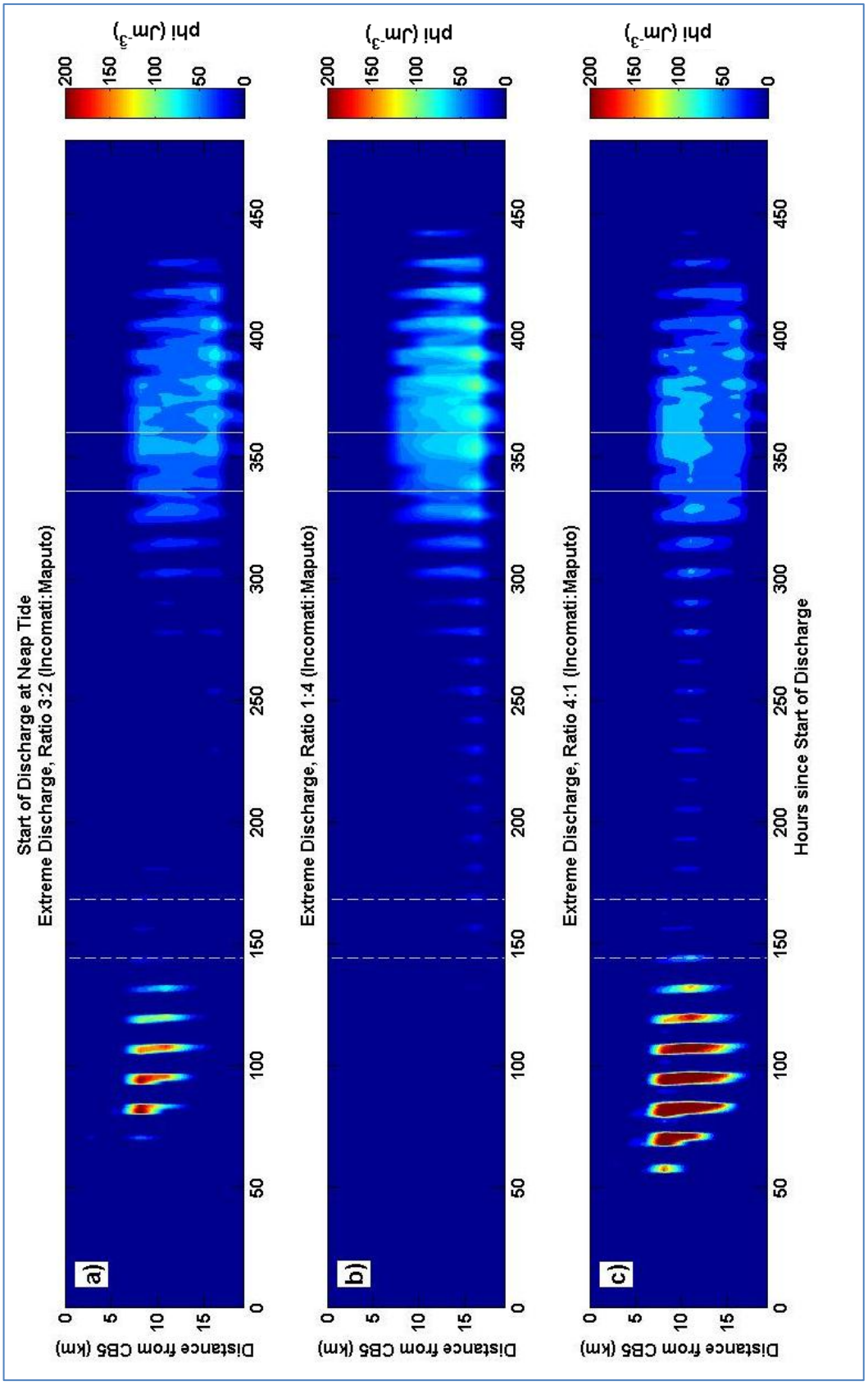

Figure 31: Development of φ over time along Maputo Bay's mouth, for model start during neap tide and extreme river discharge with varying Incomati : Maputo river discharge ratios during dry season: a) 3:2; b) 1:4; c) 4:1. Solid vertical lines indicate time of neap tide, dashed vertical lines indicate time of spring tide.

The maximum cross-bay-opening extension of significantly increased φ values is larger when the influence of the Maputo is larger. Overall, φ shows the largest values for the realistic 3:2 discharge ratio (Figure 30a). Figure 31 is similar but for discharge at neap tide. In this case, the largest values of φ (>200 Jm^{-3} can be found for a stronger Incomati discharge. If the Maputo discharge is stronger, the earlier φ peak is absent. The second, smaller φ peak which was also present in the runs without discharge is slightly increased (approximately 100 Jm^{-3}) for the ratio 1:4, in which the Maputo has a larger discharge (Figure 31b).

Summarising, a comparably larger discharge of the Incomati leads to an earlier arrival of φ peaks. The extent of the φ peaks over the mouth depends on the timing of freshwater discharge. If discharge occurs during spring tide, the largest extent will be found for a 3:2 ratio. If, on the other hand, discharge occurs during neap tide, the largest extent occurs for a 4:1 ratio with the Incomati being relatively more important.

Discussion

These results confirm the previous assumption that the first arrival of high φ values around 6-8 km away from the north-western part of the bay's opening are due to the arrival of the freshwater plume from the Incomati. It can also be confirmed that the later and further extension over the opening of large φ values can be explained by a combination of horizontal mixing of the freshwater plumes as well as the arrival of the Maputo river plume. The φ development can therefore be explained by the locations of the river mouths in the bay. While the Incomati River mouth is located close to the north-western part of the bay's opening, the Maputo River mouth is located in the southern part of the bay. The Incomati River discharge therefore reaches the bay opening much earlier than the Maputo discharge. At the same time does the Maputo freshwater, on its way out of the bay, mix more with surrounding bay water, before reaching the opening. This can explain the relatively lower values of φ when the influence of the Maputo is larger, as well as the further extension towards the south-eastern part of the opening.

Stratification was especially strong when a large discharge of the Incomati was introduced during neap tide. In this case, the Incomati discharge, entering the bay very close to it's opening, was undergoing very little mixing on its short way to the bay's opening. The large φ values were therefore a result of the combination of small tidal energies mixing the river and bay water very little and the location of the river mouth close to the bay opening.

4.6 Residual velocities

Results

Residual velocities, filtering out tidal currents, were calculated over a cross-section of the bay's opening, with positive values indicating a flow directed out of the bay and negative values indicating a flow into the bay. The results can be seen in Figures 32 to 35.

Five different moments in time were chosen, for which the velocity cross sections are presented, both for runs without discharge and with extreme discharge:

- 72 hours after the start of the model run and the beginning of discharge of the river water;
- At the moment of the first significant φ peaks in the extreme runs;
- At the moment of the largest spatial extension of φ peaks in the extreme runs, indicating a moment of a large spatial extension of stratification across the bay's opening;
- During spring tide;
- During neap tide.

As the moments of the first significant and the largest extension of φ vary depending on the moment of discharge, the exact times (in hours) for which the cross sections are represented also vary.

The left panels show runs without discharge and the right panels show runs with an extreme wet season discharge.

The runs with no discharge show generally a circulation pattern of vertical cells during spring tide, with an inflow in the north-western part of the bay opening as well as over the deepest part of the opening (around 2 cms^{-1}) and an outflow approximately 8 km away from station CB5 (usually 5-7 cms^{-1}). During neap tide, the velocities are generally small and often a surface inflow over the deeper part of the bay's opening can be observed.

The runs with an extreme discharge generally show larger velocities, especially in the first three time steps, representing the conditions after 72 hours as well as during the first signs of stratification and the largest spatial extent of stratification over the bay's opening. Here, the flow is always represented by surface velocities in the north-western part of the opening being directed outwards and reaching approximately 8 cms^{-1}. During spring tide, velocity patterns are similar to the no-discharge runs, with an inflow in the north-western part of the opening and over the deeper parts and an outflow approximately 8 km away from station CB5 (~ 8 cms^{-1}). Even though the patterns are very similar, velocities are larger for the runs with an extreme discharge than for those without discharge. During neap tide, flow patterns of the extreme discharge runs are very different from the no-discharge runs. Here, a classical estuarine circulation pattern can be observed, with two horizontal flow cells: surface layers show large velocities directed out of the bay, while bottom layers indicate an inward flow.

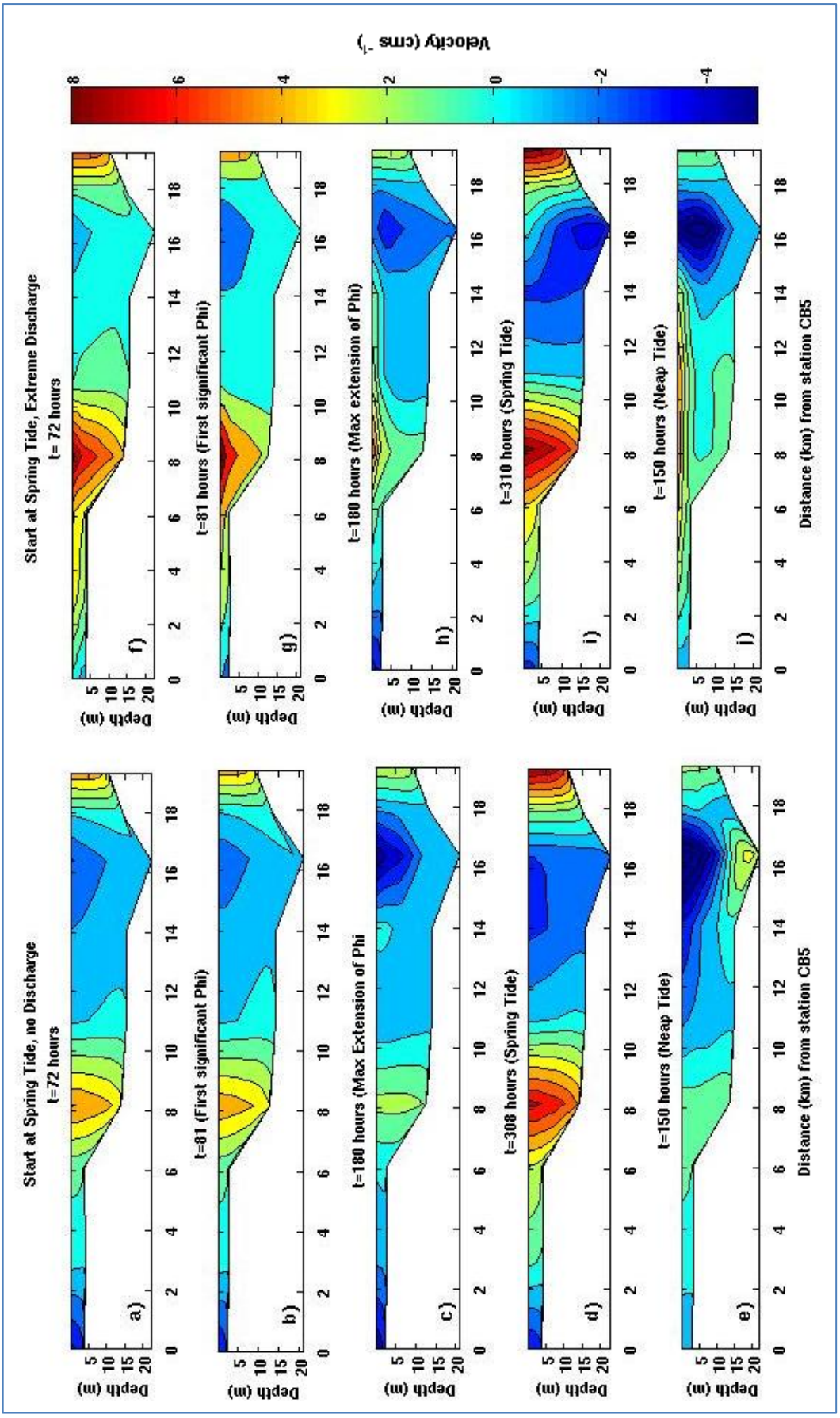

Figure 32: Residual velocities for dry season model runs starting at spring tide. Positive velocities indicate flow out of the bay, negative velocities represent flow into the bay. The left column shows model runs without discharge, the right column shows runs with extreme discharge.

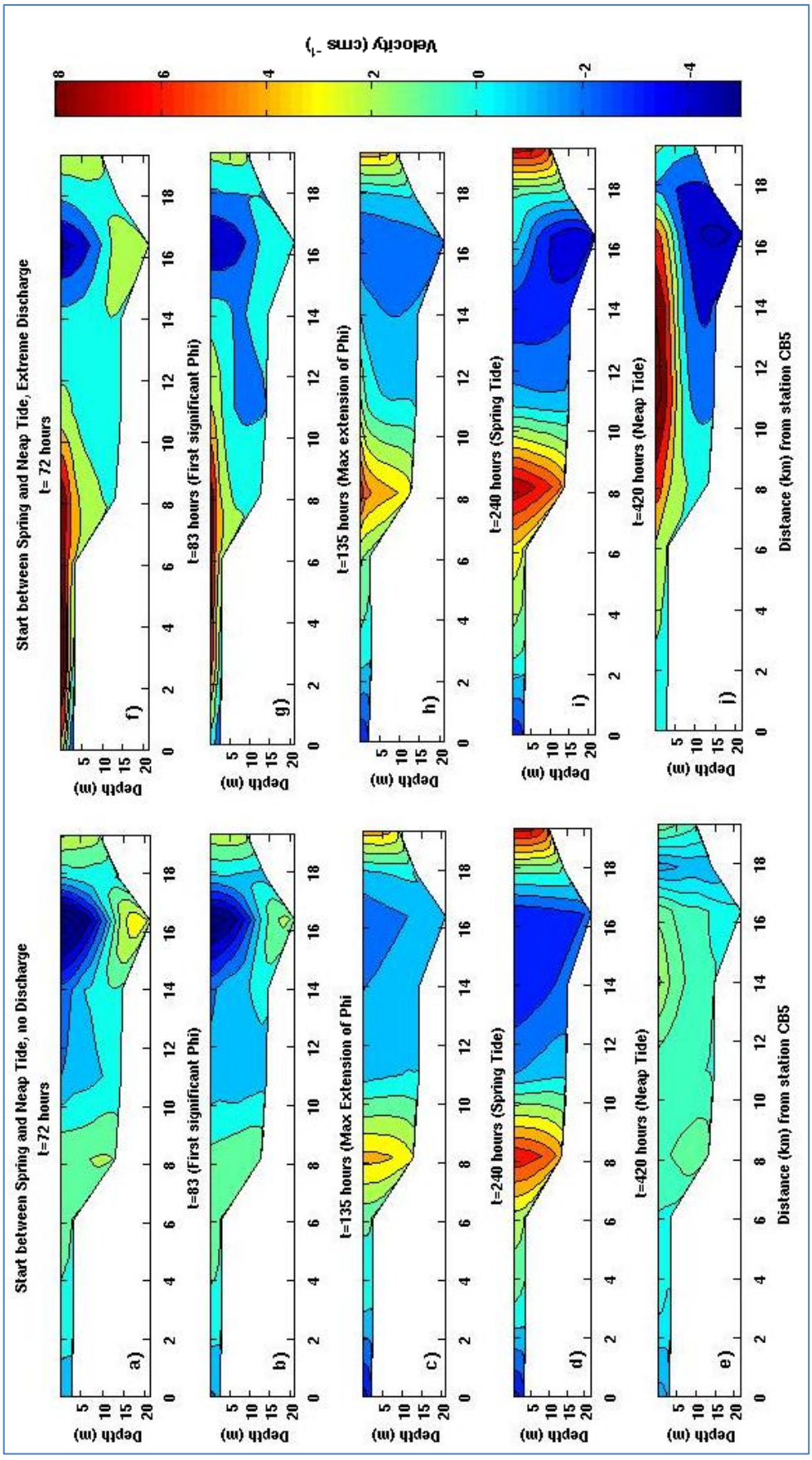

Figure 33: Residual velocities for dry season model runs starting between spring and neap tide. Positive velocities indicate flow out of the bay, negative velocities represent flow into the bay. The left column shows model runs without discharge, the right column shows runs with extreme discharge.

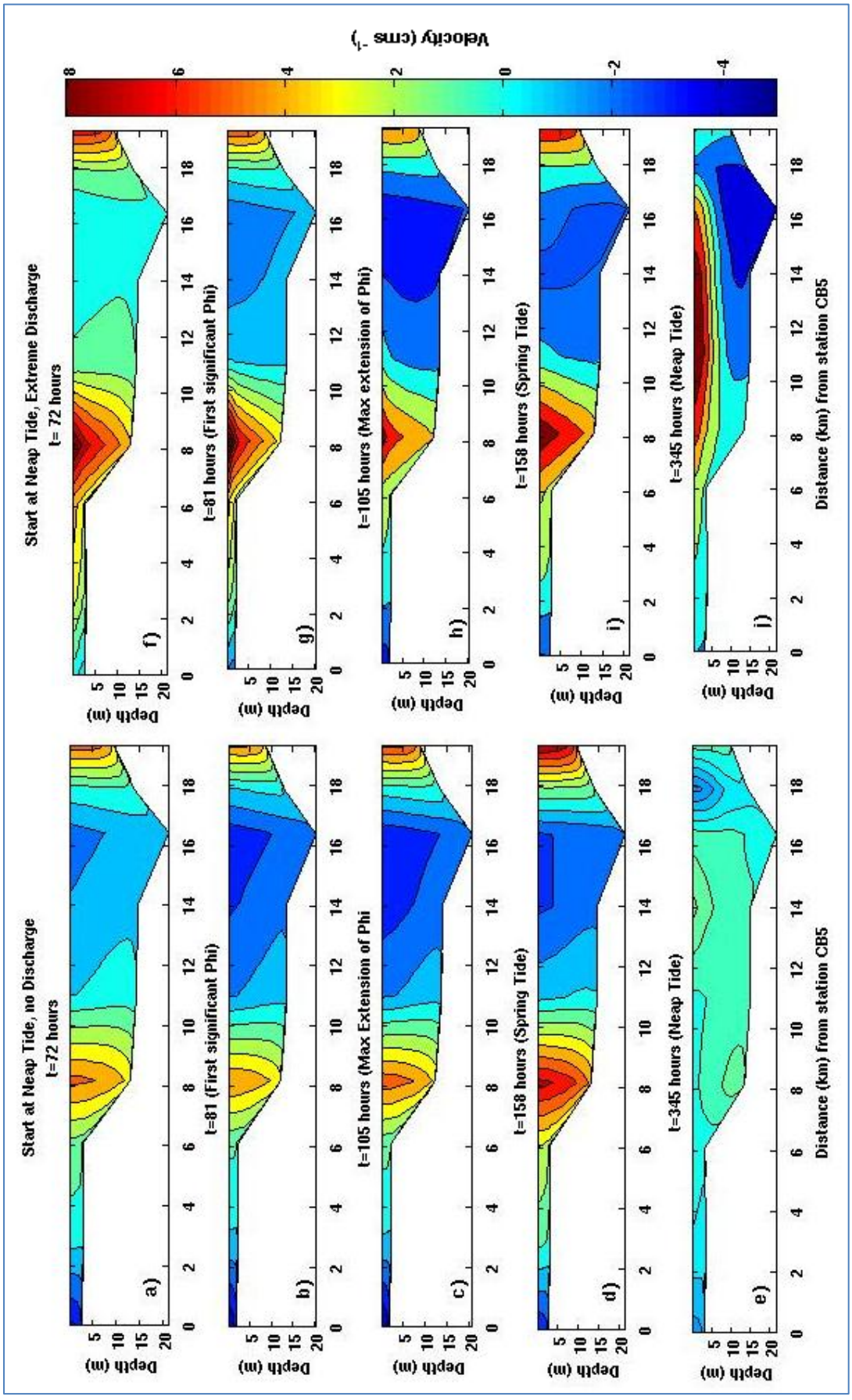

Figure 34: Residual velocities for dry season model runs starting at neap tide. Positive velocities indicate flow out of the bay, negative velocities represent flow into the bay. The left column shows model runs without discharge, the right column shows runs with extreme discharge.

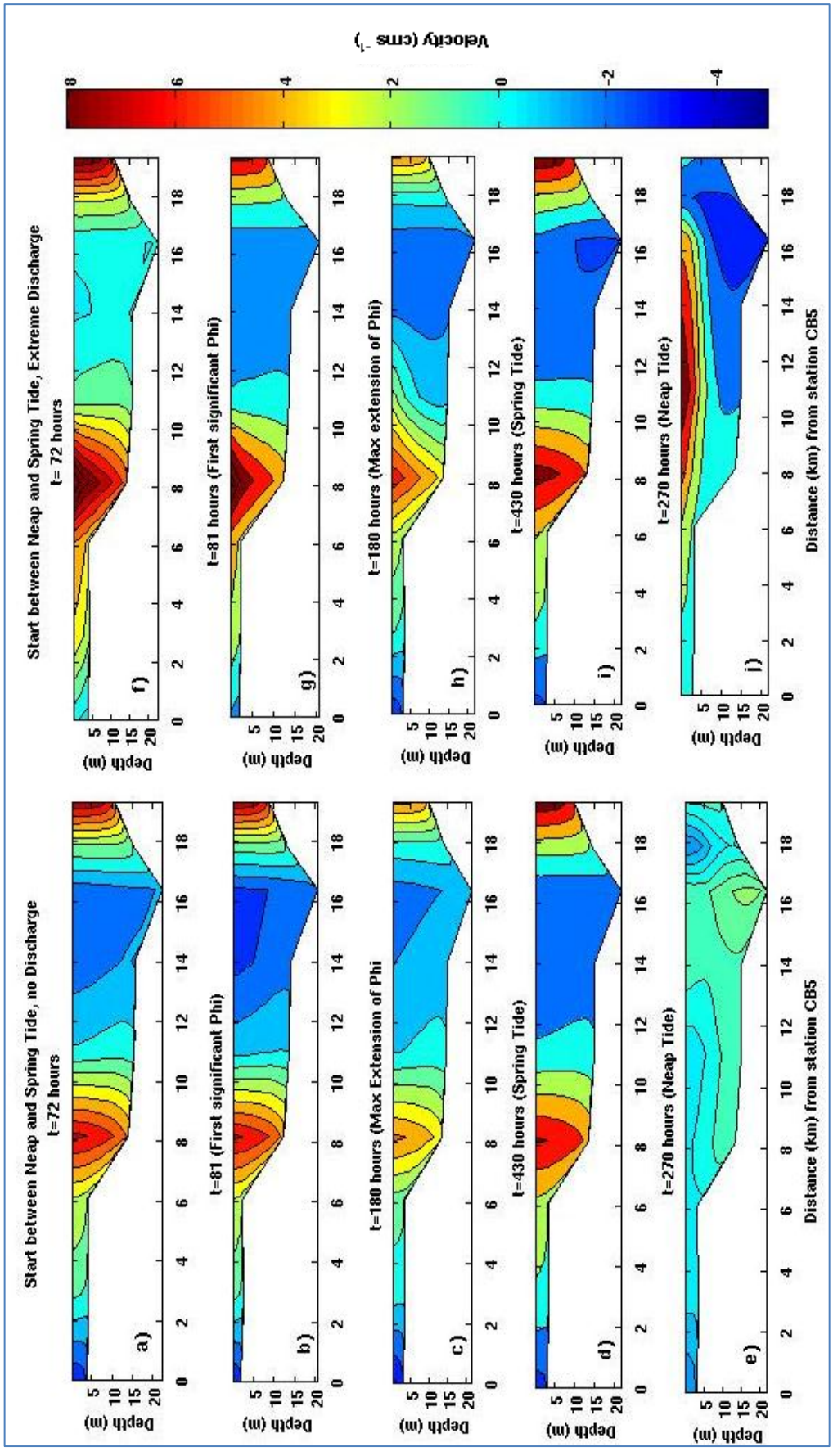

Figure 35: Residual velocities for dry season model runs starting between neap and spring tide. Positive velocities indicate flow out of the bay, negative velocities represent flow into the bay. The left column shows model runs without discharge, the right column shows runs with extreme discharge.

Discussion

The residual currents display a general pattern of inflow through the deep channel and outflow over the more shallow banks. This is typical for subtropical estuaries where the tide is rather a standing wave than progressive. Lencart e Silva (2007) suggested that the tide in Maputo Bay is mixed but closer to a standing wave. Valle-Levinson et al. (2009) investigated the residual circulation in four subtropical estuaries which are characterised by a shorter bay and narrower mouths than Maputo Bay. The tidal waves in the bays were either standing waves or near-standing waves. Valle-Levinson et al. (2009) reached similar conclusions to those found here, with the residual circulations across the bay openings generally being characterised by an inflow in the channel and an outflow over the shallower shoals. The varying bathymetry of the channel acts on the tidal wave and a pair of gyres develops, forcing an inflow through the deep channel and outflows over the banks. The residual flow patterns are therefore mainly forced by tidal stresses and residual elevation slopes, while the Stokes transport is considered negligible in the case of a standing wave (Valle-Levinson et al., 2009). Further research would be needed to determine whether the Stokes effect is in fact negligible in Maputo Bay or has to be taken into account due to the influence of the progressive wave component in Maputo Bay's tidal regime.

The larger out-ward surface velocities can be explained by the density currents related to the fresher river water introduced to the bay. The flow is focused more in the surface for runs which are less prone to mixing from spring tide. Where the river plume is influenced by strong mixing shortly after entering the bay, such as in the run starting between spring and neap tide, the outward velocities can be found over the complete depth of the bay's opening.

During spring tide, the velocity patterns of no-discharge runs and extreme discharge runs are comparable, even though velocity magnitudes are larger for the extreme discharge runs. This is in accordance with Lencart e Silva (2007), who found that during spring tide the dry season and wet season flow patterns are similar, being comprised of an outflow over the whole depth of the deep channel and inflows over the complete depths of the more shallow parts in the Northwest. During neap tide, on the other hand, a classical estuarine circulation is found for the extreme discharge run, with surface waters flowing out and deeper water layers flowing into the bay. It is assumed that this estuarine circulation can develop due to the decreased mixing force of the tide during neap tide. As the tidal magnitudes are much smaller than during spring tide, less mixing is induced and the fresh river water floats on top of the saline bay water. A density current develops, with the fresher water flowing out at the surface, compensated by an inflow of shelf water in the deeper layers. Due to the lack of freshwater in the no-discharge runs, this pattern is not found in the left columns of the previous figures. In this case, buoyancy is not induced through freshwater but only through surface heating, which acts on the whole water surface and was not able to create significant residual velocities.

For discharge during neap tide or between spring and neap tide, the residual currents for the extreme discharge runs show an estuarine-type circulation with large velocities. This is due to the potential energy anomaly in the system as the plume had been arrested during the previous spring tide. With the weakening tidal stirring, strong density currents developed, exporting buoyancy out of the bay during neap tide. In the runs without discharge, the potential energy anomaly in the system was much smaller, leading to very small residual currents during neap tide.

4.7 Flushing Times

Results

To investigate the flushing times in Maputo Bay under varying discharge conditions, a number of realistic model runs were undertaken, varying between a typical dry season discharge, an average wet season discharge and an extreme wet season discharge, all induced over 3 consecutive days. An artificial, conservative tracer was introduced evenly over the bay in all depths with a concentration of 1 kgm^{-3}. The tracer was introduced at the start of the discharge. For each discharge, four model runs were undertaken, introducing the discharge and tracer during different moments in the tidal cycle, to investigate whether the timing of the arrival of the freshwater plume has an effect on flushing times.

The results for the model runs without freshwater discharge and with a dry season discharge were very similar. Therefore, the dry season discharge runs will not be visually represented in this chapter.

Figure 36 shows the temporal development of the bay-average tracer concentrations over the same area the tracer was introduced in. The tracer concentration was filtered applying a pl33 filter to exclude the tidal signal. Due to the application of the filter, the first and last 33 hours of data should not be taken into account. The figures therefore only show tracer concentrations for a limited time span.

Generally, the figures clearly show that tracer concentration dropped strongest when the extreme wet season discharge was applied and least when no discharge was used. 420 hours after the discharge and tracer were introduced to the model, tracer concentrations for the extreme discharge had dropped to ~69-72% of the initial concentration. For the average wet season discharge and the no discharge runs, concentrations had dropped to ~77-82% and ~80-84%, respectively. The average and no discharge runs generally showed the same patterns of concentration development, with magnitudes of concentration decreases being larger in the average runs. Within the first 3 days, concentrations of the average run had dropped by 7-9% while concentrations in the no-discharge run had only dropped by 4-7%. Halfway from spring to neap tide as well as during neap tide, concentrations only showed very small decreases, almost plateauing at constant concentrations. An exception was the model run with discharge during spring tide (Figure 36a), where a significant decrease in concentration was observed during neap tide. Significant concentration decreases were mainly found in the transition from neap to spring tide as well as during spring tide. For both types of discharge, after 17 days of running the model, the concentration was smaller if freshwater discharge occurred at spring tide and largest if discharge occurred between spring and neap tide or during neap tide.

The extreme discharge runs showed a large decrease of concentration in the first 3 days. By then, concentrations for all extreme discharge runs had dropped by 13-14%, with concentrations having been slightly larger when discharge was introduced during spring tide or in the transition from neap to spring tide. Independent on when discharge was introduced, largest decreases in concentration occurred during neap tide. During spring tide, concentrations decreased, even though the decrease was less pronounced than just after neap tide.

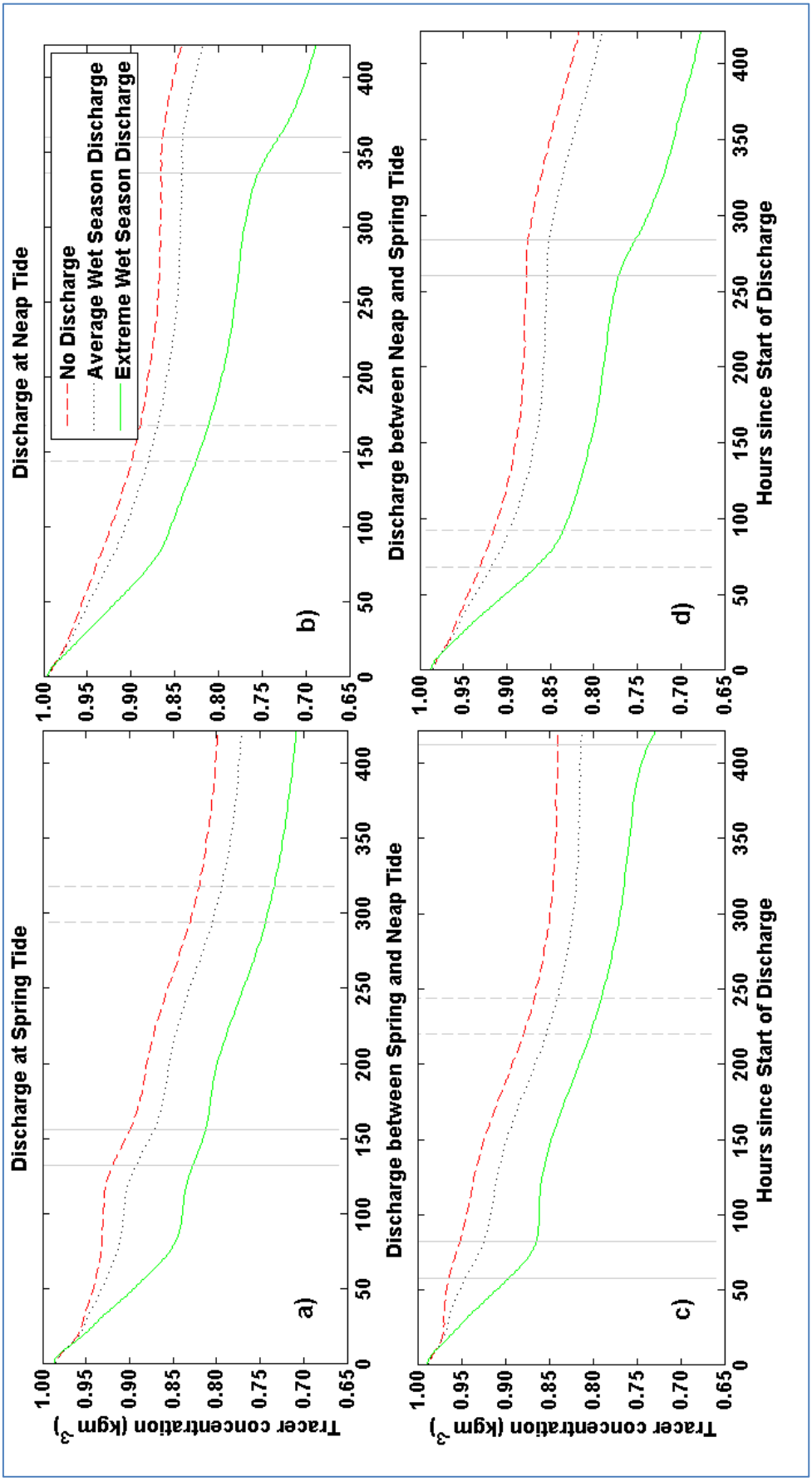

Figure 36: Development of tidally-filtered tracer concentration during dry season, for model start and discharge at a) spring tide, b) neap tide, c) between spring and neap tide and d) between neap and spring tide. Red dashed line shows runs without river discharge, black dotted line shows runs with average wet season discharge and green line shows runs with extreme river discharge. Solid vertical lines indicate time of neap tide, dashed vertical lines indicate time of spring tide.

Summarising, if no freshwater or an average amount of freshwater is introduced, concentration changes are generally smaller, especially around neap tide. If a larger amount of freshwater is introduced, concentrations decrease faster and no plateau in bay-average tracer concentrations can be found during neap tide. Instead, tracer concentrations decrease significantly.

To determine whether the two significant rivers, Incomati and Maputo, have different effects on flushing times, a set of model runs with differing Incomati:Maputo discharge ratios was undertaken. The ratio used for the basic runs (Figure 36) was 3:2, which is approximately in accordance with the ratio usually observed. Additional ratios were: 4:1 and 1:4 (freshwater discharge Incomati : freshwater discharge Maputo). The developments of tracer concentrations for these runs, using average and extreme discharge conditions and introducing the discharge either during spring or during neap tide, can be seen in Figure 37. The Figures show that if the average discharge is applied, differences between various discharge ratios are very small. If the extreme discharge is applied, the concentrations decrease more if the discharge of the Maputo is increased (1:4 ratio) and less if the discharge of the Incomati is increased (4:1).

Flushing times were calculated from the tracer concentrations and are shown in Figure 38.

Subfigures a), b), c) and d) of Figure 38 show flushing times for the no-discharge runs. These generally show peaks of 600-800 days, with peaks occurring just before neap tide. This peak was not visible for the run starting at spring tide (subplot a)). Minimum values are approximately 80 days, found in the days around spring tide.

Subfigures e), f), g) and h) show the runs with an average wet season discharge. Maximum flushing times of 500-600 days are found before neap tide. This peak was not found for the run starting at spring tide (subplot e)). Minimum flushing times of approximately 70 days are found in the days around spring tide.

Subfigures i), j), k) and l) show extreme wet season discharge runs, which showed significantly lower flushing times. Maximum values of 140 days occurred in the transition from spring to neap tide for model runs when discharge was introduced between spring and neap tide (Figure 38j). For discharge during neap tide (Figure 38k) or between neap and spring tide (Figure 38l)), maximum flushing times were ~125 days. Minimum flushing times were found in the transition from neap to spring tide, with values as low as 40 days if discharge occurred during neap tide (Figure 38k), and 50 days if discharge was introduced at a different moment of the spring-neap cycle.

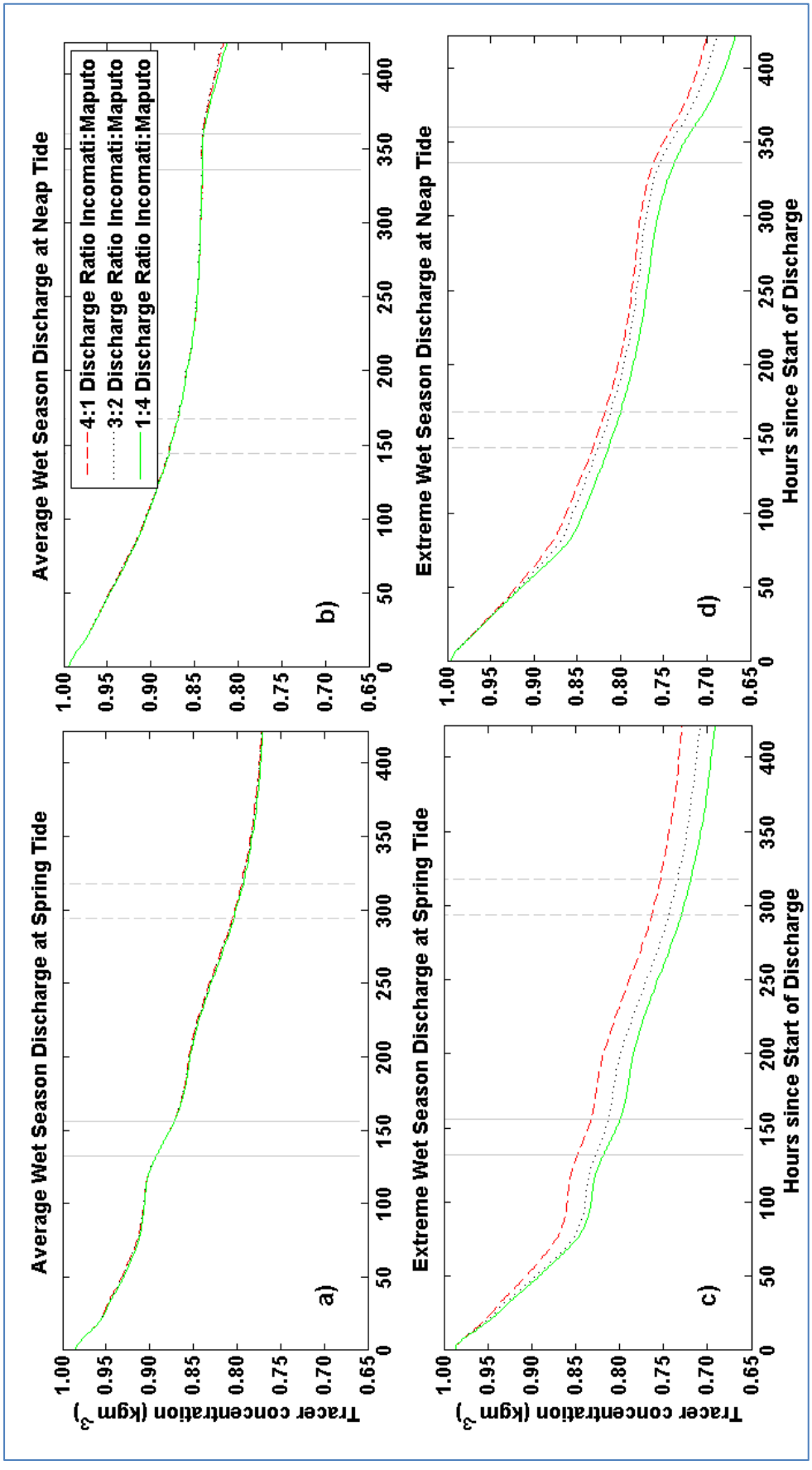

Figure 37: Development of tidally-filtered tracer concentration for varying discharge ratios during dry season, for a) average wet season discharge at spring tide, b) average wet season discharge at neap tide, c) extreme discharge at spring tide and d) extreme discharge at spring tide. Varying Incomati : Maputo discharge ratios, with the red dashed line indicating a ratio of 4:1, the black dotted line a ratio of 3:2 (same as in previous figure) and the green line indicating a ratio of 1:4. Solid vertical lines indicate time of neap tide, dashed vertical lines indicate time of spring tide.

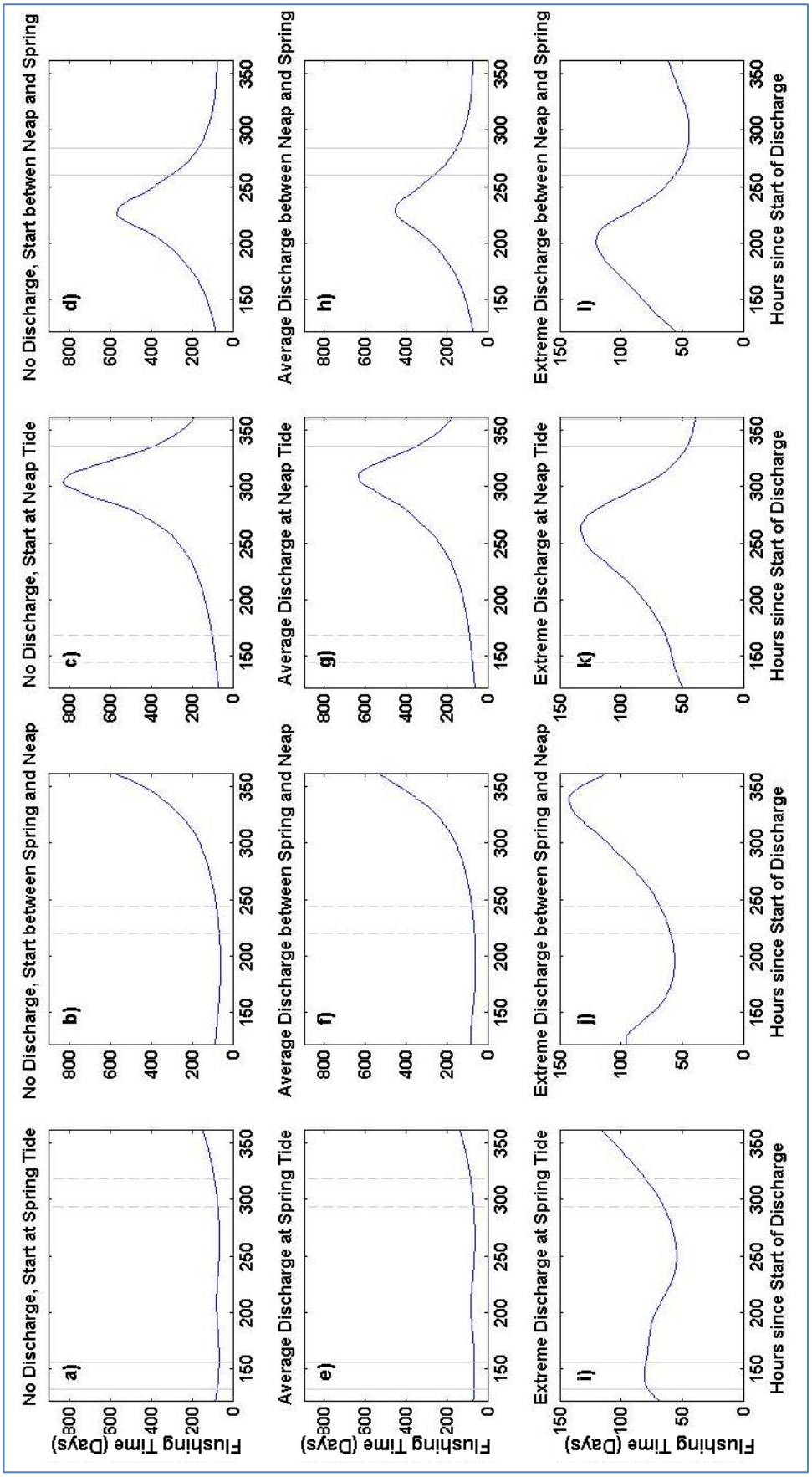

Figure 38: Development of dry season flushing time for 5-day moving windows for several runs: no discharge: a) start at spring tide, b) start between spring and neap tide, c) start at neap tide, d) start between spring and neap tide; average wet season discharge: e) start at spring tide, f) start between spring and neap tide, g) start at neap tide, h) start between spring and neap tide; i) extreme discharge: start at spring tide, j) start between spring and neap tide, k) start at neap tide, l) start between spring and neap tide. Solid vertical lines indicate time of neap tide, dashed vertical lines indicate time of spring tide.

Figure 39 shows flushing times for varying Incomati : Maputo discharge ratios. Figure 39 a) and b) show the runs with an average wet season discharge.

When an average discharge is introduced, varying the discharge ratio between Incomati and Maputo river discharge has little effect on flushing times, apart from just before neap tide in the runs where discharge was introduced during neap tide (subplot b)). Here, a larger discharge of the Incomati has lead to larger peaks in flushing time.

Figure 39 c) and d) show the runs with an extreme wet season discharge. Here, flushing times vary more with discharge ratio. For a discharge during spring tide, flushing times are smaller if the discharge of the Maputo is larger, apart from a moment in the transition between neap and spring tide (around day 200), when all ratios show very similar flushing times. For a discharge during neap tide, flushing times for all discharge ratios are similar around spring tide. Between spring and neap tide, flushing times are much smaller (20 days) for a larger Maputo discharge. Towards neap tide, the difference in flushing times has decreased but is still visible, with flushing times still being slightly smaller for a larger Maputo discharge. Overall, for the runs with an extreme discharge, a decreasing importance of the Incomati and an increasing importance of the Maputo River leads to an overall decrease in flushing times.

Discussion

The results showed that overall flushing times decrease with river discharge. This is due to the river water flushing out the bay water as it is an added forcing mechanism in the system. Where very little or no freshwater is introduced, this forcing is very weak or absent.

In the model runs with smaller river discharge, flushing times are smallest around spring tide. This is due to the large in- and outflows due to the tidal motions, transporting some of the bay water out of the bay during each tidal excursion. This advection is more efficient during spring tide than during neap tide, as neap tide velocities are much smaller. What was surprising was the peaks of flushing times for the runs without discharge not occurring during neap tide but approximately 40 hours earlier. This earlier peak can not be explained by tidal forcing, as the peak should occur during neap tide when no freshwater is present. However, the increased values of φ found at around neap tide in the runs with no discharge, dry season discharge and average wet season discharge, might play a role. As suggested in Chapter 4.4, these increased φ values may be due to surface heating that occurred in the given days. It is possible that this surface heating of the bay, inducing stratification, lead to flushing times decreasing, so that maximum flushing times occurred before the surface heating during neap tide. Model runs with dry season discharge and average wet season discharge showed flushing time patterns similar to the flushing times for the no-discharge run, suggesting that the freshwater input was not large enough to trigger significant classical estuarine circulation. A particularity in the results that remains is the larger flushing time peak for the no-discharge run starting at neap tide. This peak is around 200 days larger than the peaks for the no-discharge runs starting in different moments of the tidal cycle. Further research will be needed to explain this difference, which can also be found for the average discharge runs. The runs with little or no discharge, starting at spring tide, showed small flushing times over the complete duration of the model run.

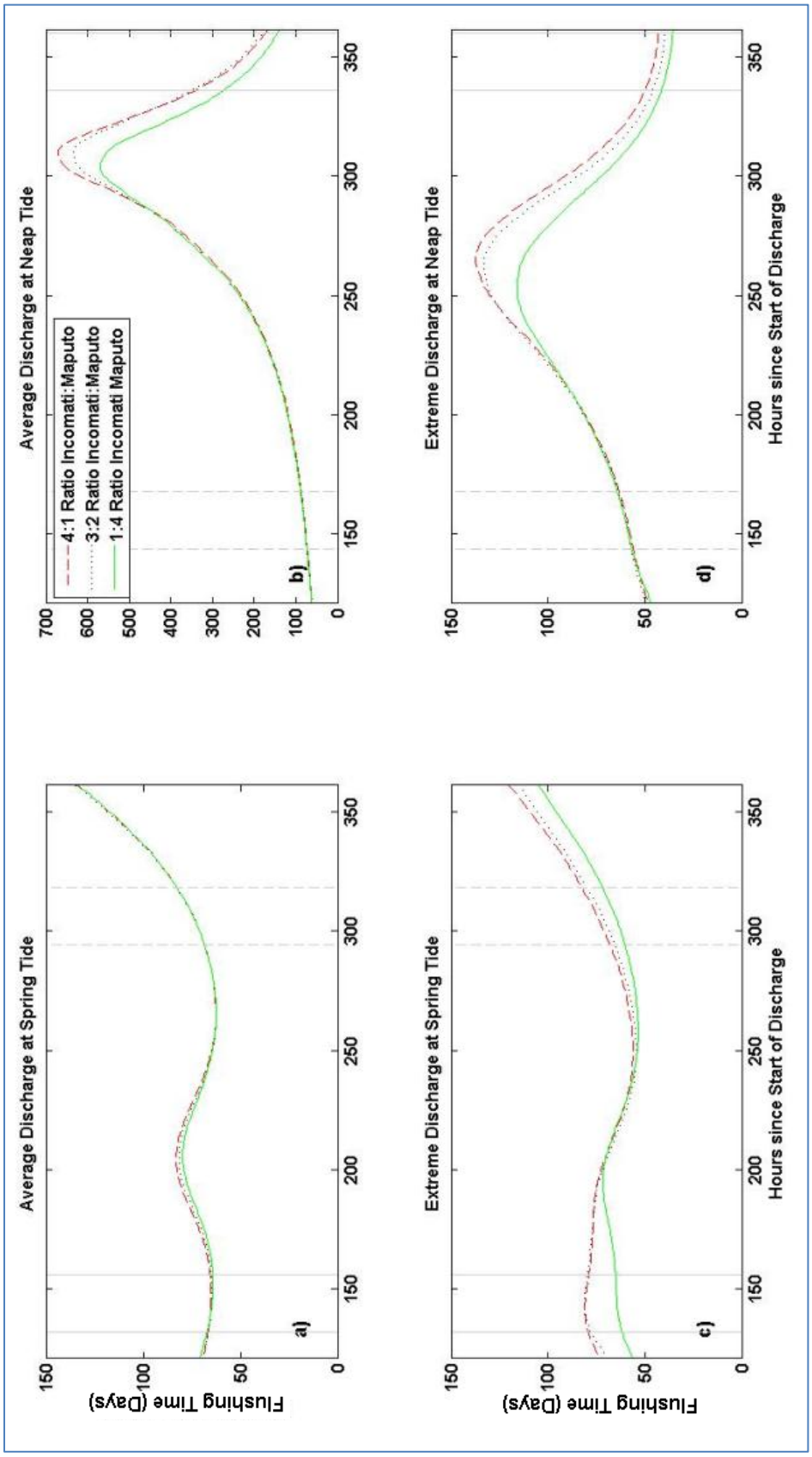

Figure 39: Development of dry season residence time for 5-day moving windows for varying discharge ratios: a) average wet season discharge at spring tide, b) average wet season discharge at neap tide, c) extreme discharge at spring tide and d) extreme discharge at spring tide. Varying Incomati : Maputo discharge ratios, with the red dashed line indicating a ratio of 4:1, the black dotted line a ratio of 3:2 (same as in previous figure) and the green line indicating a ratio of 1:4

This is expected to be an effect of the first days of very efficient decreases of tracer concentrations that were found in all runs being followed by spring tide, which also leads to smaller flushing times.

The extreme wet season runs showed significantly different flushing time patterns, with smallest flushing times just after neap tide. This can be explained taking into account the velocity cross sections and vertical salinity differences. During neap tide, a clear estuarine circulation developed, with fresh water flowing out of the bay in surface layers and saline water flowing into the bay in the deeper layers. This classical estuarine circulation showed large velocities which made flushing of the estuary very efficient and lead to the smaller flushing times. Flushing times stay small for some time after neap tide, until mixing becomes more significant during spring tide. Directly during spring tide, flushing is still relatively effective, possibly due to the direct effect of tidal advection. After spring tide, however, when the water column is still mixed but tidal velocities decrease, leading to less advection, a peak in flushing times is reached. This is somewhat surprising as it seems to not be in accordance with the conclusions of Linden and Simpson (1988), according to which the maximum flushing times should be found during spring tide, when tidal mixing erodes the density stratification and thereby inhibits the density currents. However, this is in accordance with the findings of Lencart e Silva (2007), who found, for river discharge of both, 800 m^3s^{-1} and 3200 m^3s^{-1} that the maximum flushing times occurred under tidal velocities corresponding to a transition between neap and spring tide or vice versa.

It is possible that, due to the very large difference between spring tide and neap tide in Maputo Bay, the flushing due to tidal advection during spring tide is in fact important enough for maximum flushing times to peak not during spring tide but afterwards, when the water column is still mixed, leading to the absence of density currents, but tidal advection loses its efficiency towards neap tide. The input of one extreme freshwater pulse into a dry season regime may not have been enough to fully develop the dynamics found explained by Linden and Simpson (1988). Further research in wet season conditions will be needed to reach a final conclusion about the actual origin of this divergence of the model results from the theory proposed by those authors.

Taking into account the above results, it is suggested that the estuarine plume in Maputo Bay is in fact arrested during a part of the tidal cycle. However, this arrestment does not occur during spring tide, as previously suggested, but during the transition from spring to neap tide. It seems that in this moment neither baroclinic forcing through density variations, nor barotropic forcing through tides, is strongly present, leading to the much larger flushing times. This arrestment occurs independent of the timing of the discharge in the spring-neap cycle. However, tracer concentrations after 420 hours of running the model were lower when discharge was introduced during neap tide or between neap and spring tide.

Flushing times, especially for the extreme discharge runs, were smaller when the Maputo was relatively more important. This is assumed to be related to the relative locations of the river mouths. The Incomati River mouth is located close to the northwestern part of the bay's opening. The discharge from the Incomati reaches the mouth relatively early and without mixing very much with the surrounding waters. It then leaves the bay relatively soon. The river water of the Maputo, discharging into the southern part of the bay, travels through the whole bay before reaching the opening. It has an effect over a larger area of the bay opening and stays in the bay

for longer. This way, the Maputo contributes more to the storage of buoyancy in the bay which will then force an earlier and more effective flushing through the density-driven currents. The discharge of the Maputo therefore is more important in setting the salinity field as well as the flushing times than the Incomati discharge.

During spring tide, the ratio of river discharge does not have a large influence on flushing times. This may support the idea that maximum flushing times do not occur during spring tide due to the large barotropic tidal forcing, which acts independent of discharge ratios.

It is assumed that the flushing times calculated here are slightly larger than those found in reality. This is due to the lack of mesoscale processes due to the limited extent of the model outside the bay area. In reality, shelf currents would lead to a larger mixing of the tracer outside the bay, leading to smaller return fractions of the tracer from the shelf back into the bay.

5 Wet Season Runs - Results and Discussion

In order to investigate the dynamics occurring in Maputo Bay during the wet season, a number of wet season runs were developed. These include runs 25-38 in Table 8. For these runs, only the extreme discharge quantity was applied, with timings of discharge varying between spring and neap tide. For these runs, bay-average salinities, stratification across the bay's opening, residual velocities and flushing times were calculated, varying timings of discharge as well as the discharge ratios between the Incomati and the Maputo. Furthermore were a number of runs undertaken with varying durations of discharge, to determine the effect of the discharge duration on the bay dynamics (see Chapter 5.3).

5.1 Results

Bay-average salinities

Bay-average salinities were calculated for the wet season runs according to the methodology described on page 50. Figure 40 shows the tidally-filtered results.

Over the first 72 hours, corresponding to the duration of discharge, bay-average salinities decrease stronger when discharge occurs during spring tide. These runs reach a minimum approximately 100 hours after the start of discharge and, for a discharge ratio of 3:2 (discharge Incomati : discharge Maputo), minimum bay-average salinities are 27.5. The runs with discharge occuring during neap tide also show steep bay-average salinity decreases over the first 72 hours. However, the minimum is only reached later in the simulation, corresponding to a salinity of 28.3 for the run with a 3:2 discharge ratio. Overall, bay-average salinities were usually larger for a discharge during neap tide.

Generally, bay-average salinities increase significantly during neap tide and decrease slightly during spring tide, independent of timing or ratio of discharge.

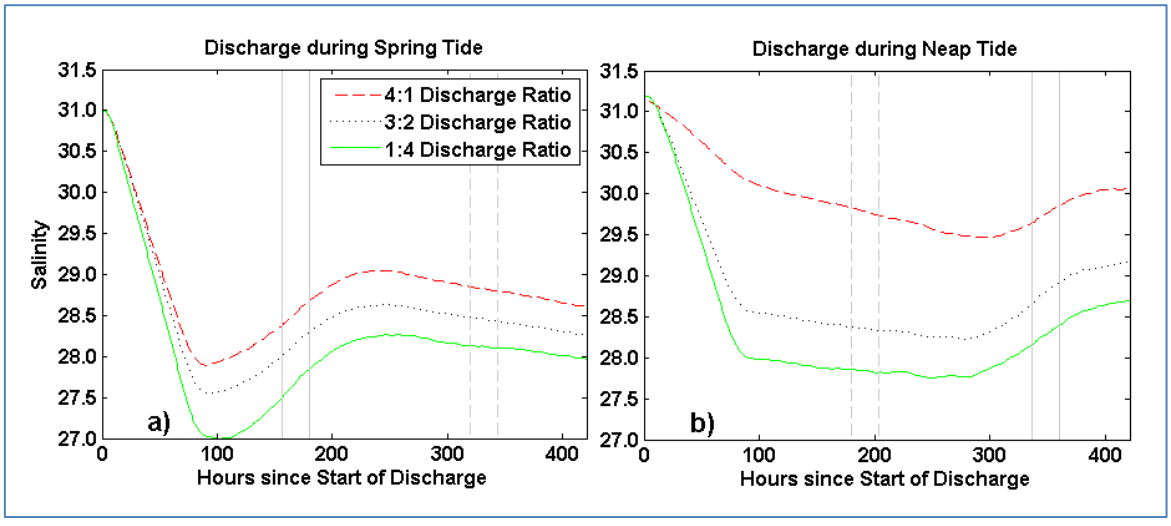

Figure 40: Tidally-filtered bay-average salinities over time for wet season runs with varying discharge ratios for a) extreme discharge during wet season spring tide, b) extreme discharge during wet season neap tide. Solid vertical lines indicate time of neap tide, dashed vertical lines indicate time of spring tide.

The runs with a larger Incomati discharge (4:1 ratio) always show larger bay-average salinities. This is most pronounced in the first 72 hours of a discharge during neap tide when bay-average salinities for the 4:1 discharge only decrease by around 1.1 units while bay-average salinities for the 1:4 discharge ratio decrease by around 3 units.

Stratification vs Mixing (Φ)

The potential energy anomalies φ for the wet season runs with discharge during spring tide and during neap tide are shown in Figures 41 and 42, respectively.

Maximum values of φ are approximately 300 Jm^{-3}. For a discharge during spring tide, first signs of very large stratification can be observed after approximately 48 hours (3:2 discharge ratio, see Figure 41 a). For runs with discharge during neap tide, stratification can already be observed during the beginning of the simulation. A semi-diurnal modulation between stronger and weaker stratification is found in all runs.

Generally, stratification is strongest during neap tide and very weak or absent during spring tide. The largest stratification is usually found in the middle of the cross-section and extending towards the South-East, while the north-western part of the opening usually shows no or very little stratification. The runs with varying discharge ratios clearly show that a larger discharge of the Incomati (4:1 ratio, Figure 41 c and Figure 42 c) leads to an earlier arrival of large values of φ at the bay's opening. Runs with a larger Maputo discharge on the other hand (1:4 ratio, Figure 41 b and Figure 42 b) lead to a longer presence of increased stratification, such as visible in Figure 42 b after approximately 350 hours, during neap tide.

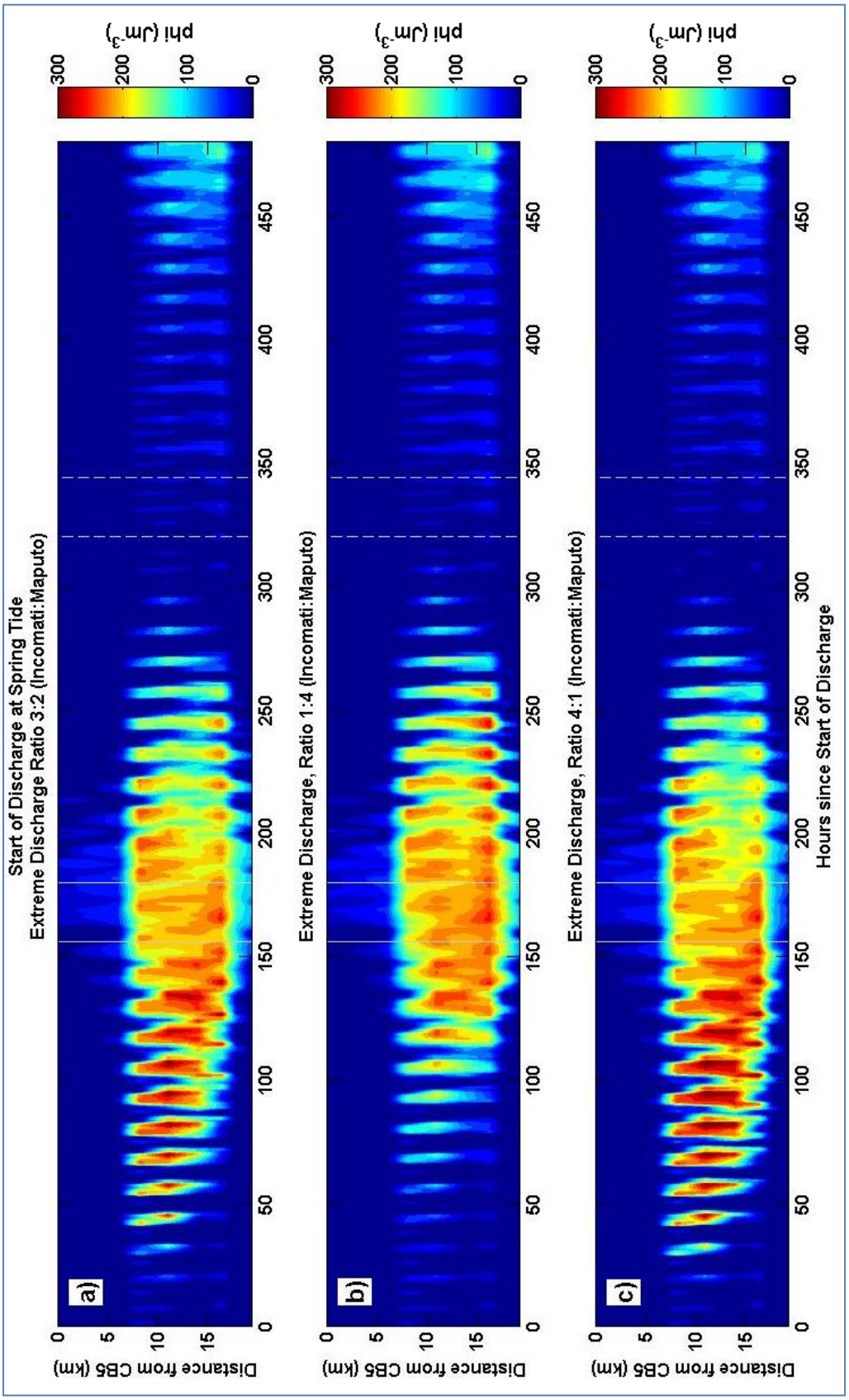

Figure 41: Wet season development of *φ* over time along Maputo Bay's mouth, for model start during spring tide and varying Incomati : Maputo river discharge ratios: a) 3:2, b) 1:4, c) 4:1. Solid vertical lines indicate time of neap tide, dashed vertical lines indicate time of spring tide.

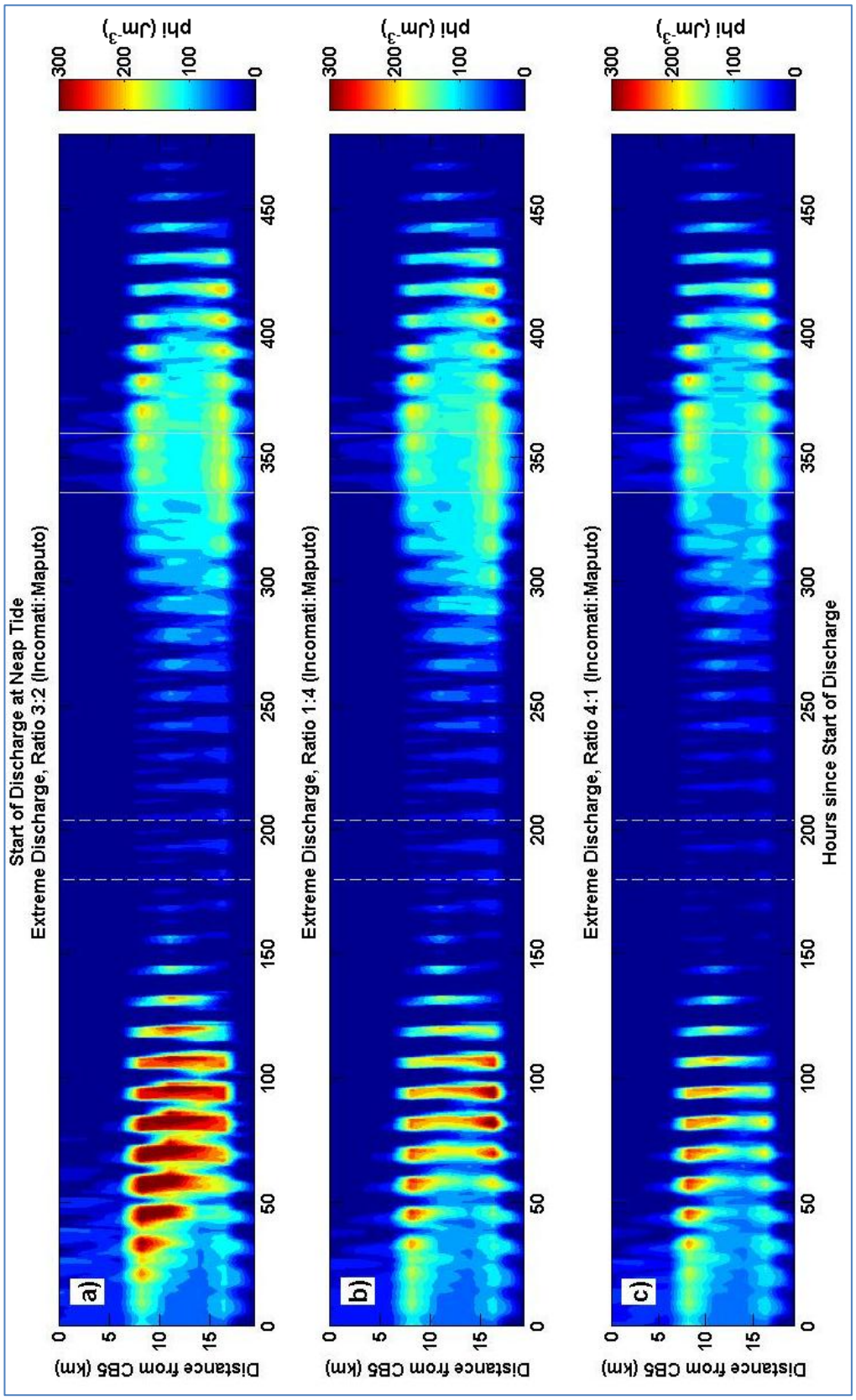

Figure 42: Wet season development of φ over time along Maputo Bay's mouth, for model start during neap tide and varying Incomati : Maputo river discharge ratios: a) 3:2, b) 1:4, c) 4:1. Solid vertical lines indicate time of neap tide, dashed vertical lines indicate time of spring tide

Residual velocities

The residual velocities for four time steps are shown in Figures 43 and 44 for discharge during spring tide and neap tide, respectively. Four moments in time where chosen, for which the residual velocities are presented:

- 72 hours after the start of the model run and the beginning of discharge of the river water;
- At the moment of the largest spatial extension of φ peaks, indicating a moment of a large spatial extension of stratification across the bay's opening;
- During spring tide;
- During neap tide

Maximum residual velocities into and out of the bay of 10 and 15 cms^{-1}, respectively, were found.

72 hours after discharge (Figure 43 a, e, j and Figure 44 a, e, j), as well as during the maximum extension of φ (Figure 43 b, f, j and Figure 44 a, e, j) flows out of the bay are found at the surface over most of the cross section of the bay's opening. Maximum velocities as well as spatial extension of the surface outflows were larger for runs with discharge during spring tide.

During spring tide (Figure 43 c, g, k and Figure 44 a, e, j) the flow structure is described by an intermediate case between vertical and horizontal flow cells: significant inflows are found in the deep parts of the channel. Significant outflows occur in surface layers around 6-10 km away from station CB5 while the surface layers over the deeper channel now show only very weak flows with velocities close to 0.

During neap tide (Figure 35 d, h, l and Figure 44 a, e, j), the flow patterns are characterised by an inflow in deeper parts and an outflow in surface layers. Velocities are slightly larger for runs with discharge during neap tide.

Generally, differences between varying discharge ratios are small. When discharge occurs during spring tide, 72 hours after the start of discharge the velocities of outflow in the surface layer are larger for a larger Incomati discharge (ratio 4:1, Figure 43c) than for a larger Maputo discharge (ratio 1:4, Figure 43b). During the maximum extension of φ, the situation has switched, with surface outflows now being larger for a larger Maputo discharge (ratio 1:4, Figure 43f) than for a larger Incomati discharge (ratio 4:1, Figure 43j). For discharge during spring tide, surface velocities are slightly larger for the 1:4 ratio (more Maputo discharge) during both time steps (Figure 44 e and f, compared to I and j). Independent of the timing of the discharge, current velocities do not show significant differences between the varying ratios during spring tide. During neap tide, a small difference can be found for the runs with discharge during neap tide: surface velocities in the middle of the bay's opening are slightly higher for the 4:1 ratio (Figure 44l) than for the 1:4 ratio (Figure 44h).

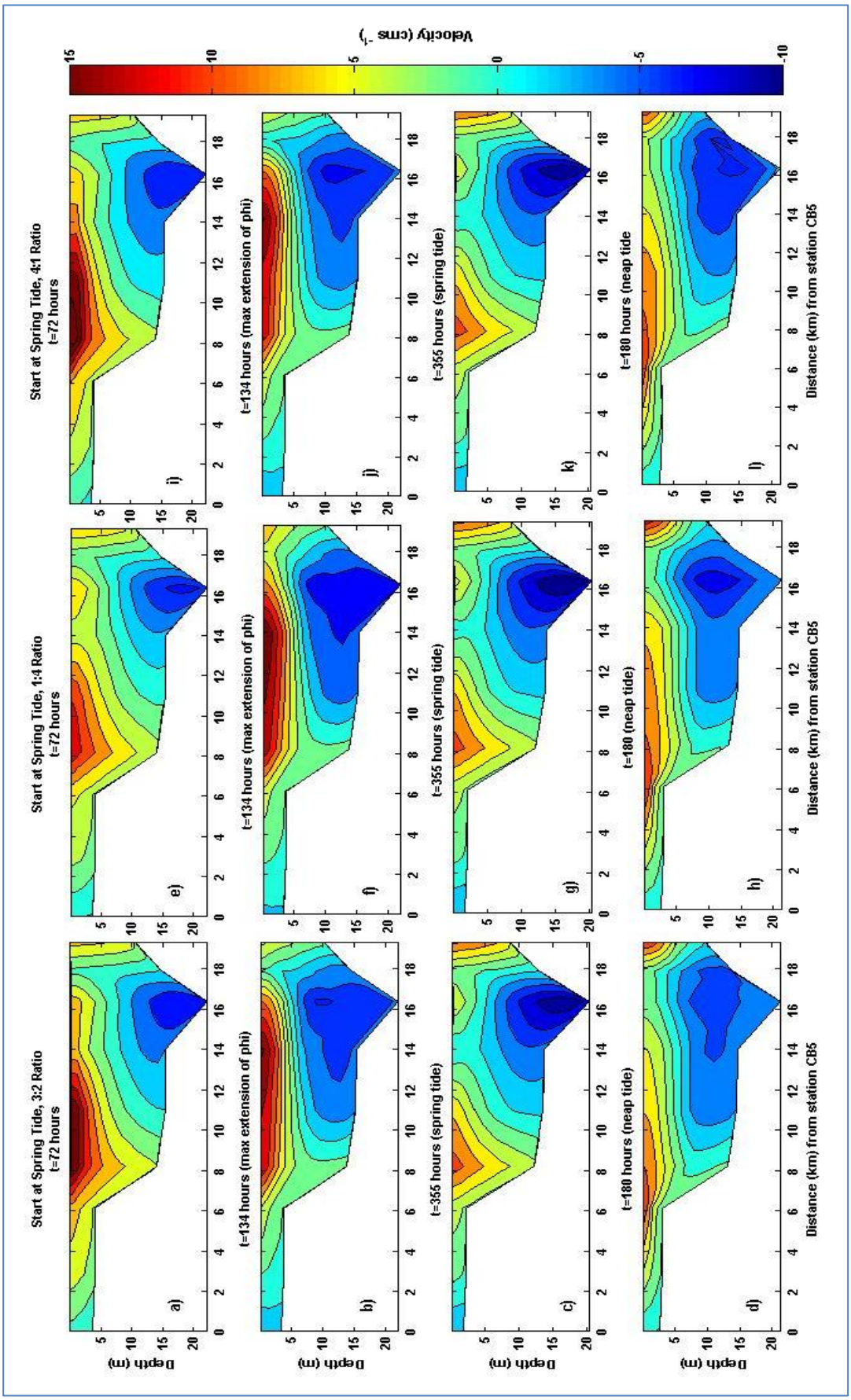

Figure 43: Wet season residual velocities for model runs with varying discharge ratios, starting at spring tide. Positive velocities indicate flow out of the bay, negative velocities represent flow into the bay. The left column shows model runs with a 3:2 ratio, the middle column discharge with a 1:4 ratio and the right column shows discharge with a 4:1 ratio.

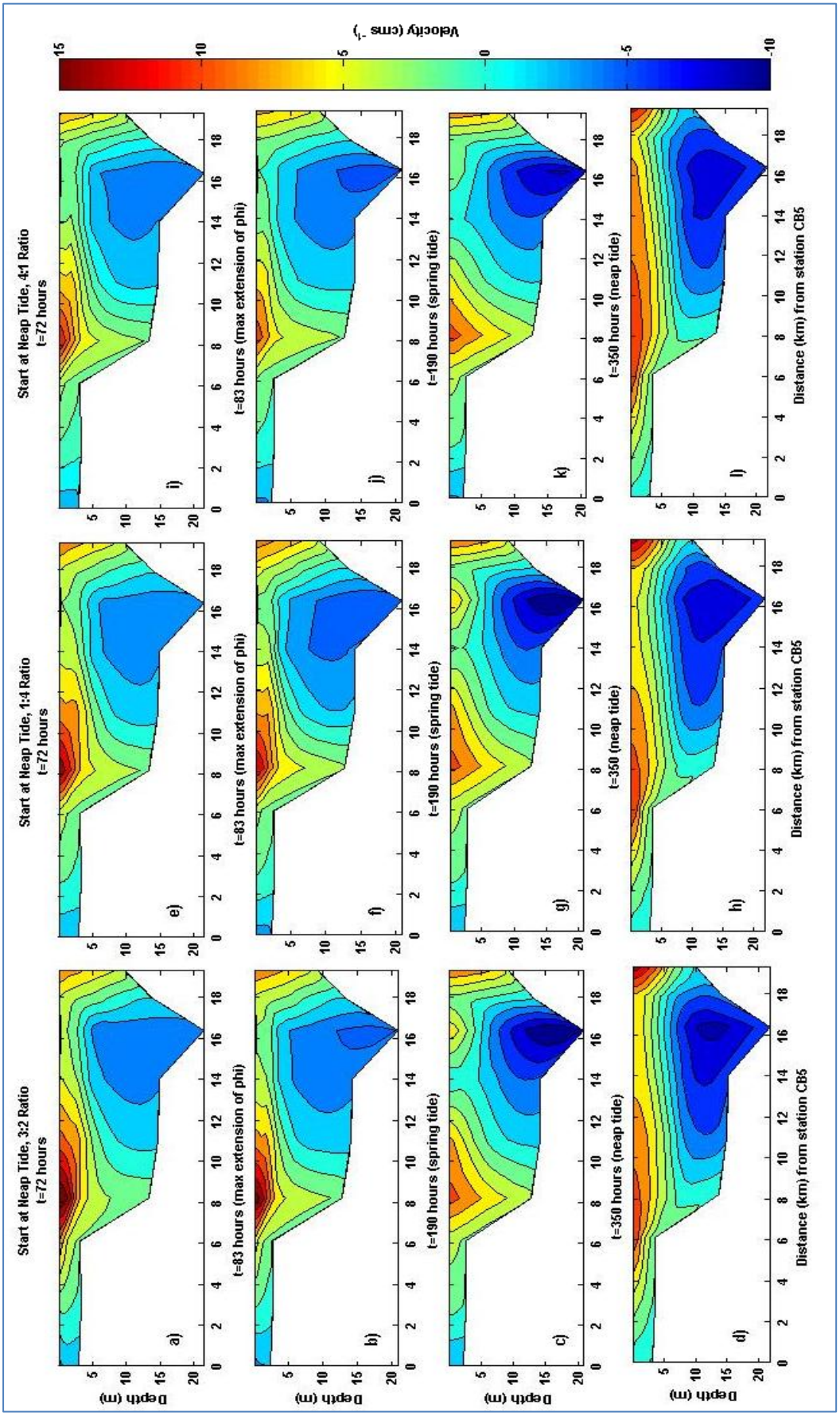

Figure 44: Wet season residual velocities for model runs with varying discharge ratios, starting at neap tide. Positive velocities indicate flow out of the bay, negative velocities represent flow into the bay. The left column shows model runs with a 3:2 ratio, the middle column discharge with a 1:4 ratio and the right column shows discharge with a 4:1 ratio

Flushing Times

The dynamic flushing times were, as for the dry season runs, calculated from bay-average tracer concentrations. Please refer to Chapter 4.6 for the methodology.

The flushing times of extreme discharge introduced into a wet season environment can be found in Figure 45. Maximum flushing times are 60 days and minimum flushing times are 20 days.

Maximum flushing times occur around spring tide and minimum flushing times occur during neap tide, independent of discharge ratio and timing of discharge.

The runs with a larger Incomati discharge show larger flushing times around spring tide (especially for discharge introduced during neap tide), whereas flushing times during neap tide are very similar for all ratios and may even be slightly smaller for a comparably larger Incomati discharge (ratio 4:1).

The smallest minimum flushing times are observed when the discharge of the freshwater pulse occurs during neap tide (Figure 45b). Maximum flushing times are also smaller for discharge during neap tide, apart for the run with a 4:1 discharge ratio which shows significantly higher flushing times than the 3:2 and 1:4 discharge ratios.

5.2 Discussion

Compared to dry season runs with an extreme discharge, the wet season runs with an extreme discharge were generally characterised by lower bay-average salinities, larger stratification, higher residual velocities and lower flushing times.

The lower bay-average concentrations are due to the freshwater that was already present in the initial conditions of the simulations.

Bay-average salinities decreased most strongly over the first 72 hours, which correspond to the duration of the discharge of the freshwater pulse and is therefore a direct effect of a larger amount of freshwater introduced to the bay.

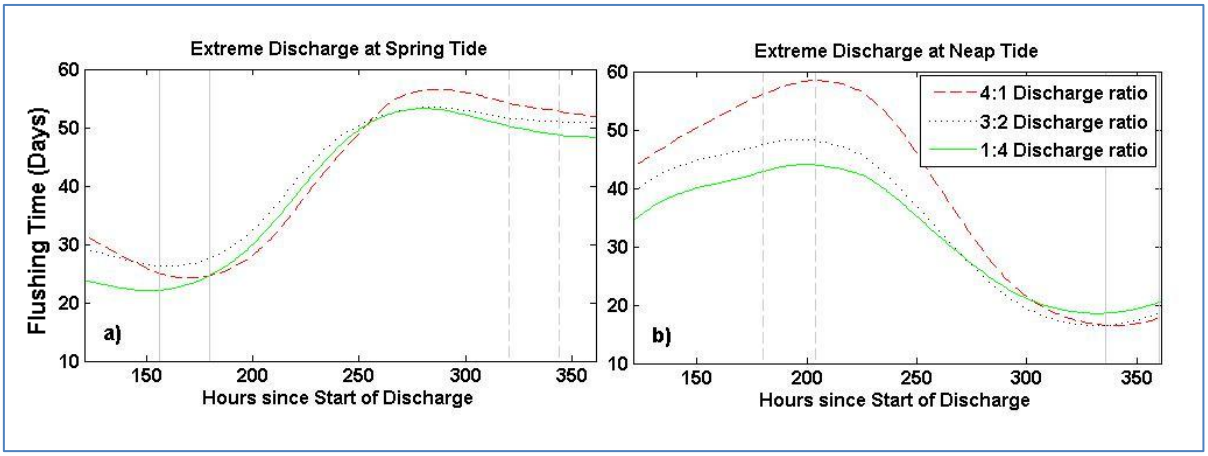

Figure 45: Development of flushing times for wet season runs with varying discharge ratios for a) discharge during spring tide and b) discharge during neap tide. Solid vertical lines indicate time of neap tide, dashed vertical lines indicate time of spring tide.

Due to the background conditions now being characteristic of the wet season, bay-average salinities decrease more strongly than for the dry season runs with extreme discharge. All runs, independent of the timing of the freshwater discharge or the discharge ratio between the two rivers, showed slightly decreasing bay-average salinities during spring tide and stronger increases in salinity during neap tide. It is probable that during neap tide, when tidal forcing was weak and the water column stratified vertically, exchange between the bay and the shelf was efficient, leading to an export of freshwater from the bay to the shelf as well as salt water from the shelf to the bay, thereby increasing salinities in the bay. During spring tide tidal forcing was stronger, mixing the water column vertically. The density-currents present during neap tide weakened and the barotropic bay-shelf exchange was probably less efficient than the baroclinicly-forced exchange during neap tide. There are two hypotheses which might have led to the decreasing bay-average salinities during spring tide: firstly, it is possible that some of the freshwater present in the river arms got transported into the bay. As the river arms are not included in the mask to calculate bay-average values, this could lead to a decrease in salinities if the input from the river arms is larger than the export of freshwater to the shelf. A second possibility is a process occurring outside the bay: during spring tide some of the freshwater that had been transported out of the bay during neap tide and mixed with surrounding waters towards spring tide. This water may have been advected back into the bay, thus decreasing bay-average salinities.

The runs with discharge during neap tide showed overall larger minimum bay-average salinities. This is probably due to the mixing induced to the water column when the freshwater arrives in the bay. A discharge during spring tide will be prone to large mixing, leading to a lower bay-shelf exchange. This in turn means that bay-average salinities decrease as little of the freshwater leaves the bay. Due to the large amount of freshwater in the bay, the recovery during the following neap tide is larger. The opposite happens when discharge occurs during neap tide, when the bay-shelf exchange is efficient (due to little mixing) and a lot of the freshwater is flushed out of the bay, leading to larger bay-average salinities.

A comparably larger discharge of the Incomati lead to larger bay-average salinities. This was already observed in the dry season runs and is due to the location of the Incomati river mouth located close to the bay opening. The Incomati discharge leaves the bay faster than the Maputo discharge, which influences a larger bay area before reaching the shelf. The run with a 4:1 ratio-discharge induced during neap tide has shown significantly higher bay-average salinities than the other runs. The large input of freshwater of the Incomati reached the bay's opening fast, when tidal amplitudes were still relatively small. Much of the freshwater left the bay soon after discharge, before tidal mixing increased and weakened density currents. The difference between the different discharge ratios was less significant for discharge during spring tide, as the Incomati discharge was prone to large mixing when it spilled into the bay, associated with a large tidal amplitude due to spring tide.

The stratification found for the wet season runs was generally larger than that of the dry season runs, due to the larger amount of freshwater in the bay, as was seen by the bay-average salinities.

The fact that the neap tide runs show some stratification from the beginning of the run on can probably be explained by the larger freshwater present in the bay in the initial conditions. The

stratification observed from the beginning on may therefore not be an effect of the input of the discharge pulse but rather the freshwater present in the bay before the start of the simulation. This idea is also supported by the fact that in the first hours of the simulation, all runs with discharge during neap tide, independent of discharge ratio, show the same pattern.

For a discharge during neap tide, a larger Incomati discharge (4:1 discharge) showed the weakest stratification. A possible explanation may be the presence of freshwater in the initial conditions which supported density currents that were very effective in exporting the freshwater from the Incomati out of the bay. The run with a comparably larger discharge of the Maputo River (1:4 ratio) showed stronger stratification for the period approximately 50-120 hours after start of the discharge as the Maputo river discharge needed longer to reach the bay opening. During the time it took to reach the opening, the density currents had already weakened and exchange between the bay and the shelf was less efficient.

Residual velocities over the cross section of the bay's opening were stronger for an extreme discharge during the wet season than for the discharge during the dry season. This is due to the freshwater present in the initial conditions influencing density currents. The freshwater pulses introduced to the wet season environment are bedded into a background discharge. This extra discharge increased stratification of the bay, as was seen in Chapter 5.2. The freshwater present in the bay at the beginning of the simulation of the dry season runs was smaller, which lead to less intense stratification.

The vertical cells of in- and outflow were less pronounced than during the dry season runs. This is due to the larger buoyancy in the system, leading to more stratified conditions.

The runs with discharge introduced during wet season spring tide showed, after 72 hours of the simulation, larger surface velocities when the discharge of the Incomati was larger. This was due to the water of the Maputo not having arrived at the bay's opening yet and therefore not having been able to influence exchange with the shelf. Due to the larger mixing associated with spring tide, the plume of the Maputo needed a longer time to reach the opening, whereas the Incomati river mouth is located close to the opening, influencing bay-shelf exchange early on in the simulation. During the maximum extension of stratification (second time step in the velocity plots), the discharge from the Maputo had arrived at the bay opening and increased currents. This effect is stronger when the discharge of the Maputo is larger. The influence of the Incomati, on the other hand, had decreased at this point, due to some of the discharge already having left the bay earlier.

When discharge was introduced during neap tide, the first time steps showed larger residual velocities for the run with a larger discharge of the Maputo. This is in accordance with the larger stratification, which increased density currents. It is assumed that the stratified conditions of the bay during the discharge supported stronger density currents which lead to a fast arrival of the Maputo discharge at the bay's mouth. The Maputo discharge was therefore able to reach the opening earlier when discharge was induced during neap tide, compared to an introduction during high-mixing conditions of spring tide.

In later time steps, differences between the varying ratios were very small, in accordance with the stratification observed. The salinity fields had become more similar, with the influence of the discharge pulses decreasing and the background discharges increasing.

Flushing times are smaller for the wet season runs, probably due to the larger potential energy which leads to larger velocities, making the bay-shelf exchange more efficient.

During neap tide the bay stratifies which leads to strong density currents and an efficient bay-shelf exchange. Flushing times are therefore small during neap tide. During spring tide, on the other hand, mixing is strong, eroding the vertical density gradients and arresting the density currents. Flushing times were therefore largest during spring tide. This shows that unlike in dry season conditions, the wet season runs were in accordance with the laboratory results from Linden and Simpson (1988). The estuarine plume is in fact arrested during high mixing of spring tides and released during neap tide when strong density gradients lead to an efficient bay-shelf exchange.

It can therefore be concluded that an arrestment of the estuarine plume occurs during spring tide in the wet season when mixing is large.

Flushing times during spring tide were larger for a larger discharge of the Incomati (4:1 ratio). This may be due to a smaller potential energy anomaly present in the system. Figure 34 showed that values of φ during the spring tide are close to zero for all runs starting at neap tide, however, φ values for the 1:4 discharge ratio are slightly larger than for the 4:1 ratio. This means that during spring tide, the cross section of the bay opening was slightly more stratified when the discharge of the Maputo was larger. The baroclinic circulation was therefore slightly larger too, leading to more efficient shelf-bay exchange which may explain the smaller flushing times when the influence of the Maputo was larger than that of the Incomati. The Maputo River is more important in forcing the bay's average salinities, inducing a small amount of stratification even during spring tide and therefore decreases flushing times.

5.3 The Effects of Varying Durations of Discharge on Flushing Times and Bay-average Salinities

Results

Previous research suggested that salinities outside the 20-30 range will hamper production in the mangroves and affect early life stages in mangrove habitats that sustain economically important life stocks. As the rivers Maputo and Incomati consist of dam systems through which the timing of freshwater discharge can be managed, research was undertaken to determine how different timings and durations of discharge of the same amount of freshwater influence bay-average salinities. Figure 46 shows the tidally-filtered bay average salinities for several 40-day runs. Due to the application of the filter, the first and last 33 hours should not be taken into account.

Generally, bay-average salinities were slightly lower when discharge started during spring tide. During spring tide, bay-average salinities were usually decreasing and during neap tide they were strongly increasing. Differences between varying durations of discharge can mainly be observed over the first 300 hours after beginning of the discharge. Afterwards, bay-average salinities follow similar patterns.

The runs with discharge over 2, 3 and 5 days all showed very similar bay-average salinities. Only before the first neap tide can significant differences be observed, with bay-average salinities dropping slower for runs in which discharge is spread over more days. Bay-average salinities drop most slowly for a discharge over 10 days but stay below the values of other runs over the complete simulation time of the spring tide discharge and until approximately 700 hours after a discharge during neap tide.

The runs with discharge starting during spring tide showed minimum bay-average salinities of approximately 27.5 for a discharge duration of 2, 3 or 5 days and minimum salinities of around 28 for a discharge with a duration of 10 days.

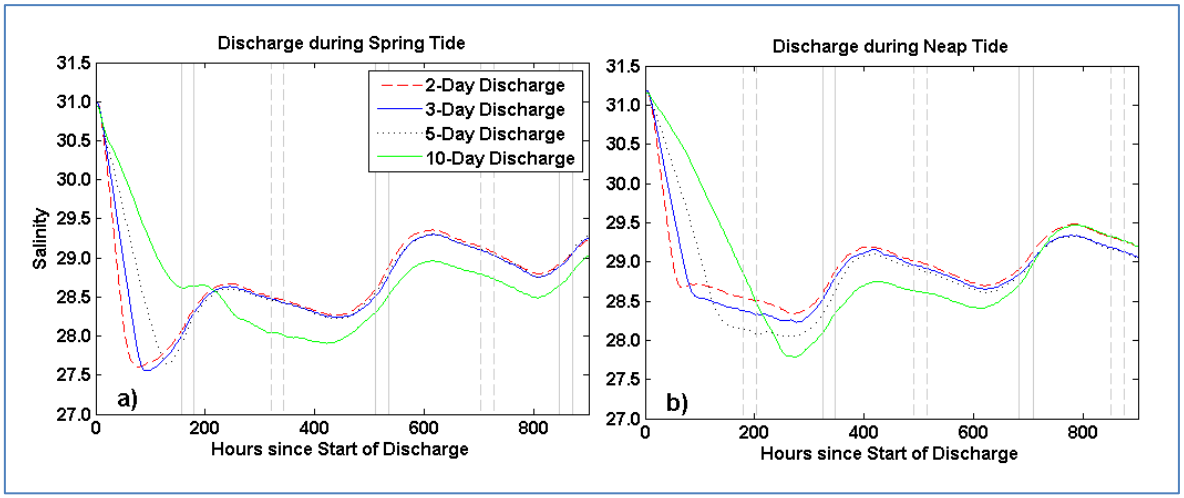

Figure 46: Bay-average salinities for wet season runs with varying discharge durations and timings, with a) discharge during spring tide and b) discharge during neap tide. Solid vertical lines indicate time of neap tide, dashed vertical lines indicate time of spring tide.

The minimum values occurred after approximately 100-150 hours for the 2, 3 and 5-day duration discharges and approximately after 400 hours for the 10-day duration of discharge. The runs with discharge during neap tide showed smallest minimum values of approximately 27.7 for a discharge duration of 10 days, 28 for a duration of 5 days, 28.3 for 3 days and 28.4 for 4 days. Minimum values occurred approximately 300 hours after the start of discharge, independent of the duration of discharge.

To understand the causes of the varying developments of bay-average salinity with varying durations of discharge, the potential energy anomalies along the bay opening were calculated. Values of φ for a discharge during spring tide are shown in Figure 47 and values for discharge starting during neap tide are shown in Figure 48.

Differences can mainly be observed in the first third of the simulation period, afterwards the energy anomalies become similar for all durations of discharge.

When discharge starts during spring tide, in the first 100 hours φ is largest for a discharge duration of 2 days. Between 100 and 150 hours it is largest for a discharge duration of 5 days and after 150 hours, until the following spring tide, stratification is slightly stronger for a discharge duration of 10 days. After approximately 300 hours, potential energy anomalies are very similar for all discharge durations.

When discharge starts during neap tide, φ is in the first 150 hours largest if the discharge is introduced over 2 days. During the following spring tide, approximately 200 hours after beginning of discharge, φ becomes largest for runs with discharge over 10 days. In this case, even during spring tide, φ values of up to 120 Jm^{-3} can be observed, compared to only approximately 50 Jm^{-3} if discharge occurs during 2 days. Energy anomalies over the following neap tides show slightly larger φ values for the run with discharge spread over 10 days, but differences decrease in time.

Discussion

The results have shown that the stratification across the bay-opening is influenced strongest during the first few days of the simulation. Those days showed strongest stratification where discharge was concentrated over a shorter time period. This is logical as the bay was characterised by a larger amount of freshwater for the runs with a shorter discharge duration. Later on, stratification was larger for runs where discharge was divided over a larger period. This was due to the arrival of the freshwater at the bay opening, which had already occurred earlier for runs with a more concentrated discharge. The run with a 10-day discharge starting at neap tide showed some significant stratification even during spring tide, due to the constant input of a larger amount of freshwater, which overcame tidal mixing to a certain degree. When the same amount of discharge was introduced over 5 days, most of the discharge had already been in the bay longer and was mixed by the tides more.

The large differences in stratification over the first days are also shown in the developments of bay-average salinity. Over the first hours, the drops in bay-average salinity are steepest for runs with a shorter duration of discharge, as a logical consequence of the larger freshwater discharged, compared to runs where the discharge is divided over a longer period.

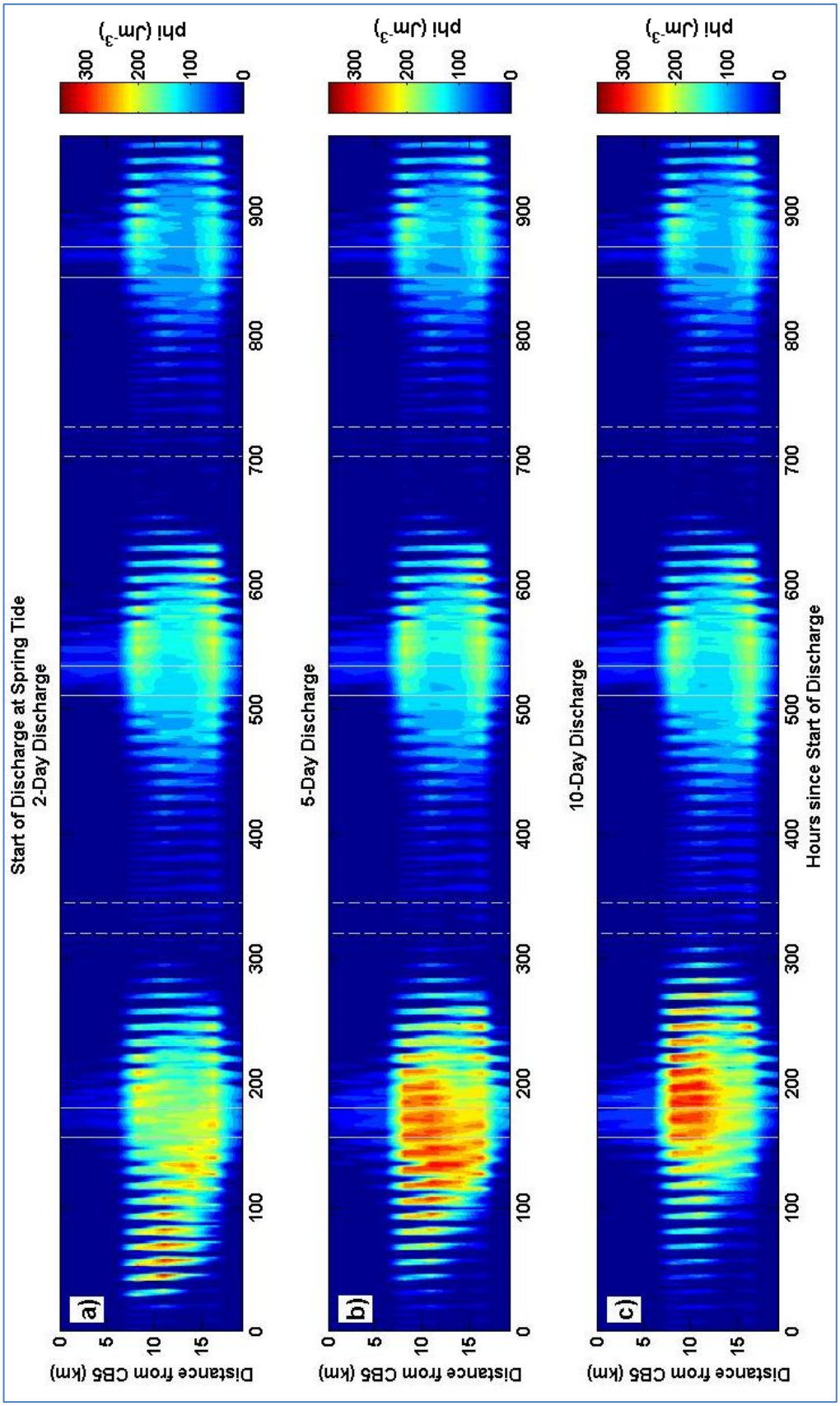

Figure 47: Wet season development of φ over time along Maputo Bay's mouth, for model start during spring tide and varying durations of discharge:a) 2 days, b) 5 days, c) 10 days. Solid vertical lines indicate time of neap tide, dashed vertical lines indicate time of spring tide

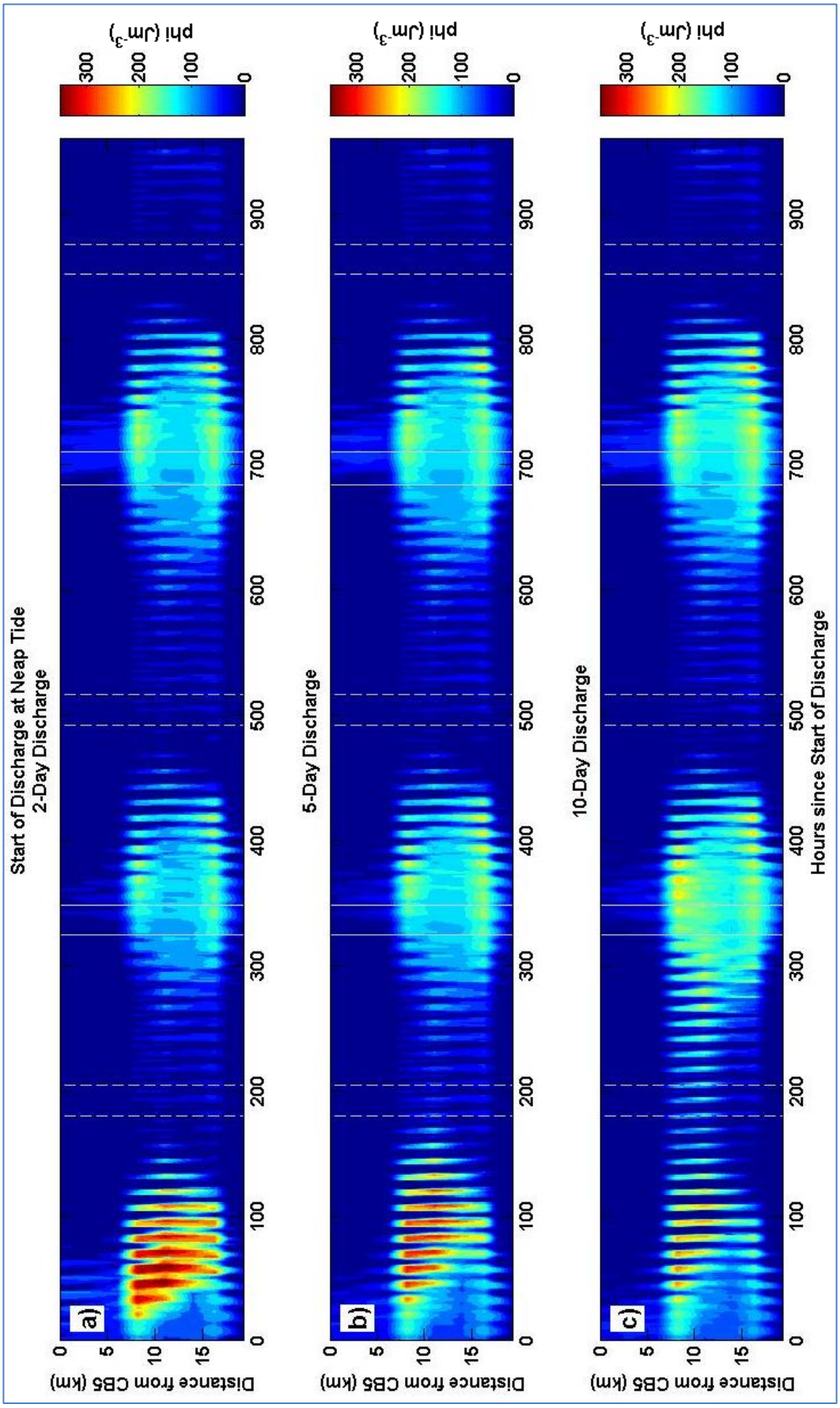

Figure 48: Wet season development of φ over time along Maputo Bay's mouth, for model start during neap tide and varying durations of discharge: a) 2 days, b) 5 days, c) 10 days. Solid vertical lines indicate time of neap tide, dashed vertical lines indicate time of spring tide.

A local minimum in bay-average salinity is usually found approximately at the end of the discharge, corresponding to approximately 48 hours for the runs with discharge over 2 days and 240 hours for the discharge over 10 days. The bay-average salinities are furthermore influenced by the spring-neap tidal cycle which leads to variations in mixing and stratification of the water column, as explained in previous chapters.

The peculiarity of recurring decreases in bay-average salinities with spring tide may be due to processes occurring outside the bay, described by the following hypothesis: during neap tide, when mixing is low, the low-salinity water from the bay is exported and replaced by shelf water with high salinities. During spring tide, when mixing is large, the low salinity water that was transported to the shelf mixes with surrounding higher salinity shelf water, creating a water mass of intermediate salinity. Through tidal advection, some of this intermediate-salinity water is re-introduced back into the bay, thus decreasing bay-average salinities.

In runs with a short discharge duration, the bay is influenced largely in the beginning of the simulation period. However, the freshwater is exported from the bay quicker, leading to increases in bay-average salinities occurring earlier than for the runs with a larger discharge duration.

Over most of the research period, bay-average salinities were smaller for longer discharge periods, as well as for a discharge starting at spring tide.

Managing the dams of the Maputo and Incomati rivers in such a way that discharge is spread over a longer period, possibly starting discharge during spring tide, can therefore help to maintain salinities below the 30 threshold value which is assumed to positively influence the functioning of the ecosystem. However, the differences in bay-average salinity with duration of discharge decrease with time. Especially the management of the Maputo is assumed to be important in this strategy, as the previous chapters have demonstrated the Maputo being more influential in setting the bay dynamics through the salinity field and inducing an overall stronger stratification.

6 Conclusion

This dissertation aimed at finding out whether and under which conditions the estuarine plume of Maputo Bay, Mozambique, is arrested and how the bay-shelf exchange and the salinity field are affected.

A three-dimensional hydrodynamic model was applied, based on a previously published model. The model was calibrated to a satisfying level and a comparison between both models has shown that the new model represents better the stratification-mixing cycles occurring in the wet season.

A number of scenarios of varying discharges for the most important rivers, Incomati and Maputo, and varying timings of input of discharge were developed and run with the software Delft3D. Model runs were taken in both, dry season and wet season conditions. Dry season conditions were forced by four amounts of discharge: no discharge, a typical dry season discharge, an average wet season discharge and an extreme wet season discharge. The two latter cases represent conditions in the end of the dry season, when there is little freshwater present in the bay but large discharge pulses can already occur, or possible extreme events that can occur throughout the year. The runs set during the wet season were only forced by the extreme wet season discharge, as the input of small amounts of freshwater would not have produced any results useful in this investigation.

For the runs set in a dry season environment, the following conclusions can be drawn:

The runs in which no discharge, a dry season discharge and average wet season discharge was applied all showed similar dynamics and stratification across the opening of the bay was mainly influenced by water temperature variations of the surface, not by the input of buoyancy through freshwater. Flushing times were smallest during spring tide, when barotropic forcing was most efficient in the exchange between the bay and the adjacent continental shelf. Largest flushing times were not found during weakest tidal mixing of neap tides but approximately 40 hours earlier. This may be due to a peak of surface heating of the bay that coincided with neap tide. Due to the differential heating between the bay and the shelf, supported by low mixing of neap tide, a weak baroclinic circulation may have developed.

The dry season runs where an extreme discharge was introduced showed very different dynamics, with large variations in stratification found during the arrival of the freshwater plume as well as during neap tide. The amount of stratification found over a cross section over the bay's mouth varied with the timing of input of the discharge, related to stronger mixing during spring tide and weaker mixing during neap tide. This lead to more elevated temporal and spatial values of potential energy anomalies (φ) across the bay's opening for the model runs where discharge was introduced during spring or between neap and spring tide. Cross sections of the residual velocities across the bay's opening showed similar patterns to the dry season runs during spring tide, with outflows over the whole depth of the deeper channel and inflows over the whole depth of the more shallow areas, in accordance with the effects of stratification for a bay where the tides are mainly characterised by a standing wave. Further research would be needed to determine whether the progressive wave component in Maputo Bay is in fact so small that the Stokes effect can be neglected. During neap tide, on the other hand, velocity patterns were very different: due

to the weaker mixing and input of buoyancy from freshwater, a classical estuarine circulation could develop, with fresh surface layers flowing out over most of the cross section and saline bottom layers flowing in in larger depths. This estuarine circulation also lead to very small flushing times due to the efficient transport of water in and out of the bay. Largest flushing times for the extreme discharge runs were found between spring and neap tide and not, as would have been assumed from the Linden and Simpson (1988) experiments, during spring tide. A hypothesis has been suggested to explain this: it is possible that the input of a single large discharge pulse into a dry season environment was not enough input of buoyancy to be comparable to the experiments of Linden and Simpson. The tides during spring tide might have been sufficiently strong in producing barotropic forcing that the absence of baroclinic forcing due to the erosion of density gradients was covered up. It is therefore assumed that the lowest flushing times were found between spring and neap tide due to the combined relatively weak forcing from the baroclinic forcing from density gradients (due to the water column still being relatively mixed) and the barotropic forcing from tides weakening towards neap tide.

Even though a difference was observed in mixing and stratification of the extreme discharges depending on the timing of their input, it remains difficult to take conclusions on the effect of timing of discharge on flushing times. Flushing times for the various phases of the tidal cycle were similar. The tracer concentrations found at the end of the research period were smallest for discharge introduced during neap or between neap and spring tide. However, this situation might have been different if the model had been run for a further seven days, due to the different developments of flushing time over the spring-neap cycle.

It can furthermore be concluded that there is in fact a difference in flushing time with the ratio of discharge between the two main rivers. If the discharge of the Maputo is larger than that of the Incomati, flushing times are generally smaller. This is related to the location of the Maputo at the southern end of the bay, while the Incomati mouth is located very close to the bay's opening. The Maputo water therefore travels through a larger part of the bay, having a larger influence area than the Incomati, which was also confirmed by the larger influence on bay-average salinities when the Maputo discharge was larger than the Incomati discharge.

This study was able to show that an arrestment of the estuarine plume of Maputo Bay can in fact be assumed. However, this arrestment seems to occur between spring and neap tide, rather than during spring tide.

From the wet season runs, the following conclusions can be drawn:

The general bay dynamics were similar to the dry season runs with an extreme discharge. However, due to the larger amount of freshwater present in the initial conditions as well as after discharging the extreme pulses, stronger stratification could develop, indicated by larger potential energy anomalies. The more significant stratification lead to increased current velocities as well as shorter flushing times. Smallest flushing times occurred during neap tide and largest flushing times occurred during spring tide, in accordance with the laboratory experiments by Linden and Simpson (1988). The timing of the discharge of the freshwater pulse had the strongest influence in the first days of discharge, due to the varying amounts of mixing induced by tides. Overall,

flushing times were slightly smaller for discharge induced during neap tide, except for a run with a larger influence of the Incomati compared to the Maputo.

As already shown in the dry season runs, the Maputo was more influential in determining the salinity and density fields in the wet season runs, due to the location of the Maputo River mouth further away from the bay's opening. This larger effect on salinity and density fields was indicated by the larger decreases in bay-average salinities and larger stratification after the first 150 hours of simulation. A large Maputo discharge induced small amounts of stratification even during spring tide conditions, preventing a complete mixing of the water column and leading to slightly smaller maximum flushing times compared to the runs with a larger discharge of the Incomati.

Concluding, an arrestment of the estuarine plume could be observed, occurring during the high mixing periods of spring tide and being released during neap tide, when density currents developed again. This arrestment occurred independent of the timing of the discharge of the freshwater plume. Maximum flushing times were slightly larger when the discharge of the Incomati was larger than that of the Maputo.

To find out how the dam systems of the Maputo and Incomati Rivers can be managed to maintain bay-average salinities between 20 and 30 for long periods, a set of model runs with the same total discharge divided over different discharge durations was developed. Results showed that spreading the discharge over a longer period and possibly starting discharge during spring tide can lead to an overall longer bay-average salinity in the given range. The run where the discharge was divided over 10 days showed lowest bay-average salinities. However, it should be taken into account that this is not a permanent effect but will be balanced out after a few tidal cycles. Furthermore may the situation be different under different conditions, such as a larger or smaller overall discharge.

The results presented here help to determine flushing times in the bay, both for freshwater, which may be important for the sustainment of natural resources, as well as for limiting pollution in the bay.

Further research will be needed to gain a further insight. Firstly, it is recommended to update the bathymetries available for Maputo Bay. The bathymetries used here may be out-dated and that way change forces such as friction. Furthermore would research into a more usable wind station be helpful to investigate to what extent the wind may play a role in influencing bay dynamics. Currents on the shelf were not taken into account in this dissertation. A nested model, taking into account mesoscale processes from the shelf would be useful, to better integrate processes occurring at the shelf. Undertaking model runs similar to those used here but with a larger duration can help to find out whether there is in fact a difference in arrestment and flushing times depending on timing of discharge in the neap-spring cycle. Measuring actual river discharge of the Maputo River will help to determine whether the relatively large salinity deficits observed here are in fact due to the predicted nature of the river data of the Maputo or are rather the result of a weakness within the model, underestimating salinities.

References

- Álvarez-Salgado, X. A., Gago, J.. Míguez, B.M., Gilcoto, M. and Pérez, F.F. (2000). Surface Waters of the NW Iberian Margin: Upwelling on the Shelf versus Outwelling of Upwelled Waters from the Rías Baixas, Estuarine, *Coastal and Shelf Science*, **51**, 821–837, doi:10.1006/ecss.2000.0714.

- Cheng, R.T., Casulli, V. and Gartner, J.W. (1993). Tidal, residual, intertidal mudflat (TRIM) model and its applications to San Francisco Bay, California. *Estuarine, Coastal and Shelf Science*, **36**, 235-280.

- Canhanga, S. (2004). Modelação Hidrodinâmica da Baía de Maputo. MSc. Thesis, Universidade de Aveiro, Portugal, 134 pp.

- Canhanga, S. and Dias, JM. (2005). Tidal characteristics of Maputo Bay, Mozambique. *Journal of Marine Systems*, **58**, 83– 97.

- Chao, S.-Y. (1988). Wind-driven Motion of Estuarine Plumes. *Journal of Physical Oceanography*, **18**, 1144-1166.

- Climatemps (2013). *Climate of Maputo, Mozambique Average Weather*. http://www.maputo.climatemps.com/ consulted on 18th of December 2013.

- Cooper, A.J. and Pilkey, O.H. (2002). The Barrier Islands of Southern Mozambique. *Journal of Coastal Research*, **SI 36**, 164-172.

- Dale, A. W., Prego, R., Millward, G.E. and Gómez-Gesteira, M. (2004). Transient oceanic and tidal contributions to water exchange and flushing times in a coastal upwelling system in the NE Atlantic: the Pontevedra Ria, Galicia. *Marine Pollution Bulletin*, **49**, 235–248.

- De Boer, W. F. and Longamane, F A. (1996). The exploitation of inter-tidal food resources in Inhaca bay, *Mozambique. Biol. Conserv*., **78**, 295–303.

- De Boer, W.F., Rydberg, L. and Saide, V. (2000). Tides, tidal currents and their effects on intertidal ecosystems of the southern bay, Inhaca Island, Mozambique. *Hydrobiologia*, **428**, 187–196.

- Deltares (2011). Delft3D-Flow User Manual Version 3.15. Delft, The Netherlands, 627 pp.

- deCastro, M., Gómez-Gesteira, M., Prego, R, Taboada, J.J. and Montero, P. (2000). Wind and Tidal Influence on Water Circulation in a Galician Ria (NW Spain). *Estuarine, Coastal and Shelf Science* **51**, 161–176.

- deCastro, M., Gómez-Gesteira, M., Prego, R. and Neves, R. (2003). Wind influence on water exchange between the ria of Ferrol (NW Spain) and the shelf*. Estuarine, Coastal and Shelf Science*, **56**, 1055–1064.

- Dias, J.M. and Lopes, J.F. (2006). Implementation and assessment of hydrodynamic, salt and heat transport models: The case of Ria de Aveiro Lagoon (Portugal). *Environmental Modelling & Software*, **21**, 1–15.

- Dias, J.M., Sousa, M., Bertin, X., Fortunato, A. and Oliveira, A. (2009). Numerical modelling of the impact of the Ancão inlet relocation (Ria Formosa, Portugal*). Environmental Modelling & Software*, **24,** 711-725.

- Dyer, K.E. (1998*), Estuaries, A Physical Introduction, 2e*. John Wiley & Sons, 212 pp.

- Geyer, W.R. (1997). Influence of Wind on Dynamics and Flushing of Shallow Estuaries. *Estuarine, Coastal and Shelf Science*, **44**, 713–722.

- Gilcoto, M., Pardo, P. C., Álvarez-Salgado, X. A. and Pérez, F. F. (2007). Exchange fluxes between the Ría de Vigo and the shelf: A bidirectional flow forced by remote wind. *Journal of Geophysical Research*, **112**, C06001, doi: 10.1029/2005JC003140.

- Hoguane, A.M. (2007). Perfil Diagnóstico da Zona Costeira de Moçambique. Diagnosis of Mozambique Coastal Zone. *Revista de Gestão Costeira Integrada***, 7**(1), 69-82.

- Hoguane, A.M. (1994). *Tidal Currents and Oil Spill Dispersion in Maputo Bay*. 16 pp.

- Hoguane, A.M. and Dove, V.F. (2000). Condicções oceanográficas da Baía de Maputo. *Relatorio de estudos ambientais*. Instituto de Investigação Pesqueira, Maputo, Moçambique.

- Hoguane, A.M., Hill, A.E., Simpson, J.H. and Bowers, D.G. (1999). Diurnal and Tidal Variation of Temperature and Salinity in the Ponta Rasa Mangrove Swamp, Mozambique. *Estuarine, Coastal and Shelf Science*, **49**, 251-264.

- Kolmogorov, A.N. (1942). Equations of turbulent motion in incompressible fluid. *Izv. Akad. Nauk. SSR, Seria fizicheska Vi*, **1 2** (1-2): 56–58. English translation: 1968 Imperial College, Mech. Eng. Dept. Rept. ON/6.

- Lencart e Silva, J.D. (2007). Controls on Exchange in a Subtropical Tidal Embayment, Maputo Bay. Ph.D. dissertation, University of Wales, Bangor, 111pp.

- Lencart e Silva, J.D., Simpson, J.H., Hoguane, A.M. and Harcourt-Baldwin, J.-L. (2010). Buoyancy-stirring interactions in a subtropical embayment: a synthesis of measurements and model simulations in Maputo Bay, Mozambique. *African Journal of Marine Science,* **32**:1, 95-107

- Li, C. and O'Donnell, J. (1997). Tidally driven residual circulation in shallow estuaries with lateral depth variation. *Journal of Geophysical Research*, **102** (C13), 27915-27929.

- Li, M., Zhong, L. and Boicourt, W. C. (2005). Simulations of Chesapeake Bay estuary: Sensitivity to turbulence mixing parameterizations and comparison with observations. *Journal of Geophysical Research*, **110**, C12004.

- Linden, P.F. and Simpson, J.E. (1986). Gravity-driven flows in a turbulent fluid. *Journal of Fluid Mechanics*, **172**, 481-497.

- Linden, P.F. and Simpson, J.E. (1988). Modulated mixing and frontogenesis in shallow seas and estuaries. *Continental Shelf Research*, **8**(10), 1107-1127.

- Lutjeharms, J.R.E. and Jorge da Silva, A. (1988). The Delagoa Bight Eddy. *Deep-Sea Research*, **35**(4), 619-634.

- Milliman, J.D. and Meade, R.H. (1983). World-wide delivery of river sediment to the oceans. *Journal of Geology,* **91**, 1–21.

- Monsen, N.E., Cloern, J.E., Lucas, L.V. and Monismith, S.G. (2002). A Comment on the Use of Flushing Time, Residence Time and Age as Transport Time Scales. *Limnology and Oceanography*, **47**(5), 1545-1553.

- Monteiro, P.MS. and Marchand, M. (2009). Catchment2Coast: A Systems Approach to Coupled River-coastal Ecosystem Science and Management. *Deltares Select Series Volume 2*. IOS Press, 92 pp.

- Nunes, R.A. and Lennon, G.W. (1987). Episodic Stratification and Gravity Currents in a Marine Environment of Modulated Turbulence. *Journal of Geophysical Research*, **92,** C5, 5465-5480.

- Officer, C.B. (1976). Physical Oceanography of estuaries (and associated coastal waters). New York, Wiley, 480 pp.

- Pawlowicz, R., Beardsley, B. and Lentz, S. (2002). Classical tidal harmonic analysis including error estimates in MATLAB using T_TIDE. *Computers and Geosciences*, **28**, 929–937.

- Piedracoba, S., Álvarez-Salgado, X. A., Rosón, G. and Herrera, J.L (2005). Short-timescale thermohaline variability and residual circulation in the central segment of the coastal upwelling system of the Ría de Vigo (northwest Spain) during four contrasting periods. *Journal of Geophysical Research*, **110**, C03018, doi:10.1029/2004JC002556.

- Prandtl, L., (1945). Über ein neues Formelsystem für die ausgebildete Turbulenz. *Nachrichten von der Akademie der Wissenschaften in Göttingen*. Mathematisch-Physikalische Klasse, 6–19.

- Prego, R., Fraga, F. and Ríos, A. (1990). Water interchange between the Ría of Vigo and the coastal shelf. *Scientia Marina*, **54**(1), 95-100.
- Quartly, G.D. and Srokosz, M.A. (2004). Eddies in the Southern Mozambique Channel. *Deep Sea Research II*, **51**(1-3), 69-83, doi:10.1016/j.dsr2.2003.03.001.
- Ravikumar, S., Kathiresan, K., Thadedus Maria Ignatimmal, S., Babu Selvam, M. and Shanthy, S. (2004). Nitrogen-fixing azobacters from mangrove habitat and their utility as marine biofertilizers*. Journal of Experimental Marine Biology and Ecology*, **312**, 5-17.
- Ridderinkhof, H. and Zimmermann, J.T.F. (1992). Chaotic Stirring in a Tidal System. *Science* **258**(5085): 1107-1111.
- Sætre, R. and Jorge da Silva, A. (1982). Water masses and circulation of the Mozambican Channel*. Revista de Investigação Pesqueira*, **3**.
- Sete, C., Ruby, J. and Dove, V. (2002). Seasonal Variation of Tides, Currents, Salinity and Temperature along the Coast of Mozambique. Instituto de Investigação Pesqueira, Maputo, Moçambique, 72 pp.
- Simpson, J.H. (1997). Physical Processes in the ROFI regime*. Journal of Marine Systems*, **12**, 3-15
- Simpson, J.H. (1998). Tidal Processes in Shelf Seas (Chapter 5). *The Sea*, **10**. Brink. K.H. and Robinson, A.R. [eds.]. John Wiley and Sons Inc., 628 pp.
- Simpson, J.H. and Hunter, J.R. (1974). Fronts in the Irish Sea. *Nature*, **250**, 404-406.
- Simpson, J.H. and Sharples, J. (1991). Dynamically-active models in prediction of estuarine stratification. Dynamics and Exchange in Estuaries and Coastal Zones (ed D. Prandle), American Geophysical Union, Washington, D. C.. doi: 10.1029/CE040p0101
- Simpson, J.H., Allen, C.M. and Morris, N.C G. (1978). Fronts on Continental-Shelf. *Journal of Geophysical Research-Oceans and Atmospheres,* **83**(C9): 4607-4614.
- Simpson, J.H., Allen, C.M. and Morris, C.G. (1987). Fronts on the Continental Shelf. *Journal of Geophysical Research*, **83**(C9), 4607-4514.
- Simpson, J.H., Brown, J., Matthews, J. and Allen, G. (1988). Tidal Straining, Density Currents, and Stirring in the Control of Estuarine Stratification. Proceedings of the Estuarine Research Federation Conference, New Orleans, October 1987. To be published in Estuaries.
- Simpson, J.H., Brown, J., Matthews, J. and Allen, G. (1990). Tidal Straining, Density Currents, and Stirring in the Control of Estuarine Stratification. *Estuaries*, **13** (2), 125-132.

- Stow, A.C., Jolliff, J., McGillicuddy, D.J.Jr., Doney, S.C., Allen, J.I., Friedrichs, M.A.M., Rose, K.A. and Wallhead, P. (2007). Skill assessment for coupled biological/physical models of marine systems. *Journal of Marine Systems*, **76**, 4-15.

- Stow, A.C., Roessler, C., Borsuk, M.E., Bowen, J.D. and Reckhow, K.H. (2003). Comparison of Estuarine Water Quality Models for Total Maximum Daily Load Development in Neuse River Estuary. *Journal of Water Resources Planning and Management,* **129**(4), 307-314.

- Valle-Levinson, A., Miller, J.L. and Wheless, G.H. (1998). Enhanced stratification in the lower Chesapeake Bay following northeasterly winds. *Continental Shelf Research*, **18**, 1631-1647.

- Valle-Levinson, A., de Velasco, G.G., Trasviña, A., Souza, A.J., Durazo, R. and Mehta, A.J. (2009). Residual Exchange Flows in Subtropical Estuaries. *Estuaries and Coasts*, **32**, 54-67.

- Vas, Á., C. and v.d. Zaag, P. (2003). Sharing the Incomati Waters: Cooperation and Competition in the Balance. *Water Policy*, **5**(4), 349-368.

- Warner, J. C., Geyer, W. R., Lerczak, J. A., 2005. Numerical modelling of an estuary: a comprehensive skill assessment. *Journal of Geophysical Research*, **110**, C05001.

- Willmott, C.J. (1981). On the validation of models. *Physical Geography*, **2**, 184–194.

- Woods Hole Oceanographic Institute (1985). *CODE-2: Moored Array and Large-Scale Data Report*. CODE Technical Report No. 38, 73-107.

Appendix

Appendix A: Harmonic Analysis from Water Levels in Station Clube Naval

Constituent	Amplitude (m)		Phase Lag (°)		Differences Model-Observation	
Name	Observation	Model	Observation	Model	Ampl	Phase lag
MSF	0.019	0.008	266.609	181.417	-0.012	-85.192
Q_1	0.014	0.007	186.893	183.200	-0.007	-3.692
O_1	0.022	0.021	126.435	127.459	-0.001	1.024
K_1	0.056	0.041	189.745	179.058	-0.015	-10.687
MU_2	0.048	0.106	111.753	126.045	0.057	14.292
N_2	0.132	0.108	6.011	12.230	-0.024	6.219
M_2	0.897	0.879	271.386	270.470	-0.017	-0.916
S_2	0.495	0.479	172.918	177.603	-0.015	4.686
M_3	0.006	0.007	282.433	289.573	0.000	7.140
SK_3	0.008	0.002	8.634	243.851	-0.006	235.217
MN_4	0.002	0.003	135.287	225.060	0.001	89.773
M_4	0.008	0.020	94.005	119.460	0.011	25.455
MS_4	0.008	0.019	56.049	69.936	0.011	13.887
S_4	0.001	0.007	169.494	270.915	0.006	101.421
M_6	0.011	0.011	151.978	142.621	0.000	-9.357
$2MS_6$	0.018	0.019	41.646	35.559	0.001	-6.087
$2SM_6$	0.009	0.010	304.137	310.134	0.002	5.997
M_8	0.001	0.019	254.256	225.207	0.017	-29.049

Appendix B: Values of RMSE from Salinities over all Stations and all Surveys

Station	29. Jul 03	27. Sep 03	25-Oct 03	18. Nov 03	10-Dec 03	26. Jan 04	25. Feb 04	26-Mar 04	20. Apr 04	20-May 04	21. Jun 04
A1		0.144	0.195	1.354	2.049	1.344	0.935	2.770	2.977	3.714	5.046
A2	0.706	0.067	0.208	1.199	1.146	0.122	1.573	1.426	2.063	2.528	2.405
A3	1.234	0.241	0.484	0.752	0.817	0.182	2.669	0.458	1.643	1.442	2.318
A4	1.168	0.089	0.756	0.591	0.811	0.314	1.356	0.687	1.474	2.205	2.369
A5	0.926		0.688	0.590	0.859	0.370	0.971	0.577	1.651	1.639	
A6	0.340		0.612	0.634	0.660	0.300	0.121	0.665	1.862	1.502	1.868
A7	0.694		0.098	0.131	0.453	0.429	0.032	0.340	0.330	0.303	1.044
B1	1.396	0.375	0.168	0.227	0.835	0.162		1.475	3.496	2.002	1.652
B2	1.114	0.320	0.057	0.088	0.833	0.095		1.582	3.434	2.060	1.645
B4	1.010	0.077	0.319	0.687	0.861	0.171		0.991	1.873	2.626	3.538
B5	0.996	0.133	1.740	1.841	2.489	2.391		4.969	3.405	3.070	4.408
B6	0.797	0.118	2.085	1.812	2.466	2.200		3.990	3.969	3.458	
B7	1.324	0.037	1.647	1.880	3.367	3.637		4.435	3.581	3.064	4.912
CB1	0.110		0.022	0.248	0.308	0.812	0.301	0.239	0.615	0.640	0.486
CB2	0.119		0.032	0.059	0.919	0.715	0.325	0.430	0.909	0.121	0.192
CB3	0.111		0.017	0.141	4.337	0.465	0.633	1.009	0.268	0.138	0.077
CB4	0.142		0.147	0.083	0.278	0.033	1.296	0.055	2.496	1.497	0.436
CB5	0.541		0.019	0.132	0.567	1.253	0.214	2.135	1.702	2.204	1.903

Appendix C: Fit of the Regression Lines Used for Calculation of Flushing Times

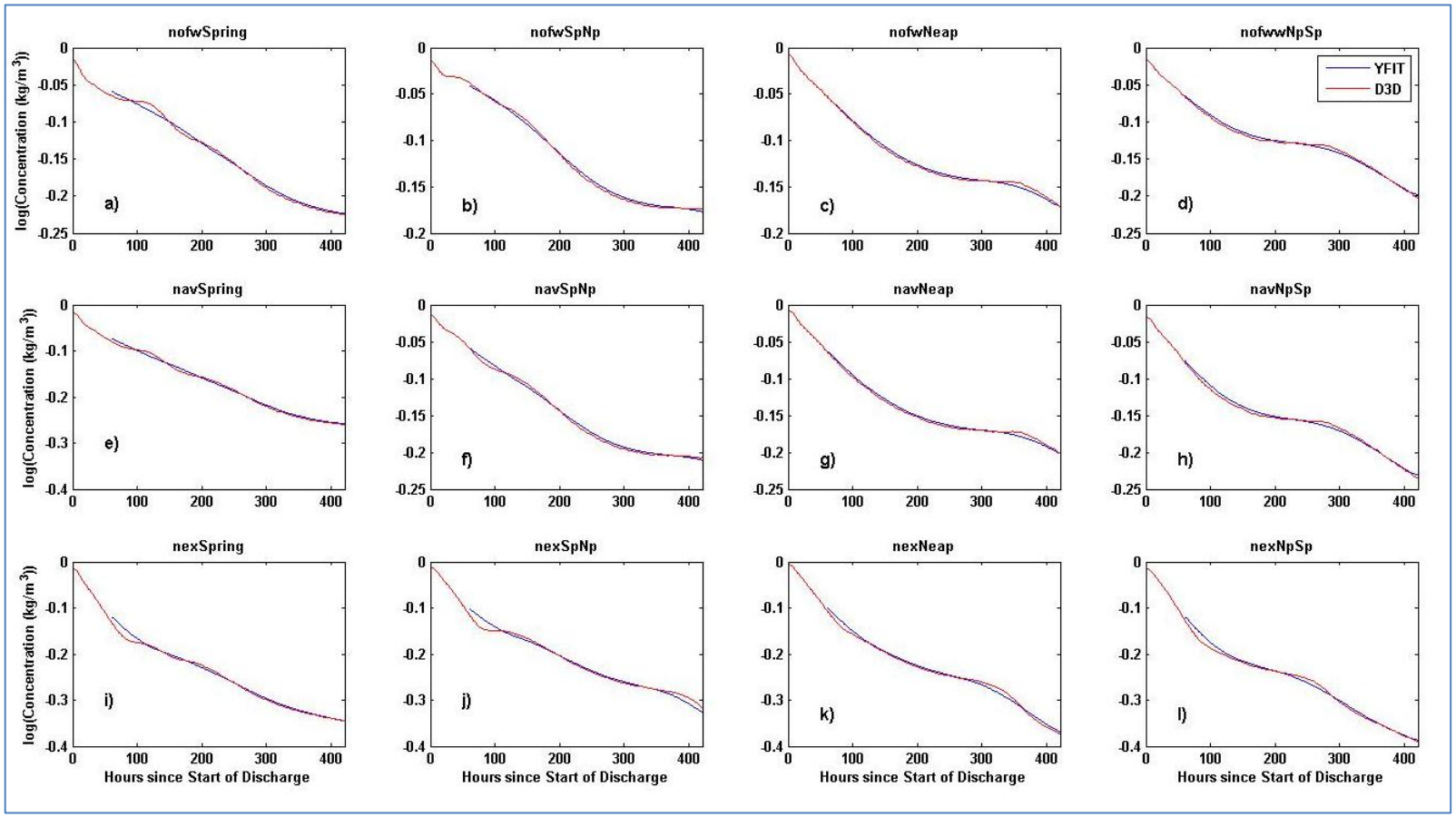

Fit of the regression model (blue line) to the logarithm of tracer concentration (red line) for various model runs: no discharge.: start at Spring tide (a), start between spring and neap tide (b), start at neap tide (c), start between spring and neap tide (d); average wet season discharge: start at Spring tide (e), start between spring and neap tide (f), start at neap tide (g), start between spring and neap tide (h); extreme discharge: start at Spring tide (i), start between spring and neap tide (j), start at neap tide (k), start between spring and neap tide (l).